

Aus dem Max-Planck Institut für Kolloid und Grenzflächenforschung

„Charakterisierung von Siliciumdioxid in Winterschachtelhalmen und dessen Umwandlung in biomorphe Keramiken“

Characterisation of Silica in *Equisetum hyemale* and its Transformation into Biomorphous Ceramics

Dissertation
zur Erlangung des akademischen Grades
„doctor rerum naturalium“
(Dr. rer. nat.)
in der Wissenschaftsdisziplin „Anorganische Chemie“

eingereicht an der
Mathematisch-Naturwissenschaftlichen Fakultät
der Universität Potsdam

von Lanny Sapei

Potsdam, im Oktober 2007

Elektronisch veröffentlicht auf dem
Publikationsserver der Universität Potsdam:
<http://opus.kobv.de/ubp/volltexte/2007/1588/>
[urn:nbn:de:kobv:517-opus-15883](http://nbn-resolving.org/urn:nbn:de:kobv:517-opus-15883)
[<http://nbn-resolving.org/urn:nbn:de:kobv:517-opus-15883>]

Since we are assured that the all-wise Creator has observed the most exact proportions of number, weight and measure in the make of all things, the most likely way therefore to get any insight into the nature of those parts of the Creation which come within our observation must in all reason be to number, weigh and measure.

Stephen Hales (1677-1761)

*To the memory of my beloved Mother
Soh Bie Lay (1943-2003)*

Abstract

Equisetum spp. (horsetail / “Schachtelhalm”) is the only surviving genus of the primitive Sphenopsids vascular plants which reached their zenith during the Carboniferous era. It is an herbaceous plant and is distinguished by jointed stems with fused whorl of nodal leaves. The plant has been used for scouring kitchen utensils and polishing wood during the past time due to its high silica encrustations in the epidermis. *Equisetum hyemale* (scouring rush) can accumulate silica up to 16% dry weight in its tissue, which makes this plant an interesting candidate as a renewable resource of silica for the synthesis of biomorphous ceramics. The thesis comprises a comprehensive experimental study of silica accumulations in *E.hyemale* using different characterisation techniques at all hierarchical levels. The obtained results shed light on the local distribution, chemical form, crystallinity, and nanostructure of biogenic silica in *E.hyemale* which were quite unclear until now. Furthermore, isolation of biogenic silica from *E.hyemale* to obtain high grade mesoporous silica with high purity is investigated. Finally, syntheses of silicon carbide (β -SiC) by a direct thermoconversion process of *E.hyemale* is attempted, which is a promising material for high performance ceramics.

It is found that silica is deposited continuously on the entire epidermal layer with the highest concentration on the knobs. The highest silicon content is at the knob tips ($\approx 33\%$), followed by epidermal flank ($\approx 17\%$), and inner lower knob ($\approx 6\%$), whereas there is almost no silicon found in the interior parts. Raman spectroscopy reveals the presence of at least two silica modifications in *E.hyemale*. The first type is pure hydrated amorphous silica restricted to the knob tips. The second type is accumulated on the entire continuous outer layer adjacent to the epidermis cell walls. It is lacking silanol groups and is intimately associated with polysaccharides (cellulose, hemicellulose, pectin) and inorganic compounds. Silica deposited in *E.hyemale* is found to be mostly amorphous with almost negligible amounts of crystalline silica in the form of α -quartz ($< 7\%$). The silica primary particles have a plate-like shape with a thickness of about 2 nm. Pure mesoporous amorphous silica with an open surface area up to 400 m²/g can be obtained from *E.hyemale* after leaching the plant with HCl to remove the inorganic impurities followed by a calcination treatment. The optimum calcination temperature appears to be around 500°C. Calcination of untreated *E.hyemale* causes a collapse of the biogenic silica structure which is mainly attributed to the detrimental action of alkali ions present in the native plant. Finally, pure β -SiC with a surface area of about 12 m²/g is obtained upon direct pyrolysis of HCl-treated *E.hyemale* samples in argon atmosphere. The original structure of native *E.hyemale* is substantially retained in the biomorphous β -SiC.

The results of this thesis lead to a better understanding of the silicification process and allow to draw conclusions about the role of silica in *E.hyemale*. In particular, a templating role of the plant biopolymers for the synthesis of the nanostructured silica within the plant body can be deduced. Moreover, the high grade ultrafine amorphous silica isolated from *E.hyemale* promises applications as adsorbent and catalyst support and as silica source for the fabrication of silica-based composites. The synthesis of biomorphous β -SiC from sustainable and low-cost *E.hyemale* is still in its initial stage. The present thesis demonstrates the principal possibility of carbothermal synthesis of SiC from *E.hyemale* with the prospect of potential applications, for instance as refractory materials, catalyst supports, or high performance advanced ceramics.

Zusammenfassung

Equisetum spp. (Schachtelhalm) ist die einzige überlebende Gattung der Schachtelhalmgewächse, die ihren Zenit während der Karbon Ära erreichten. Der Schachtelhalm ist eine krautartige Pflanze und wird durch verbundene Stämme mit fixiertem Wirtel der Knotenblätter unterschieden. Aufgrund seiner hohen Siliciumdioxid Bedeckung in der Epidermis sind Winterschachtelhalmen lange Zeit zur Reinigung von Küchegeräten und zum Polieren von Holz verwendet worden. Der Winterschachtelhalm (auch Scheuerkraut genannt) kann Siliciumdioxid bis zu 16% Trockengewicht in seinem Gewebe ansammeln. Dies macht aus dieser Pflanze einen interessanten Kandidaten als erneubare Ressource von Siliciumdioxid für die Synthese von biomorphen Keramiken. Die vorliegende Doktorarbeit beinhaltet eine ausführliche experimentelle Studie der Siliciumdioxidansammlungen in Winterschachtelhalmen mittels unterschiedlicher Charakterisierungstechniken auf allen hierarchischen Ebenen. Die Ergebnisse der Arbeit werfen neues Licht auf die lokale Verteilung, die chemischen Form, die Kristallinität und die Nanostruktur des biogenen Siliciumdioxids, die bisher ziemlich unklar waren. Außerdem werden Möglichkeiten zur Isolierung des biogenen Siliciumdioxids aus Winterschachtelhalmen untersucht, um hochgradig reines Siliciumdioxid zu erhalten. Auch wird die direkte carbothermale Synthese von Siliciumkarbid (β -SiC) aus Schachtelhalmen untersucht, mit dem Ziel einer kostengünstigen Herstellung von Hochleistungskeramiken aus nachwachsenden Rohstoffen

Es wird gezeigt, dass das Siliciumdioxid in einer kontinuierlichen Schicht in der Epidermis vorliegt, mit der höchsten Siliciumkonzentration in den auffälligen knopfartigen Ausbuchtungen. Den höchsten Siliciumgehalt zeigen die Knospitzen ($\approx 33\%$), gefolgt von der epidermalen Flanke ($\approx 17\%$) und inneren unteren Teile der Knöpfe ($\approx 6\%$), während es in den inneren Teilen der Pflanze praktisch kein Silicium gibt. Ramanspektroskopie beweist eindeutig, dass mindestens zwei Siliciumdioxid Modifikationen vorhanden sind. Der erste Typ ist reines hydratisiertes amorphes Siliciumdioxid, das auf den Bereich der Knospitzen beschränkt ist. Der zweite Typ wird in der gesamten kontinuierlichen äußeren Schicht angesammelt, weist keine Ramanbanden von Silanolgruppen auf, und ist örtlich eng verknüpft mit Banden von Polysacchariden (Zellulose, Hemizellulose, Pektin) sowie anorganischen Verbindungen. Der Großteil des Siliciumdioxids in Winterschachtelhalmen ist amorph mit unwesentlichen Mengen an kristallinem α -Quarz ($< 7\%$). Die primären Siliciumdioxidpartikel haben eine plattenähnliche Form mit einer Dicke von ungefähr 2 nm. Hochreines mesoporöses amorphes Siliciumdioxid mit offener Porosität und innerer Oberfläche bis zu $400 \text{ m}^2/\text{g}$ kann aus Winterschachtelhalmen isoliert werden. Dies wird erreicht indem man die Pflanze mit Salzsäure behandelt um die anorganischen Verunreinigungen zu entfernen, gefolgt von einer Kalzinierung, wobei die optimale Temperatur bei etwa 500°C liegt. Im Gegensatz zu den chemisch vorbehandelten Schachtelhalmen, verursacht die Kalzinierung von unbehandelten Winterschachtelhalmen einen Kollaps der biogenen Siliciumdioxidstruktur, und es werden nur sehr kleine innere Oberflächen erzielt. Dies wird hauptsächlich dem Einfluss der Alkaliionen zugeschrieben die in der unbehandelten Pflanze vorhanden sind. Es wird schließlich gezeigt, dass durch direkte Pyrolyse der HCl-behandelten Winterschachtelhalme in Argonatmosphäre reines β -SiC mit einer Oberfläche von

ungefähr 12 m²/g erzeugt werden kann. Die ursprüngliche Struktur von natürlichen Winterschachtelhalmen bleibt dabei im Wesentlichen im biomorphen β -SiC erhalten.

Die Ergebnisse dieser Arbeit führen zu einem besseren Verständnis des Silicifizierungsprozesses und erlauben es auch, Aussagen über die mögliche Rolle von Siliciumdioxid in *E.hyemale* zu treffen. Insbesondere kann den Pflanzenpolymeren die Rolle eines Templates bei der Synthese des biogenen Siliciumdioxids im Pflanzengewebe zugeschrieben werden. Das aus den Pflanzen isolierte ultrafeine amorphe Siliciumdioxid mit hoher Reinheit verspricht potentielle Anwendungen, z.B. als Adsorbent oder Katalysatorsupport, und auch als Füllmaterial für die Herstellung von Kompositmaterialien. Die Synthese von biomorphem β -SiC aus erneubaren und preiswerten Winterschachtelhalmen steht zwar erst am Anfang, jedoch konnte die vorliegende Arbeit die prinzipielle Machbarkeit aufzeigen. Dieses Material scheint sehr vielversprechend für eine Reihe technischer Anwendung, zum Beispiel als Refraktärmaterial, Katalysatorsupport oder neuartige Hochleistungskeramik.

Contents

Abstract	i
1. Introduction	1
1.1. <i>Equisetum hyemale</i>	2
1.1.1 Biological background	2
1.1.2 Silica in <i>Equisetum hyemale</i>	4
1.2. Silicon-based biomorphous ceramics	5
1.2.1 Silica and its polymorphs	5
1.2.2 Biogenic silica	6
1.2.3 Silicon carbide	8
1.3. Objective and scope of works	12
1.4. Outline of the thesis	13
2. Silica in <i>Equisetum hyemale</i>	14
2.1. Study of silica accumulation in <i>E.hyemale</i> during the growth period	14
2.2. Microscopic investigations of silica in <i>E.hyemale</i>	22
2.3. Molecular investigations of silica in <i>E.hyemale</i>	24
2.3.1 Confocal Raman Microscopy	25
2.3.2 FTIR	28
2.4. Crystallinity and nanostructural study of silica in <i>E.hyemale</i>	31
2.5. H ₂ O ₂ -treated <i>E.hyemale</i>	36
2.6. Discussion	42
2.7. Summary	46
3. Isolation of Silica from <i>Equisetum hyemale</i>	48
3.1. Native and HCl-treated <i>E.hyemale</i>	49
3.2. Ash and biogenic silica from <i>E.hyemale</i>	53
3.3. Discussion	62
3.4. Summary	66

4. Silicon Carbide (β -SiC) from <i>Equisetum hyemale</i>	67
4.1. Microtomography	69
4.2. SEM/ EDX analysis	70
4.3. Powder Diffraction/ WAXS	72
4.4. SAXS	75
4.5. Nitrogen sorption	76
4.6. Discussion	78
4.7. Summary	79
5. Conclusions and Outlook	80
5.1. Conclusions	80
5.2. Outlook	83
Appendix A. Characterisation Methods	vi
Appendix B. Experimental Details	xl
Appendix C. SAXS/WAXS Data Evaluation	lii
References	lix
Acknowledgements	lxix
<i>Curriculum vitae</i>	lxxi

Chapter 1

INTRODUCTION

Silicon is of special interest in the series of chemical elements. It is the most abundant element next to oxygen in the form of silicates in building up the earth's crust. These silicates are not only of geochemical significance as structural components of the earth but also are of outstanding practical and cultural value in the form of man-made synthetic materials, for instance bricks, earthenware, glass, enamel, white ware, porcelain and cement ¹. The history of man's use of natural "stones", such as flint, the most important material for making man's first implements, which were mined more than 5000 years ago and the history of quartz and of semi-precious stones ("Halbedelsteine") which were used as ornaments even in the earliest times, is of cultural and archeological significance ¹.

Silica (SiO₂) belongs to silicate compounds and is one of the most common materials in nature. It is the main constituent of more than 95% of all the earth's rocks ². Most glasses in our everyday surroundings are made of mainly silica, combined with a variety of other substances. In technology, SiO₂ is present in most devices containing metal-oxide-semiconductor transistors. For these and other reasons SiO₂ has been studied quite extensively over the years and has always been a focus of attention, from both the theoretical and practical viewpoints ^{2,3}.

Biom mineralisation is related to the accumulation of minerals in living organisms, mainly to strengthen or stiffen the organic tissues. Important examples include calcium carbonates in invertebrates such as mollusk shells ⁴ and calcium phosphates in vertebrates, e.g. bone ⁵. Among the biominerals, silica (SiO₂) represents the second most abundant biogenic mineral after carbonate ⁶ and it is mostly deposited in living organisms in the form of amorphous silica similar to opal or silica gel ⁷⁻¹⁰. It is often referred to as biogenic silica ^{7,10} and is ubiquitous in lower organisms, such as diatoms, sponges, and radiolarian ^{7, 11, 12} which extract silica from the water to build up their exoskeleton. Among the higher plants, grasses (*Poaceae/ Gramineae*), for instance rice, bamboo, wheat, barley, sorghum, rye, oat, and in particular *Equisetum* (horsetail/

“Schachtelhalm”) are ranked among Si accumulators that implement high amounts of silica mainly in their aerial tissues⁸.

1.1 *Equisetum hyemale*

1.1.1 Biological background

Horsetail (*Equisetum spp.*) is ranked amongst the most ancient of living vascular plants¹³. *Equisetum* has occurred in rocks of upper Devonian and Lower Carboniferous age¹⁴. They delineate the class Sphenopsida and are the only extant member of this class¹⁵. Horsetail is an herbaceous perennial plant without secondary tissues that is found in or near watery areas such as marshes, streams, or rivers and particularly grows in temperate northern hemisphere areas of Asia, Europe, North America, and North Africa. It is distinguished by jointed stems with fused whorl of nodal leaves. They have also a peculiar ability to deposit silica in their epidermis. Thus they were used in Europe for scouring metal and polishing wood during the past time ("scouring rush" is a common name for *Equisetum*, especially *Equisetum hyemale* having rough-ridged siliceous stems).



Figure. 1.1 *Equisetum hyemale*, “Winterschachtelhalm”

The *Equisetum* genus is commonly divided into two groups and 15 species^{16, 17}, namely subgenus *Equisetum* and *Hippochaete*. The first has stomata flush with the epidermis and stems branched (e.g. *E.arvense*), whereas the latter has stomata sunken below the surface of the epidermis and stems generally unbranched (e.g. *E.hyemale*). *E.hyemale* (scouring rush) is a perennial and evergreen plant and can persist over two winters¹⁶. *E.hyemale* has an unbranched, chlorophyllous and upright stem (Fig. 1.1) and its anatomy can be seen in Fig. 1.2. The stems have a corrugated structure with distinctive ridges and grooves. The ridges are occupied by two parallel rows of silica tubercles or knobs which contribute to the stem roughness. On the each flank of the grooves a single line of stomata is arranged. The stomatal apparatus of the *Equisetum* consists of a pair of guard cells internal to a pair of subsidiary cells. The epidermis is quite thick since it is encrusted by silica and cuticularised. The tissue underlying the epidermis is called schlerenchyma/ hypodermal sterome, but sometimes called collenchyma since these cells were unligified and had relatively large pits and stored starch (implying that they are living)¹⁶. They function as supporting tissues due to their thick cell walls. *E.hyemale* is very porous and light materials, marked by big hollow pith in the middle and several canals (vallecular canals, carinal canals) and cavities.

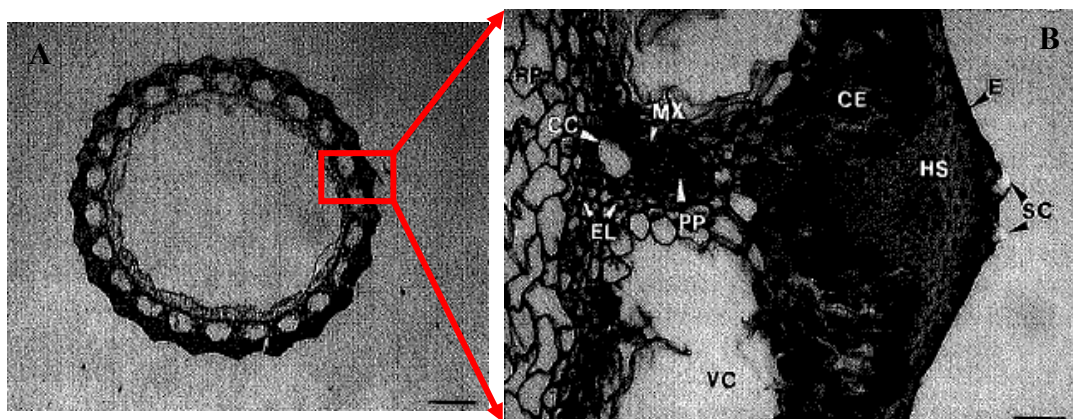


Figure. 1.2 Anatomy of *Equisetum hyemale*. (A) Cross section (70 μm thickness). The scale bar equals 1 mm. (B) Detail of the same cross section. The scale bar equals 0.1 mm. HS: hypodermal sterome; E: epidermis; SC: silica in the knobs; CE: chlorenchyma; VC: vallecular canals; MX: lignified metaxylem tracheids; PP: primary phloem; CC: carinal canals; RP: parenchymateous pith; EL: endodermis layer. Figures are taken from Speck *et al.*¹⁸.

1.1.2 Silica in *Equisetum hyemale*

Silica concentrations can reach up to 25% dry weight in *Equisetum*¹⁹ by absorbing the silicic acid from the soil⁹ and transport it to its tissue. Silica deposition in plants can take place in cell wall, cell lumen and in extracellular sites¹⁰. Discrete plant silica bodies (“phytolith”) with various shapes and morphologies depending on plant species are mainly deposited in cell lumen or cell wall and are of archeological interest to identify the vegetation patterns during the past periods^{8, 20, 21}. Even though the amount of silica in many plants can exceed that of other macrominerals such as calcium, magnesium and phosphorus, it is usually not considered to be essential because most plants can grow in nutrient solutions lacking of silicon in their formulations⁹. In the case of horsetail however, silica seems to be crucial for a normal plant growth^{22, 23}. Several functional properties have been attributed to the silica in horsetail such as²³: (i) reduction of the transpiration rate which influences its evergreen characteristic; (ii) reflection of excessive light together with cuticle; (iii) acting as a protector against predators; (iv) yielding a viable spore for reproduction. A mechanical role of silica in strengthening and stiffening the tissue has also often been claimed^{8, 24, 25, 26}. In spite of the general agreement of an important functional role of silica as essential element in the *Equisetum* family, there have been only limited experimental studies on the structure, local concentration and distribution of silica in these plants. Investigations were typically performed using scanning electron microscopy (SEM) in combination with EDX elemental analysis^{24, 27}, and in some cases they were also complemented by transmission electron microscopy (TEM)^{25, 26} and SAXS²⁶. However, the conclusions drawn in these papers do not yet provide a satisfactory and conclusive picture about the role of silica in *Equisetum*, thus a comprehensive structural and analytical investigation on silica accumulations in *E.hyemale* at all hierarchical levels is essentially necessary.

1.2 Silicon-based biomorphous ceramics

1.2.1 Silica and its polymorphs

Silicon is the second most abundant element after oxygen which makes up 25.7% of the earth's crust²⁸. It is not found free in the nature, but occurs chiefly as the oxide and as silicates. *Sand, quartz, rock crystal, amethyst, agate, flint, jasper, and opal* are some of the forms in which the oxide appears, whereas *granite, hornblende, asbestos, feldspar, clay, and mica* are a few examples of the numerous silicate minerals²⁸.

Silicon dioxide is the only compound of Si-O system that is thermodynamically stable over a wide range of temperatures and pressures³. SiO₂, whose common name is silica, exists in many allotropic forms. Most of them are found in nature in abundant quantities, but some have been made only under laboratory conditions. The best known are quartz, cristobalite, tridymite, and amorphous vitreous silica. The three crystalline forms at atmospheric pressures (quartz, cristobalite, and tridymite) have all high and low temperature forms. Additionally to the reconstructive transformation between the 3 polymorphs they all undergo displacive transformations between these low and high temperature forms on heating and cooling (see Fig. 1.3). The polymorphic transformations of silica play an important role in ceramic technology owing to the use of different crystalline forms (modifications) of silica (in particular, quartz) as the initial component for producing numerous silicate materials.

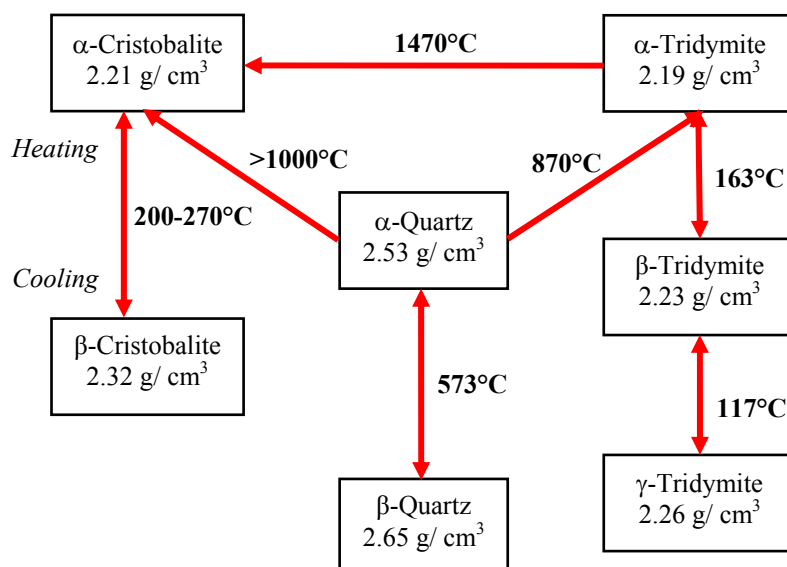
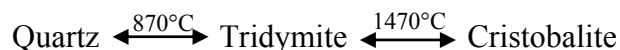


Figure. 1.3 Phase transformation of silica polymorphs at atmospheric pressure²⁹.

The stability relation for quartz, tridymite, and cristobalite proposed by Fenner³⁰



was further corrected by Stevens *et al.*³¹ who stated that tridymite is not a stable phase in the pure silica system. Cristobalite can be produced from pure quartz by heating, whereas it is not possible to produce tridymite in this fashion since a flux or mineralizer is required and even in this case cristobalite is produced before any tridymite is observed. Amorphous silica, which is predominantly found in biological systems can be also directly converted into α -cristobalite in the temperature range between 1200-1400°C³².

1.2.2 Biogenic silica

At present, sol-gel processing or vapour-phase reaction using silicon alkoxides such TEOS (tetraethyl orthosilicate) / TMOS (tetramethyl orthosilicate) as precursors³³⁻³⁶ are commonly used to produce ultra-fine silica powders. Nanometer-sized silica particles obtained from burning of SiCl₄ in an oxygen-hydrogen flame is also reported³⁷. These processes produce ultra-fine silica with high purity but their preparation including the initial precursors are very expensive, thus limiting their wide applications. As an alternative to prepare high purity silica based on high volume and low cost, silica rich plant materials are certainly of interest. Silica in plants is found to be mostly amorphous and is typically of nanometer size^{10, 26, 38}. Thus it can be considered as cheap, highly reactive silicon source for the production of various silicon-based materials with novel properties which may be of technical and industrial importance. Amorphous silica has been used extensively for a wide range of commercial applications as catalyst supports, as separation media, as filler in polymer and in biomedical applications⁷. Biogenic silica can be expected to possess reactivity similar to the numerous ionic, non-ionic, and covalent interactions that are known to be present in commercial silica⁷. Biogenic amorphous silica from diatom, diatomaceous earth which is also known as “kieselguhr” has been widely used commercially mainly as filter aid with “CELITE” as the trade name³⁹ or filter⁴⁰ besides also being used as adsorbent⁴¹ and insecticides⁴². Among higher plants, numerous attempts of silica isolation from rice husks containing of about 20% silica^{38, 43} to obtain either rice husk ash (RHA) or

biogenic silica after thermal/chemical treatments have been investigated^{38, 43-51}. Several applications of rice husk derived silica as fillers in rubbers and plastics or in cement production has been reported⁵². Further utilisation of silica in rice husks by different transformation processes into many silicon-based materials, for e.g. silicon⁵³, silicon carbide⁵⁴⁻⁶³, silicon nitride⁶³⁻⁶⁵ and zeolite⁶⁶ have also been intensively investigated. However, unlike rice husks, there are practically no investigations considering *Equisetum* as a potential resource for biogenic silica. There are only very few studies reporting some attempts to use *Equisetum* as precursors for β -SiC synthesis by a direct thermoconversion process⁶⁷⁻⁶⁸. There are also some recent attempts to use *Equisetum* as a biological template for the synthesis of zeolite with hierarchical pores by biomineral-silica-induced mechanism⁶⁹⁻⁷⁰.

Biogenic silica is always present in association with organic tissue, such as polysaccharides or proteins⁷¹⁻⁷². Therefore, an appropriate strategy to isolate silica from plant materials with desired properties (for instance large surface area and high porosity) has to be seriously considered. It has been shown that amorphous mesoporous silica with very high surface area can be obtained from rice husks, if they are subjected to an acidic treatment with hydrochloric acid prior to calcinations⁴⁷⁻⁴⁸. The low surface area of silica obtained from untreated rice husks is mainly due to the strong interaction of silica with potassium^{47, 73} leading to the surface melting of silica⁷³. The alkali-silica fusion causes coarsening of particles^{38, 50}. Moreover, Real *et al.*⁷⁴ provided some evidence from XAFS measurement that potassium oxide leads to the disruption of SiO₄ network and the formation of chain like structure of non-bridging oxygen atoms. Additionally, potassium and sodium also accelerates the crystallisation of amorphous silica into cristobalite^{73, 75}, which is not desirable since it is less reactive than amorphous silica. Metallic ingredients have a substantial effect on the quality of silica⁵¹. Thus, removal of alkaline elements by acid treatment before the calcination is a necessary step in the production of biogenic silica with high surface area and high purity indicated by the completely white ash colour⁴⁶. Acidic treatment of rice husks using HCl is proved to be more superior compared to other inorganic acids (HNO₃, H₂SO₄, H₃PO₄), organic acids (acetic acid, oxalic acid, citric acid), or bases (NaOH, NH₄OH) since it is very effective at substantially removing the metallic ingredients^{45, 46, 50, 59}. The silica obtained after the subsequent calcinations is of high purity of at least

99%^{43, 45}. Furthermore, HCl treatment does not affect the amorphousness of the biogenic silica in rice husks⁴⁶. Moreover, thermal treatment for the organics removal should be carried out at a low combustion temperature and a prolonged heating for a complete combustion of rice husk to white ash since the burning of fixed carbon in the rice husk takes place at a slow rate at low temperature⁴⁶. A combustion temperature of 500°C and above is required to produce white ash within a reasonable time⁴⁶. Pure form of silica with minimum impurities and amorphous nature is essential for the preparation of advance inorganic materials, for instance silicon carbide.

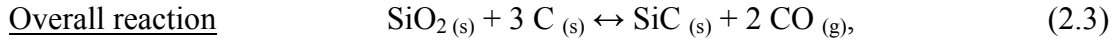
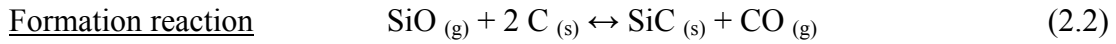
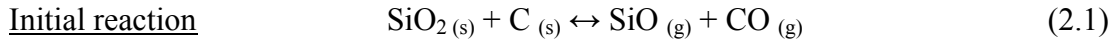
1.2.3 Silicon carbide

Silicon carbide is a non-oxide ceramic material, in contrast to silicon dioxide. Silicon carbide is extremely hard, resistant to both thermal shock and high temperatures, quite inert chemically under many circumstances. It has a low density and a high thermal conductivity, and its mechanical properties are unusual for a non-metallic solid⁷⁶. Thus the range of applications extends from metallurgical and chemical uses through abrasive and abrasion-resistant forms to refractory and mechanical engineering materials to protective coatings and application in nuclear technology to electrical and electronic equipment⁷⁶. SiC consists of several modifications, namely:

1. β -SiC (low temperature modification), which has a cubic structure and one polytype.
2. α -SiC (high temperature modification), which has a hexagonal or rhombohedral structure and about 250 polytypes.

Formation of SiC is possible starting already at 600°C (Fig. 1.4) where β -SiC is formed below 2000°C. Above this temperature, a phase transformation into α -SiC occurs⁷⁷.

SiC is hardly found in the nature. It can be found only in some volcano ash and meteorit both in α - and β -modification. SiC was produced by a technical process called “ACHESON process” in 1891 by E.G. Acheson and the product is mainly α -SiC with rough grains⁷⁷. This process is still applied up to now with some improved modifications. High energy (10 kWh/kg) and high quality of raw materials (quartz and coke) are required. The mechanisms of SiC formation are described by the carbothermal reduction of silica via a gas-solid reaction with SiO gas as an intermediate product as follows⁷⁷:



$$\Delta H_R = +618.5 \text{ kJ/mol}$$

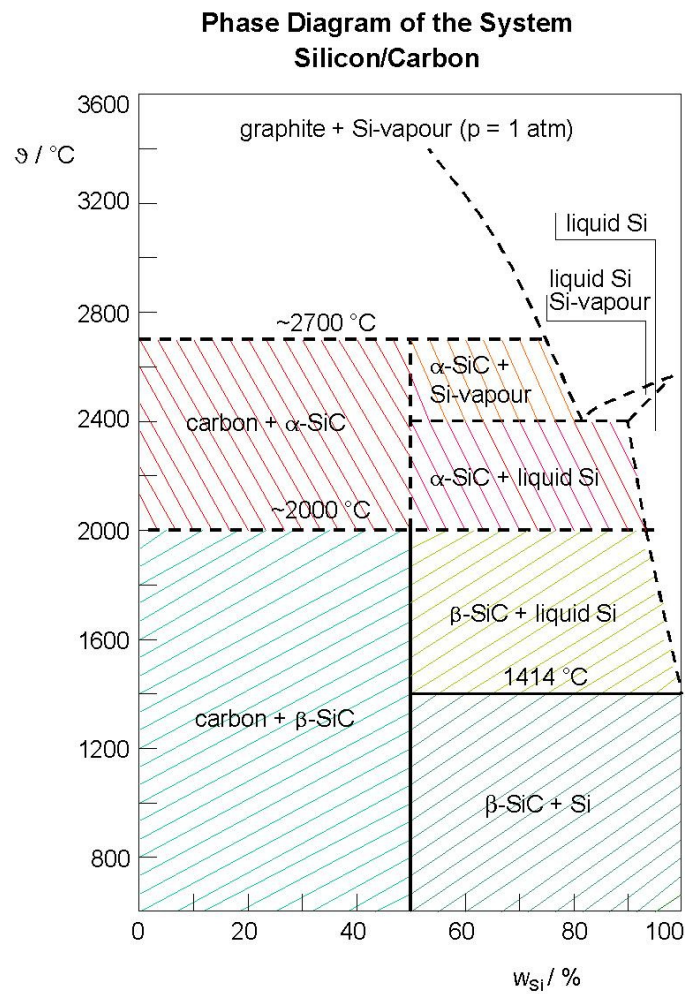
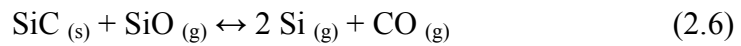
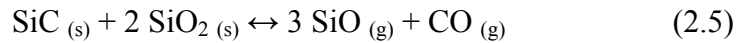
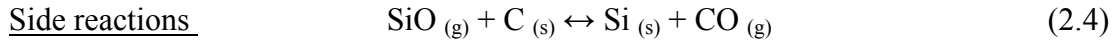


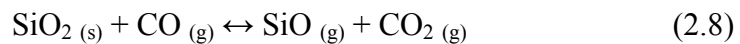
Figure 1.4 Phase diagram of silicon-carbon system ⁷⁷.

In principle, silicon carbide powders can be produced in 4 different ways: (i) chemical vapour deposition (CVD) of silane compounds ⁷⁸, (ii) sol-gel processing of silicon alkoxides ⁷⁹, (iii) direct carbonisation of Si metals ^{80, 81}, (iv) carbothermal reduction of silica ^{59-61, 77}. In terms of economy and efficiency, the carbothermal reduction is the best choice, even though the purity of SiC powders is not as high as those produced by other methods. It involves inexpensive silicon dioxide and carbon (or carbon precursors) as the starting materials ⁸². The industrial manufacture of SiC is widely performed by the Acheson process, which includes a carbothermal reduction of sand by petrol coke at high temperature ranging from 2000-2500°C ⁸³. However, the produced SiC still posses sharp grains after the final grinding process and a mixture of different SiC polytypes ⁶⁷. Besides that, high energy and high quality of raw materials (quartz and coke) are also required ⁷⁷.

There has been an increasing interest to produce artificial microstructures that resemble that of natural materials because biological structures exhibit excellent strength, high stiffness and elasticity at low density, as well as high damage tolerance, integrated into these structures through the evolutionary process ⁸⁰. Natural materials such as wood, jute, diatom, etc. are widely used as bio-templates to produce biomorphous ceramics, for e.g. SiC/C and TiC/C with the cellular structures and the final materials exhibit good performance in electric conduction, thermal conduction, friction, adsorption properties, and mechanical properties ⁸⁴⁻⁸⁶. Biomorphous SiC has been a matter of interest in recent years since it offers several advantages over conventional SiC materials such as less energy consumption and retention of microstructures of the biological precursors favouring of high specific strength and excellent high temperature stability ^{84, 87-89}. The general approach of the biomorphous SiC production from wood consists of a rapid and controlled mineralisation of the wood, with two steps: first the wood is carbonised, and second it undergoes a gas phase infiltration of silicon or a reactive infiltration of molten silicon to produce a SiC material that keeps the wood microstructures ^{84, 86, 87, 90}. This low density cellular biomorphous SiC has potential applications as high-temperature filters and as catalyst carriers ⁹¹.

There have been already numerous investigations on the transformation of silica-rich and renewable plant materials, such rice husks into SiC ⁵⁴⁻⁶³ and very few studies

on SiC synthesis using *Equisetum* as precursors^{67, 68}. SiC from rice husk was reported for the first time by Lee and Cutler⁵⁴ and has been intensively investigated until now. Rice husk which contains 15-20% silica and cellulosic materials as the carbon source can be converted into β -SiC with very fine grain size (0.1 μm) by heat treatment between 1290-1600°C using Fe as a catalyst⁷⁷. There are four competitive processes supposed to take place during the carbothermal reaction of silica from rice husk, i.e.: crystallisation of amorphous silica to cristobalite, partial graphitisation of amorphous carbon, formation of SiC polycrystals, and formation of SiC whiskers^{55, 92}. The crystallisation of both silica and carbon are barriers to the SiC formation since they are less reactive than their amorphous forms. The formation of SiC is via carbothermal reduction of silica according to the reaction 2.1 - 2.3. However, the formation of silicon would require a large excess of SiO compared to CO which is not fulfilled in the case of carbothermal reaction of silica from plant materials⁹³. Thus, side reactions considered to be likely to occur are⁵⁶:



Production of SiC from silica-rich plant materials is the most effective way from the economic and environmental point of view. It is due to the abundance of low cost and high volume raw materials which already consist of the main components for SiC synthesis, namely silica and carbon, thus addition of starting materials is not needed. Moreover, it is known that carbon and silica in plants are closely associated^{63, 71, 72}, therefore mixing process can be eliminated and they can readily contact during the pyrolysis. The presence of excess carbon is also beneficial in increasing the rate of reaction⁵⁹. Plant silica is highly reactive due to its amorphous character⁷ allowing the reaction to occur at low temperatures, i.e. within the range of 1200-1500°C⁶¹, which is far below those used for the reaction between crystalline silica and graphite^{55, 59}, thus energy consumption can be reduced. At low temperature, agglomeration and bonding of particles are hindered⁶¹, thus SiC particles in nanometer scale which is in fact depending on the size of nanosized silica and carbon^{55, 82} could be obtained. Monotype SiC (for instance β -SiC) could be obtained when the pyrolysis is carried out at temperature below 2000°C⁷⁷. Finally, the SiC particles would substantially retain hierarchical structure inherited from the original plant material, thus it may exhibit

novel properties, such as better thermal and mechanical properties. However, acid leaching of raw plant materials for the inorganic impurities (mainly K and Ca) removal is essentially necessary prior to heat treatment for getting pure SiC with high yield due to the reduced the crystallisation of silica and carbon^{51, 58}. Several applications of biomorphous SiC derived from rice husks as filler in composites, semiconductor, abrasive materials have been reported⁵².

1.3 Objective and scope of works

There are three main objectives of the work reported in this thesis:

- Detailed investigation of silica in the native plant *E.hyemale*.
- Isolation of biogenic silica from *E.hyemale* by chemical and thermal treatments and its nanostructural characterisation.
- Synthesis of biomorphous β -SiC from *E.hyemale*.

The main focus within this thesis is to get an overall picture of silica characteristics accumulated in *E.hyemale*. Therefore, the work is divided into several different tasks covering the characterisations of silica at all levels of hierarchy:

- Bulk analysis of *E.hyemale* shoots by means of chemical analysis to determine the accumulation patterns of silica during the growing time as well as determination of macroscopic silica distribution within mature *E.hyemale* stems.
- An investigation of local silica distribution in *E.hyemale* internodes. For this purpose, microtomography, SEM/EDX mapping of Si, semi quantitative analysis using SEM/EDX, SEM/BSE, and Raman microscopy are employed.
- Raman microscopy and FTIR are used to study the silica form present in *E.hyemale* tissues.
- Crystallinity of silica in *E.hyemale* is studied by X-ray diffraction (XRD/WAXS), whereas for its nanostructure investigations, Small-angle X-ray Scattering (SAXS) and nitrogen sorption are applied.

The other two objectives are based on the results from the first objective which determines the selection of chemical and thermal processes for the plant silica isolation as well as synthesis of β -SiC. SAXS/WAXS and nitrogen sorption techniques are mainly used for the characterisation of both silica and β -SiC derived from *E.hyemale*.

1.4 Outline of the thesis

This thesis consists of an introductory chapter, the description of the main research results in the following three chapters, a conclusion and appendices. The introduction in chapter 1 is intended to give a short background on the origin and anatomy of *Equisetum hyemale* including a short literature overview of silica in higher plants, followed by a general state of the art description of silicon based ceramics from biological precursors. In Chapter 2, a comprehensive structural and analytical study of silica accumulated in *E.hyemale* is presented. Chapter 3 deals with the isolation of silica from *E.hyemale* using chemical and thermal treatments and its nanostructural characterisation. Chapter 4 reports several attempts to convert silica from *E.hyemale* into SiC upon pyrolysis at high temperature. Chapter 5 finally draws general conclusions and provides an outlook for further research. The theoretical background about the different characterisation methods used in this work is described in Appendix A. Appendix B contains details of sample preparations and a description of the scientific instruments employed during the measurements. SAXS/WAXS data treatment and evaluation is finally described in Appendix C.

Chapter 2

Silica in *Equisetum hyemale*

2.1. Study of silica accumulation in *E.hyemale* during the growth period

The average silica content of dry shoots at different harvesting time within the growth period from the beginning of June until November 2005 were determined as depicted in Fig. 2.1. New shoots commenced out from the soil at the beginning of spring time, i.e. at the end of April and then started to grow at the beginning of May and continued until July. In August, the shoots appeared to reach their maturity already, marked by their maximum lengths (about 75 cm, based on visual observation). Hauke¹⁶ stated that the cones of *E.hyemale* are mature by end of July and shed spores through August and September or the cones are over wintering, releasing the spores in April and May. During winter period, the growth is ceased due to the quiescent phase and *E.hyemale* shoots continue growing in the next spring time.

The silica accumulation increased from around 6% to about 14% as the shoots were getting older (Fig. 2.1 (A)). This seems not to be accompanied by a biomass increase, since carbon content appeared to be relatively constant at about 37% during the growth period (Fig. 2.1 (B)).

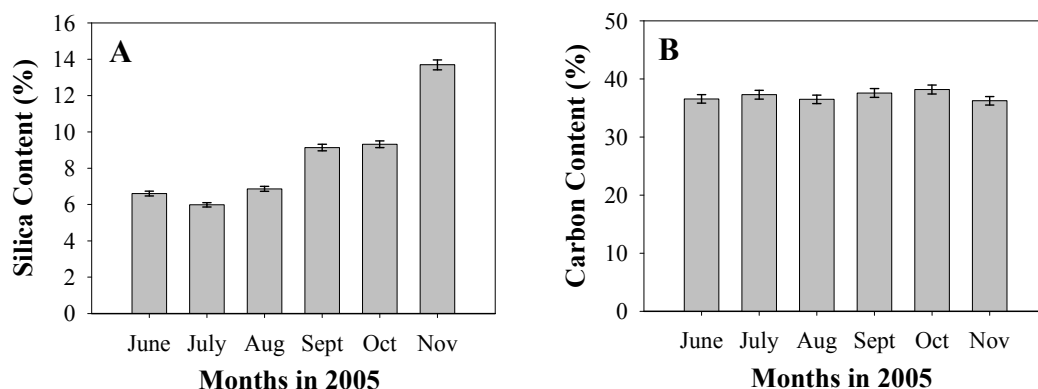


Figure 2.1 Average silica contents (A) and average carbon contents (B) of *E.hyemale* shoots harvested in June until November 2005. The silica content was determined chemically by means of a gravimetric method. Five grams of fresh material was treated chemically with 10% HCl to remove the other inorganic impurities, and then oxidised in air (750°C, 2 h) to obtain pure silica. The silica content was calculated from the mass loss.

The silica content of different segments from top to base within stalks of mature shoots harvested in the middle of November 2005 was also determined. Both nodes and internodes were dissected into five different segments, i.e. top, upper middle, middle, lower middle, and base. Each segment consisted of about 2-3 nodes/internodes depending on the stalk lengths, which comprised of normally 10-12 internodes (Fig. 2.2). The cones were excluded and its average silica content was determined separately. The macroscopic silica distribution from top to base within *E.hyemale* stalks is shown in Fig. 2.3.

The silica contents decreased from about 15% at the top part to about 10% at the base part in both mature nodes and internodes (Fig. 2.3 (A)). There were only slight differences in silica contents between nodes and internodes. Moreover, the cone where the spores are collected comprised of relatively high silica of about 11%. It is known that in *Equisetum*, the way out shoots elongate can be crudely compared to the extension of the tapering telescope⁹². The older, more extended internodes occur at the base of the shoot, while younger, less extended internodes are the last to be exposed and are found progressively toward the tip⁹². However, there was no gradient in maturity anymore from top to the base when the shoots ceased elongating since the whole stalk was mature for the investigated *E.hyemale* stems. It is therefore interesting to note that there was a degradation pattern of silica content from top to base even though the stems maturity had been reached about 3 months before. Furthermore, carbon contents of different segments were relatively constant within nodes as well as internodes, though carbon was quite less at the top part of nodes (Fig. 2.3 (B)). This carbon content could be attributed either from biopolymer fibers in the cell walls, cuticular fatty acids or the nutrients such as polysaccharides and protein. The mature internode shows significant denser sclerenchyma cell walls at the hypodermal tissues below epidermis compared to the young one (Fig. 2.4). This implies that the cell wall fibers in mature internodes are mostly contributing to carbon content rather than nutrients which are supposed to be richer in the young internodes.

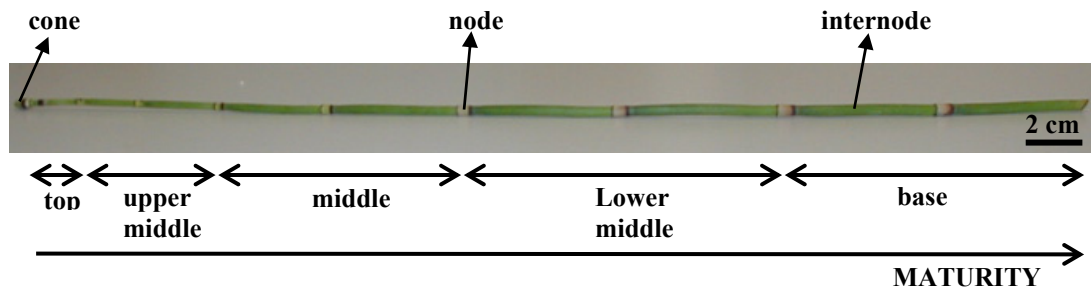


Figure 2.2 A photograph of a stalk of *E.hyemale* divided into 5 different segments for the macroscopic silica distribution determination in nodes and internodes from top to base parts.

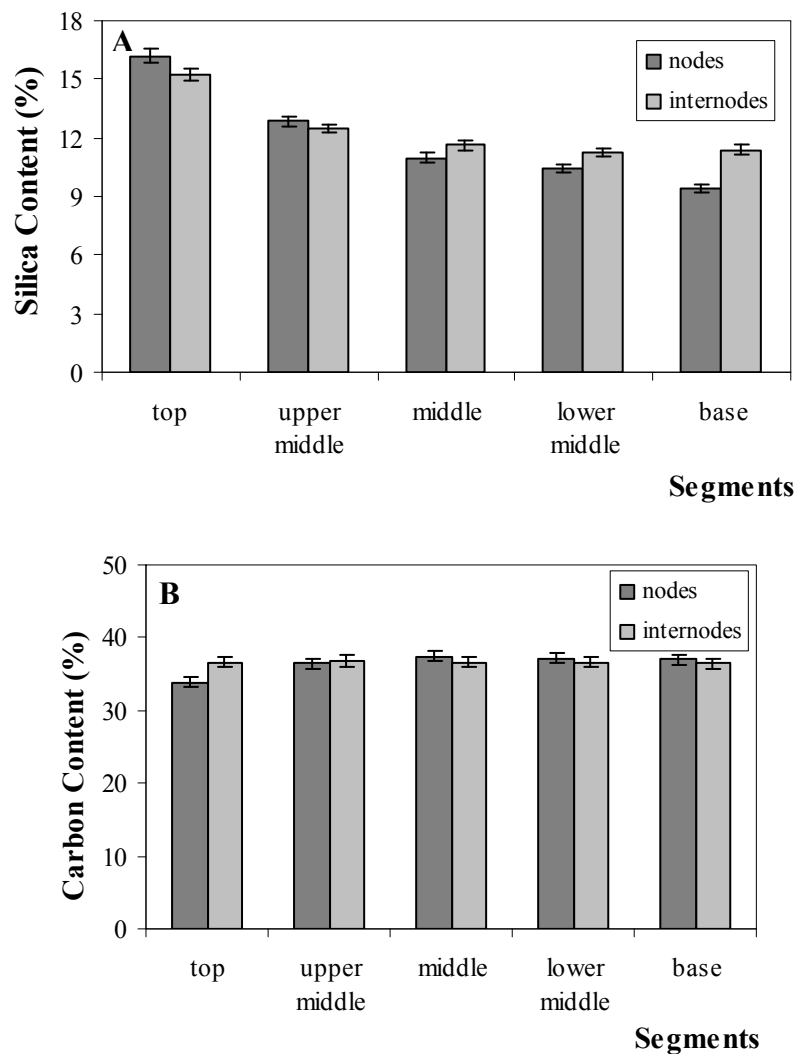


Figure 2.3 Macroscopic silica distribution (A) and carbon distribution (B) in nodes and internodes from top to base parts of *E.hyemale* stalks harvested in the middle of November 2005. *E.hyemale* stalks were dissected into five different segments for both nodes and internodes parts for the average silica content determination by means of chemical analysis. Five grams of fresh material was treated chemically with 10% HCl to remove the other inorganic impurities, and then oxidised in air (750°C, 2 h) to obtain pure silica. The silica content was determined by gravimetric method.

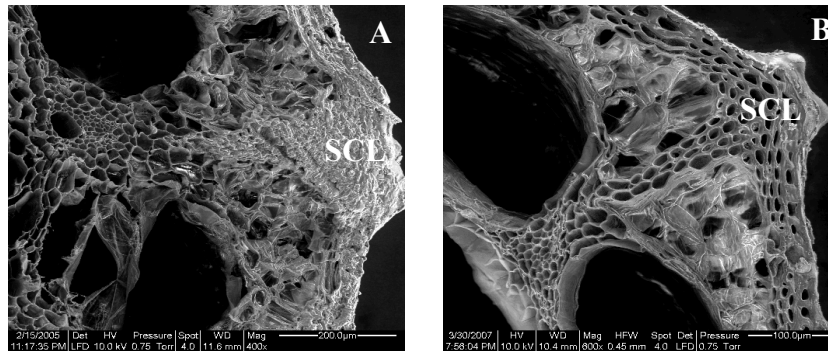


Figure 2.4. SEM images of cross sections of (A) mature internode and (B) young internode. Densification of the sclerenchyma (SCL) cell walls is marked in the mature internode and considered as one of the differentiation phase during stem maturation.

Additional to the chemical analysis, a comparative study on silica distribution of different internodes (top, middle, base) between young (one-month-old shoot) and mature (six-month-old shoot) was performed by using X-ray microtomography. The young shoot was still developing and the maturity was going basipetally while the mature ceased elongating already. Figure 2.5 (A) shows a 3D rendering from microCT of a dry stem, demonstrating the corrugated structure of the native *E. hyemale* stem outer surface. The ribs portions are occupied by two parallel rows of knobs, while the stomata row lies on each of the rib's flanks. The plant has a relatively thick and dense epidermis in contrast to its interior tissue parts. Figure 2.5 (B) shows a two dimensional reconstructed cross section of a native stalk in a water-filled tube. The colour code displays the different X-ray absorption values, being related to the local density and composition. The absorption coefficients of water and the polymer tube are very similar to those of the biopolymers in the specimen, differing only by typically 10-20%. In contrast, the linear absorption coefficient of silica is higher by at least a factor 5-7 at the relevant X-ray energies. Therefore, neglecting possible influences from other inorganic substances accumulated in the stalks, the contrast in Fig. 2.5 (C-H) can be taken as a qualitative measure of the local 3D silica distribution with a voxel size of about $(10 \times 10 \times 10) \mu\text{m}^3$. The inner tissue parts of the stalks are not visible anymore, indicating very low silica concentrations there. In the epidermal layer, the absorption contrast varies considerably, revealing highest silica concentrations in the knob regions, followed by the area between the knobs and finally the rest of the epidermis with a rather continuous and homogeneous silica layer.

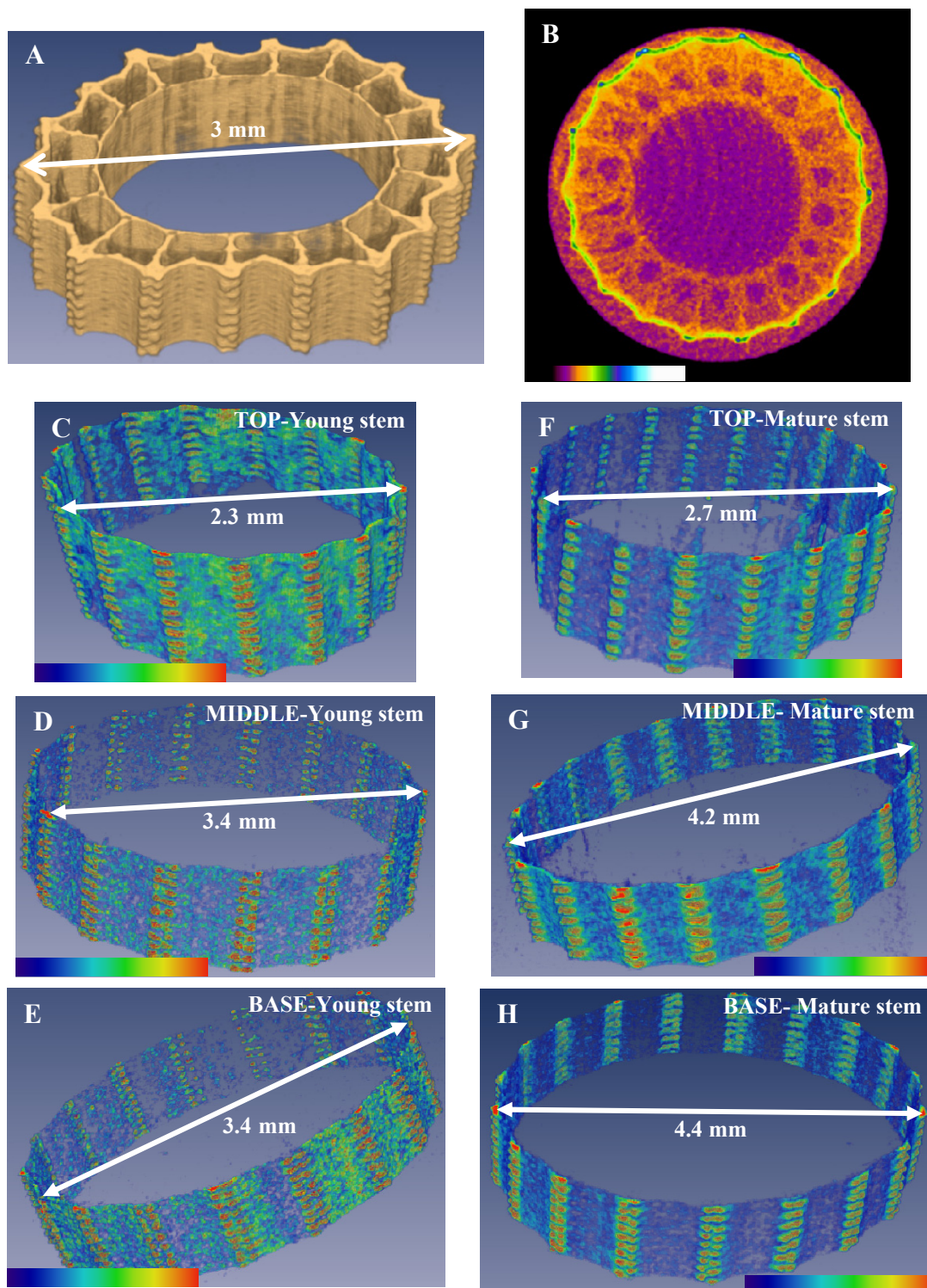


Figure 2.5 (A) 3D rendering of an X-ray micro-CT reconstructed image of a dry *E.hyemale* stalk. (B) A two dimensional reconstructed cross section of a native stalk in a water-filled tube. (C-H) Comparisons of three dimensional visualisations of qualitative silica accumulation in the epidermal layer of different internodes parts (top,middle,base) of *E.hyemale* between a developing stalk (C,D,E) and a mature one (F,G,H) in water-filled tubes acquired by X-ray micro-CT.

The pseudo-coloured 2D μ -CT image depicted in Fig. 2.5 (B) reflects "greyscale values" ranging from 0-256 depending on the different intensity of X-ray measured at each pixel. Thus, the 2D image can be reduced into a distribution of greyscale values. Since silica absorbs X-ray by far stronger than the plant biopolymers as well as water and the polymer tube, the area exclusively occupied by silica within the *E.hyemale* tissues can be analysed quantitatively based on the analysis of the greyscale histograms.

The reconstructed 2D slices of the *E.hyemale* stalks were confined within a selected region of interest in the form of a circle by assuming the stalks to be circular with the outer radius R only slightly larger than the outer radius of the stalk (Fig. 2.6 (A)) using the CTAn software (Skyscan, Belgium). Only the area restricted within this region of interest was taken into account for the analysis of the greyscale histograms. The area of 360 two dimensional slices corresponding to their greyscale values of each sample were averaged and normalised with respect to the area of the circular region of interest due to the variable sizes of the stem diameters of different samples. This leads to a parameter α , which allows to compare the greyscale histograms of different segments of the samples. Fig. 2.6 (B) shows an example of the greyscale histogram analysis of the top internodes of young and mature stems. The threshold of greyscale regions between 0-120 and 120-150 as showed by the inset in the histogram (Fig. 2.6 (B)) were chosen to select the strongly silicified regions in the knobs (Fig. 2.6 (C)) and the less silicified regions in the continuous layer (Fig. 2.6 (D)), respectively. The greyscale value of 150 was chosen as the maximum cut-off boundary for silica in the epidermal layer based on our visual inspection, despite the fact that the contrast might be also influenced by the dense association of biopolymers like cellulose, pectin, and cuticular compounds in the outer continuous epidermal layer. Above this value, the schlerenchyma tissues appeared in the images followed by water with its distinct peak lying approximately within 160-210 (Fig. 2.6 (B)). The lower area in the peak from water observed in the young stem (red curve in Fig. 2.6 (B)) is due to the formation of significant air bubbles (Fig. 2.6 (A)), which is nicely seen in the non-vanishing α -values between 210-250 and the rest region which was cut off from the image (Fig. 2.6 (B)).

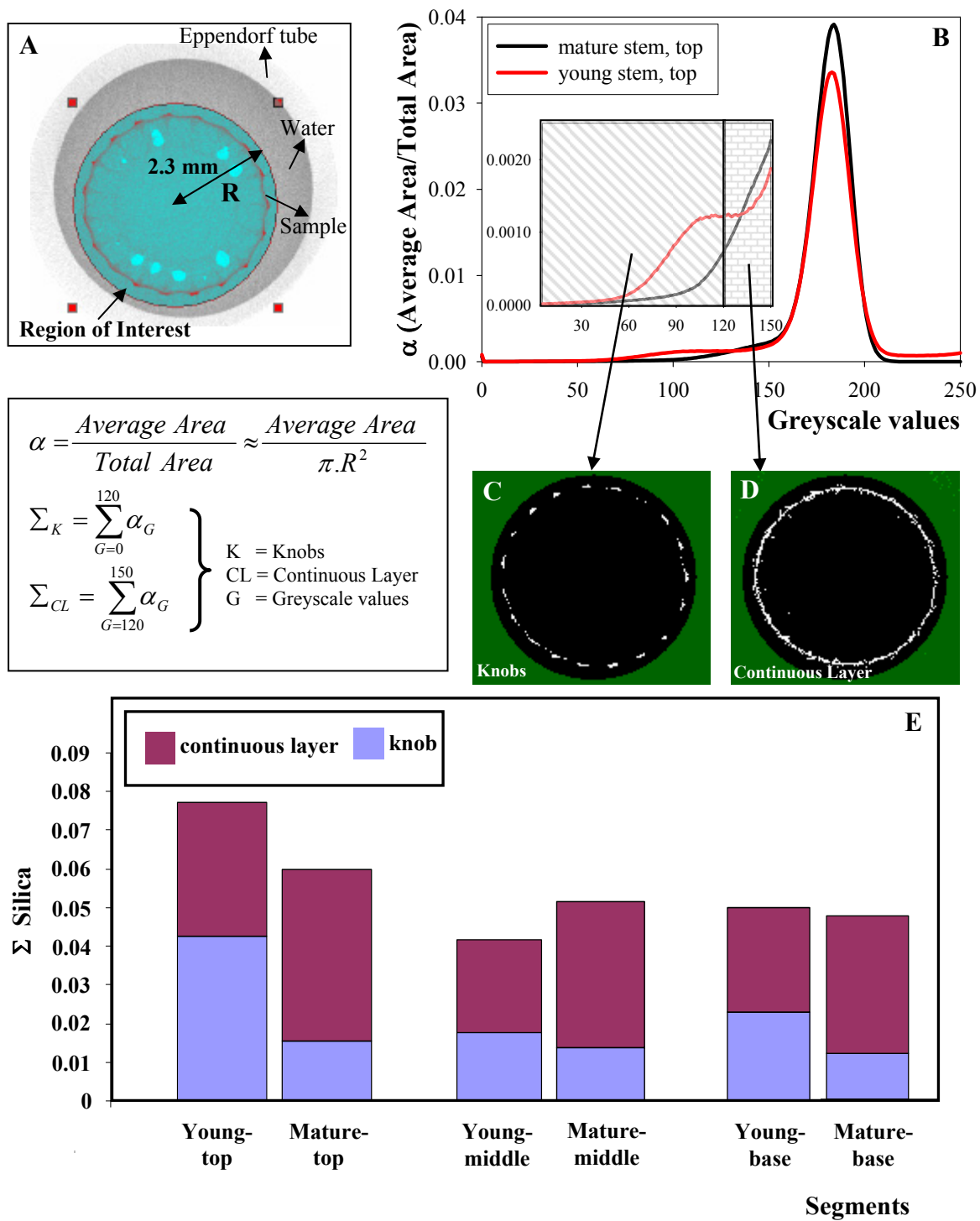


Figure 2.6 Semi-quantitative greyscale value analysis of silica distribution in different internodal segments (top, middle, base) of young (one month old) and mature shoots (six months old) of *E.hyemale* acquired by micro-CT (Figure 4.5). This analysis was conducted using the CTAn software (Skyscan, Belgium) based on the reconstructed 2D images confined within a circular region of interest (A). The plot of the average area from 360 slices relative to the total area of the circular region of interest (α) is plotted as a histogram function of greyscale values (0-256) (B). The inset indicates the magnification of those greyscale value regions which were used to distinguish between silica deposited in the knobs and in the continuous epidermal layer, with greyscale values lying within 0-120 (C) and 120-150 (D), respectively. The sum of α (Σ silica) within the respective greyscale value regions in different segments of both young and mature stems are plotted and compared in (E).

Table 2.1 Comparison of silica contents in different internodal segments (top, middle, base) of young and mature stems with respect to their deposition pattern within knobs and continuous epidermal layer based on the greyscale values analysis (CTAn, Skyscan).

Segments	$\frac{\Sigma_{young}}{\Sigma_{mature}}$	$[SiO_2]_{mature}$ (chemical analysis)	$[SiO_2]_{young}$ (estimated)	$\left(\frac{\Sigma_{CL}}{\Sigma_K}\right)_{young}$	$\left(\frac{\Sigma_{CL}}{\Sigma_K}\right)_{mature}$
Top	1.3	15.3 %	19.6 %	0.8	2.9
Middle	0.8	11.6 %	9.9 %	1.4	2.8
Base	1.0	11.4 %	11.6 %	1.2	3

CL= continuous epidermal layer; K= knobs

The cumulative α values (Σ) within greyscale intervals of 0-120 and 120-150 were determined to distinguish the amount of silica deposited in the knobs and in the continuous layer, respectively in a semi-quantitative way. This semi-quantitative analysis allowed getting more meaningful data to differentiate and compare the portions of silica deposited in the knobs and the continuous layers within different parts (top, middle, base) of young and mature stems (Fig. 2.6 (E)) rather than just estimating their values by having a look at the qualitative 3D rendering μ -CT images (Fig. 2.5 (C-H)).

Fig. 2.5 (C-E) indicates a difference in the silica distribution between the internodes from the top compared to the internodes from the middle and base parts within the developing *E.hyemale* stalk. This is consistent with the semi-quantitative greyscale analysis (Fig. 2.6 (E)). The top part contained the highest amount of silica deposited in the knobs as well as the continuous epidermal layer among the other segments within young shoot (Fig. 2.6 (E)). This decreasing pattern of silica distribution from the top to the base parts, which is hardly seen in the 3D rendering μ -CT images (Fig. 2.5 (F-H)), was also observed in the mature stem based on the greyscale values analysis (Fig. 2.6 (E)) and was fully consistent with the chemical analysis (Fig. 2.3 (A)). There is quite a difference in silica content of the top internodes (Fig. 2.5 (C) vs. (F) and Fig. 2.6 (E)) between the young and mature stems, while the middle and base parts show rather small differences (Fig. 2.6 (E)). Interestingly, the silica deposited in the continuous epidermal layer became more conspicuous in all segments within the mature stems in contrast to the young stems which predominantly deposited silica in the knob parts (Fig. 2.6 (E) and Table 2.1), even though the continuous layer of the young stem shows a higher contrast qualitatively compared to the mature one within the top part (Fig. 2.5 (C) vs. Fig. 2.5 (F)). The silica deposited in the continuous epidermal layer

was consistent in the top, middle, and base segments of the mature stem with a factor of about 3 higher than those deposited in the knobs (Table 2.1). The more homogeneous silica distribution within the continuous “silica layer” over the whole internodes are obviously seen in the middle and base internodes of the mature stalk compared to the young one (Fig. 2.5 (D-E) vs. Fig. 2.5 (G-H)). In general, silica gradient appeared to be diminished from the top to the base parts and the silicification pattern within the internodes became more homogeneous over the whole continuous epidermal layer as the *E.hyemale* shoots were getting mature.

2.2 Microscopic investigations of silica in *E.hyemale*

Scanning electron microscopy (SEM) in secondary electron mode and in the backscattered electron (BSE) mode as well as energy dispersive X-ray (EDX) analysis for the Si mapping and semi-quantitative analysis were performed to study the silica distribution and its accumulation pattern at the microscopic level in *E.hyemale*.

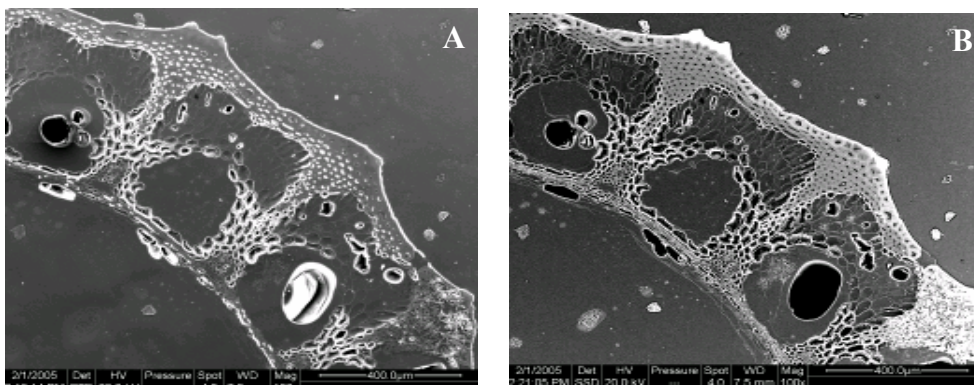


Figure 2.7 Embedded and polished cross section of *E.hyemale*. (A) Secondary electron image; (B) Backscattered electron image.

Fig. 2.7 (A) shows a secondary electron image of the embedded and polished *E.hyemale* cross section, and Fig. 2.7 (B) shows the BSE image of the corresponding cross section. The BSE image contrast is dependent on the mean atomic number, thus regions containing high amount of silica should exhibit higher contrast compared to the low silica containing regions. It is obvious that the outer surface of the epidermis, in particular the bituberculate knobs lying on the ribbed portions show significantly higher contrast and indicate thus a strong silica deposition pattern, which is in agreement with

the micro-CT results. Nevertheless, this contrast might also derive from other inorganic substances present in the sample, which have similar or even higher mean atomic number. Therefore, Si mapping using EDX as well as a semi-quantitative elemental analysis with EDX was performed to support this result.

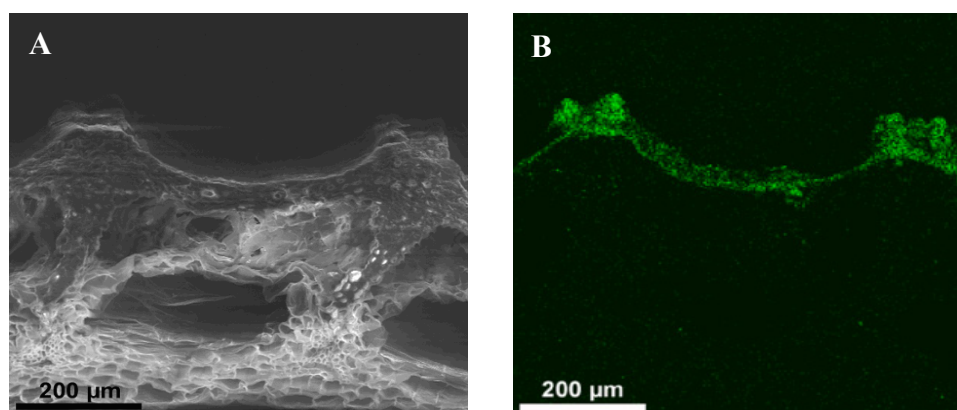


Figure 2.8 Secondary electron image (A) and EDX map of Si (B) of a cross section of *E.hyemale* showing the Si depositions on the epidermis with the strongest accumulations at the knob tips.

Fig. 2.8 (A) shows a SEM image of a cross section of *E.hyemale* stalk and Fig. 2.8 (B) shows the mapping of Si within this specimen. Si is rather homogeneously distributed (on a resolution scale of about 3-4 μm) in the epidermal layer with particularly high amount in the knobs. There was almost no Si detected in the entire interior part of the plant tissue. To quantify the Si distribution pattern on the epidermal layer, a semi-quantitative elemental analysis with EDX was performed directly on the outer surface (Figure 2.9 (B),(E)). Si reached concentrations up to 33% at the knob tips (Fig. 2.9 (A)), whereas the epidermal flank contained about 17% (Fig 2.9 (C)). Analysing the cross section (Fig. 2.9 (D),(F)), the Si content was observed to decrease from the outermost surface towards the interior. It was found that the Si content at the lower inner part of the knob was around a factor of 5 less than that of the knob tips (6%, Fig. 2.9 (F)). Si was found only in trace amounts in the walls of sclerenchyma cells (Fig. 2.9 (D)) and there was no silica at all in the interior parts (data not shown). These results agree with the qualitative Si mapping, BSE image and with the microCT results that silica is accumulated exclusively in a thin continuous layer in the outermost epidermis and is particularly concentrated on the knob tips with almost pure silica. There was practically no carbon and no inorganic elements in the knob tip region (Fig. 2.9 (A)). In contrast, the epidermal flank showed an increased carbon peak and also

some amount of K and Ca (Fig. 2.9 (C)). The inner part of the knob and the sclerenchyma cell wall contained significantly higher concentrations of both C as well as alkali and alkaline-earth metals, for instance Ca, K, Na, Mg and non metal elements, such as P and S (Fig. 2.9 (F),(D)).

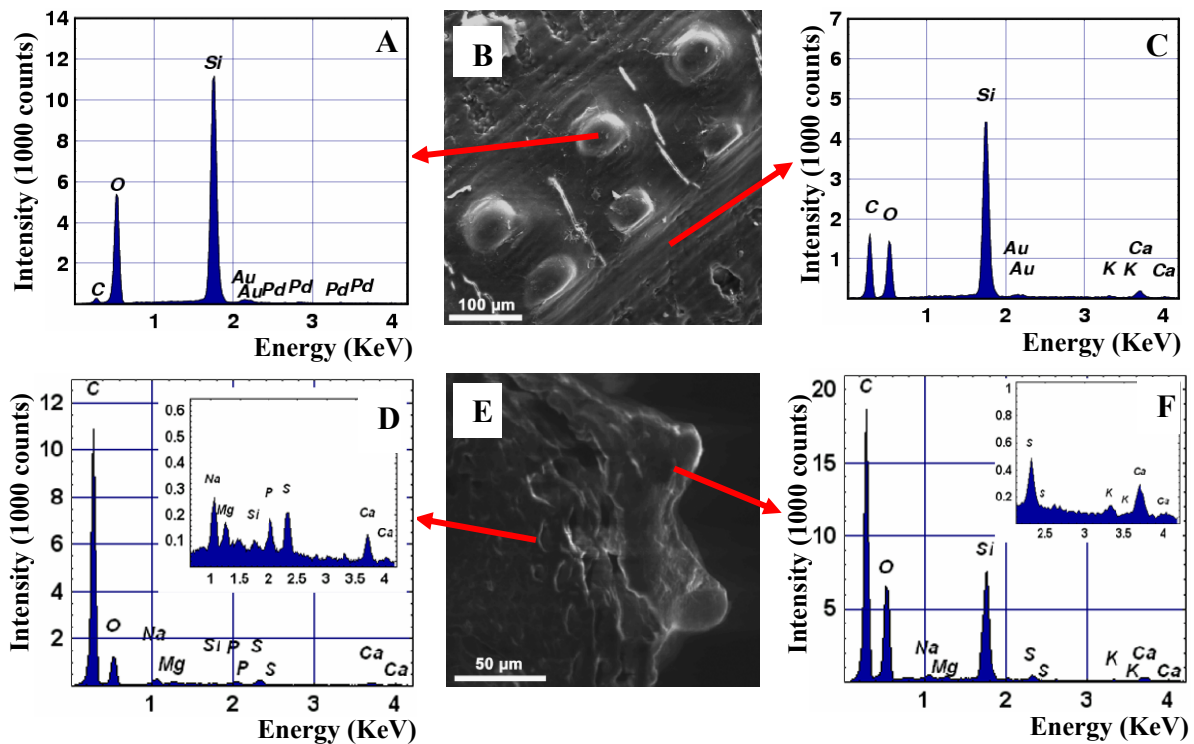


Figure 2.9 Secondary electron images of (B) the outer surface and (E) the cross section of *E.hyemale*. (A,C,D,F) show EDX spectra at different positions indicated by the arrows at the knob tip (A), epidermal flank (C), lower inner part of the knob (F), and sclerenchyma cell wall (D). Insets are magnified parts of the EDX spectra of the elements found in low concentrations. The Au- and Pd-signals in the spectra originate from the sputtering of the samples with a thin Au/Pd film. The silica content in weight percent relative to all elements detected within the local illuminated sample volume was calculated for A,C,D,F as 33%, 17%, 0.1%, and 6% \pm 2%, respectively.

2.3 Molecular investigations of silica in *E.hyemale*

Having obtained a general overview of silica distribution in macroscopic and microscopic levels, spectroscopic techniques were employed for the study of silica at the molecular level. Confocal Raman microscopy and FTIR were applied to get complementary information on the silica characteristics together with the fingerprints of other molecules present in the epidermal layer. This enables to identify the specific

silica forms, particularly those mostly accumulated in the knobs of the ribbed portions and to study the possible interactions of silica with the organic or inorganic compounds.

2.3.1 Confocal Raman Microscopy

Raman microscopy is advantageous compared to FTIR as it allows obtain chemical images with very high spatial resolution ($< 1 \mu\text{m}$). Moreover, it is possible to measure the sample in the wet state and thus, information about the unaltered native state of the specimen can be obtained. The confocal arrangement allows to perform a depth scan within the knob region to image the chemical distributions of amorphous silica, silanol groups, and polysaccharides (cellulose, hemicellulose, and pectin) by integrating over $245\text{-}570 \text{ cm}^{-1}$ (Fig. 2.10 (A)), $937\text{-}993 \text{ cm}^{-1}$ (Fig. 2.10 (B)) and $1054\text{-}1191 \text{ cm}^{-1}$ (Fig. 2.10 (C)), respectively^{95,96,97}.

It is obvious that the distribution of the amorphous silica (Fig. 2.10 (A)) is highest on the tip of the knob and decreases with distance from the tip. The epidermal flank also showed a clearly higher intensity from amorphous silica. The intensity of the band attributed to the silanol group (Fig. 2.10 (B)) was restricted to the knob tip and hardly detected in the other regions. In contrast, there was nearly no polysaccharides detected in the tip of the knobs, whereas the lower inner part of the knob and especially the epidermal flank showed a higher signal from polysaccharides (Fig. 2.10 (C)). It is also interesting to note that within the knob, polysaccharides are increasing from the outermost part to the inner part (Fig. 2.10 (C)), just opposite to the gradient of the amorphous silica (Fig. 2.10 (A)). The small layer on the top of the knob in Fig. 2.10 (C) represents epicuticular waxes, which have spectral contributions interfering with other organics, e.g. polysaccharides.

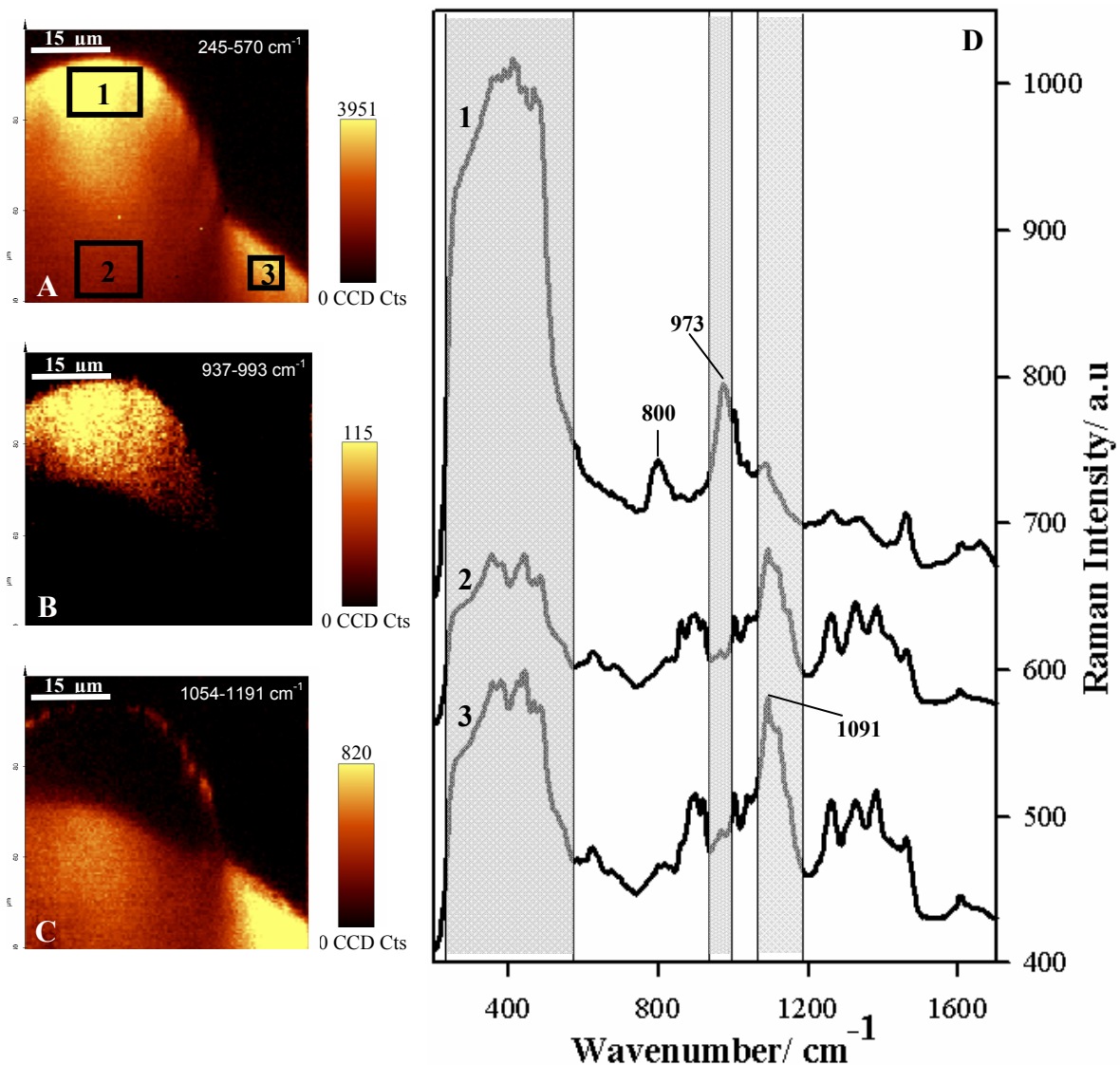


Figure 2.10 Raman images (A-C), and average spectra (D) of different knob areas calculated after a depth scan through a knob of a tangential *E.hyemale* section in the wet state. The distribution of amorphous silica, silanol groups within amorphous silica and cellulose were imaged by integrating over 245-570 cm^{-1} (A), 937-993 cm^{-1} (B), and 1054-1191 cm^{-1} (C), respectively (grey regions in D). Average Raman spectra were extracted from different regions defined in the image (A) and are shown in (D): (1) knob tip; (2) lower inner part of the knob; (3) epidermal flank.

Average spectra from regions which differed considerably in their chemistry in the imaging technique were extracted by marking selected areas in the chemical image (boxes in Fig. 2.10 (A)). Average spectra of the knob tip (spectrum 1), lower inner part of the knob (2), and epidermal flank (3) are shown within the fingerprint region (200-1700 cm^{-1}) in Fig. 2.10 (D). Raman spectra above 1700 cm^{-1} were dominated by doublet bands of organics at 2921 and 2947 cm^{-1} and water within 3000-3700 cm^{-1} , which appeared in all regions (1-3), thus did not contribute much for the chemical composition

differentiation. The average spectrum of the knob tip region (1) shows some prominent characteristic peaks of amorphous silica in a broad band within the region 250-500 cm^{-1} , which is attributed to the in plane Si-O-Si bending⁹⁵. A vibrational peak at 800 cm^{-1} corresponds to tetrahedral SiO_4 moieties⁹⁸, and a strong band at 973 cm^{-1} is typical for silanol groups as found for instance in silica gel⁹⁵. The other accompanying peaks in spectrum (1) are tentatively all attributed to organics, but polysaccharides were barely found in this area (compare Fig. 2.10 (C)). For instance, the rather isolated strong peak at 1460 cm^{-1} might be attributed to a special plant wax⁹⁹.

The two spectra of the inner knob (spectrum 2) and epidermal flank (spectrum 3) showed spectral similarities. Both demonstrated the presence of amorphous silica from the broad band in the region of 250-500 cm^{-1} , but they both lacked the characteristic peak of the silanol groups at 973 cm^{-1} and showed just a small band at 966 cm^{-1} , which could derive from the polysaccharides. The tetrahedral SiO_4 moiety peak at 800 cm^{-1} was very weak in epidermal flank region (3), and was absent on the inner part of the knob (2). Both regions showed strong bands around 1100 cm^{-1} arising from cellulose, hemicellulose and pectin^{96, 97}. Raman bands for cellulose can be seen at 440, 892, 1118, and 1380 cm^{-1} ⁹⁶. The glucomannan peak observed at 2918 cm^{-1} supports the presence of hemicellulose⁹⁷. The characteristic band for acidic pectin is detected at 859 cm^{-1} ¹⁰⁰ and is clearly seen in the lower part of the knob and as a shoulder in the epidermal flank. Furthermore, the contribution at 898 cm^{-1} is found also just in the lower part of the knob and the epidermal flank and may indicate the presence of calcium-oxalate¹⁰¹. Moreover, small amount of calcium phosphate may also present in both lower part of the knob and the epidermal flank due to the weak Raman band arising at 968 cm^{-1} ¹⁰². Some of the remaining, non-identified peaks presumably arise from cutin and waxy materials, which may differ in the different plant regions¹⁰³.

Finally, a crystalline silica polymorph in the form of α -quartz was detected in an inclusion above a stomatal opening by Raman microscopy (Fig. 2.11 (A)). The Raman spectrum shows the characteristic fingerprint of α -quartz with a typical sharp peak at 472 cm^{-1} ¹⁰⁴. Organic substances with their characteristic peaks at around 2900 cm^{-1} ⁹⁶ were found neither in this crystal nor in the guard cells, in contrast to the subsidiary cells of stomata (Fig. 2.11 (B)).

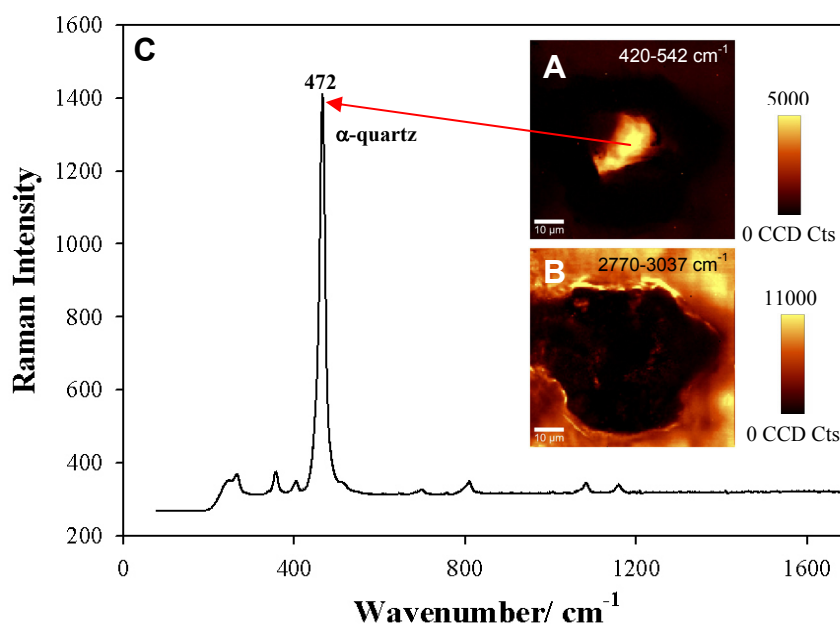


Figure 2.11 Raman images (A-B) and average spectra (C) of α -quartz detected in an inclusion above a stomatal opening. The distribution of crystalline silica, i.e. α -quartz were imaged by integrating over 420-542 cm^{-1} (A), while the distribution of CH_2 groups of organic substances were mapped by integrating over 2770-3037 cm^{-1} (B). Average Raman spectra of α -quartz were extracted from the middle region of the inclusion with the highest intensity in the image A.

2.3.2 FTIR

FTIR was employed as a complementary technique to Raman microscopy since most frequently; IR spectra can be used to differentiate biopolymers, which are indistinguishable in the Raman spectra and vice versa besides its ability to give many Si-O vibrational modes, thus additional useful information can be obtained. Additionally, IR shows no problems with fluorescence radiation in contrast to Raman spectroscopy when dealing with biological tissues, leading to an improved signal-to-noise (S/N) ratio. Local IR measurements were done on the epidermal layer focused on the outer surface of the knobs and epidermal flanks by using an ATR objective. IR light transmitted by the ATR crystal during contact with the samples was penetrating the outer surfaces of the samples for several μm before being reflected back to the system. The obtained spectra were compared with the FTIR spectrum of silica powder derived from *E.hyemale* (Fig. 2.12), which was used as a standard material showing the characteristic fingerprint of amorphous silica. The purification processes of native

E.hyemale shoots to get pure biogenic silica by means of chemical and thermal treatment along with their nanostructural characterisation will be discussed in more detail in the next chapter.

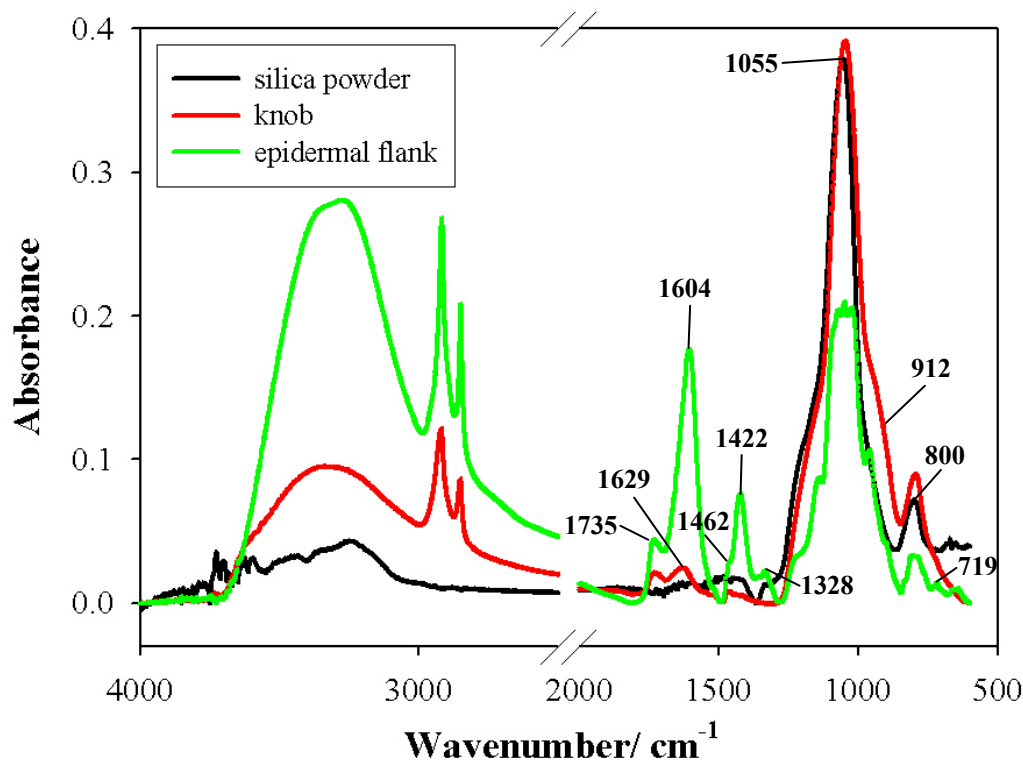


Figure 2.12 FTIR spectra of silica powder, knob, and epidermal flank taken by using ATR mode. The ATR objective was located exactly at the regions of interest by viewing the sample through the ocular or monitor under the visible light mode. Silica powder was derived from the calcination of HCl-treated *E.hyemale* at 600°C for 2 hours with a heating rate of 2 K/min. A thin epidermal layer was prepared and used for the local IR spectra measurements in the outermost part of knob and epidermal flank. The spectral region between 2000 and 2500 cm^{-1} were cut off due to the high absorbance signals derived from CO_2 at 2362 and 2341 cm^{-1} .

The region within 1250 and 850 cm^{-1} is assigned to a complex and strong vibration of Si-O¹⁰⁵. There are several absorption bands attributed to hydrated amorphous silica within the range of 4000 cm^{-1} to 600 cm^{-1} : a sharp signal in the region 1100-1000 cm^{-1} and a weaker signal at $\sim 800 \text{ cm}^{-1}$ due to siloxanes $-(\text{SiO})_n-$ and a silanol band at 955 – 830 cm^{-1} ¹⁰⁶. Furthermore, water associated with hydrated amorphous silica is mostly detected at 1630 cm^{-1} due to a H-O-H bending band, which are attributed to the hydrogen-bonded hydroxyl groups and physically adsorbed water

molecules besides a broad peak at the around the centre of 3400 cm^{-1} due to OH⁻ stretching band^{107, 108}.

The outer surface of the knob represented almost pure hydrated amorphous silica, showing rather broad silica bands at 1045 cm^{-1} and 793 cm^{-1} , silanol group at about 912 cm^{-1} , adsorbed water at 1629 cm^{-1} and a broad water band within $3700 - 3000\text{ cm}^{-1}$. Some organics derived from the epicuticular waxes on the outer surface marked by the presence of strong doublet organic bands at 2925 and 2855 cm^{-1} ¹⁰⁹ and a small peak around 1732 cm^{-1} was proposed to be attributed to the cuticular related organic compound⁹⁹. There was no cellulose or other cell wall biopolymers detected in the knob tip. In comparison to the silica powder, the siloxanes $-(\text{SiO})_n-$ bands of typical amorphous silica at around 1050 and 800 cm^{-1} are slightly shifted to the right within the knob tip. Probably, the knob tip also contained some impurities derived from the trace inorganic compounds containing Ca and K which could shift the absorption bands of amorphous silica to lower wavenumbers.

In contrast to the knob tip, the outer surface of the epidermal flank displayed a rather complex spectrum of amorphous silica which was associated with organic as well as inorganic substances. The characteristic silica peaks centred at about 1045 cm^{-1} and 793 cm^{-1} were obviously seen as in the case of amorphous silica in the knob tip. The amorphous silica found in this epidermal flank lacked silanol band. However, it showed a much higher water band within $3700 - 3000\text{ cm}^{-1}$ compared to the knob tip, indicating the presence of a greater amount of OH⁻ groups ascribed to alcohol, cellulose, and other hydroxyl containing compounds. Moreover, the C-H stretching doublet bands at 2925 and 2855 cm^{-1} ⁹⁶ were increased influenced by a greater quantity of organics present in the epidermal flank. Cellulose prominent peaks appeared at 1050 , 900 and 1328 cm^{-1} ¹¹⁰. Furthermore, the epidermal flank was incredibly rich in pectin marked by the appearance of pectic polysaccharides bands at 1144 , 1072 , 1050 , 1022 and 958 cm^{-1} ¹⁰⁰. Additionally, strong bands at 1604 and 1422 cm^{-1} due to the acidic groups of polygalacturonic acids were also associated with the pectinic acids¹⁰⁰. Hemicellulose may also be present as suggested by the absorption band of carbonyl bonds at 1735 cm^{-1} ¹⁰⁹. IR bands at 1735 , 1462 and 719 cm^{-1} are possibly due to cutin, wax or other related cuticular compounds⁹⁹. Furthermore, minerals such as calcium oxalate and calcium phosphate - which were detected by Raman - are not easily observable in the FTIR

spectra since they are mostly overlapped by the organics spectra. For instance, the IR band of calcium oxalate at 1328 cm^{-1} ¹⁰² overlapped with the spectra of cellulose. Calcium phosphate was not virtually seen at 1035 cm^{-1} ¹⁰², being most probably masked by either silica or organics bands. Moreover, FTIR measurements were also done on several local sites in the guard cells of stomata (data not shown) and their spectra exhibited similarities with those derived from the epidermal flanks.

The results obtained from the FTIR measurements agreed well with the results from Raman spectroscopy. Pure hydrated amorphous silica is confined to the knob tips, while silica deposited in the epidermal flanks lacks of silanol groups and is closely associated with biopolymers, such as cellulose, hemicellulose, and pectin. *E.hyemale* is strikingly rich in pectin mostly in galacturonic acid residues which is in agreement with previous findings¹⁹. Calcium oxalate and calcium phosphate are the most likely calcium containing mineral forms found on the entire continuous epidermal layer except the knob tips regions, which is consistent with the EDX results.

2.4 Crystallinity and nanostructural study of silica in *E.hyemale*

X-ray scattering was carried out to study the crystallinity by WAXS and to reveal the nanostructure of accumulated silica in *E.hyemale* by SAXS. Six powdered samples, namely native *E.hyemale*, epidermal layer, knob tips, ash, SiO₂/C and biogenic silica from *E.hyemale* were investigated. The epidermal layer was peeled off from the outer surface using a razor blade while the knob tips were mechanically isolated by scrapping off the ribbed portions with a razor blade. The ash was obtained by calcination of *E.hyemale* stalks at 400°C in air. SiO₂/C was prepared by applying a chemical treatment in 10% HCl to remove mainly all inorganic substances other than silica, prior to pyrolysis in Argon atmosphere at 400°C. Finally, biogenic silica was obtained upon calcination of the HCl-treated samples at 400°C in air. The chemically and thermally treated samples are included in this section under the assumption that the structure of the material after purification remains largely intact due to the mild treatments. This allows better understanding and interpreting the silica nanostructure within the complex native tissues of *E.hyemale*. The detailed investigations on HCl-treated *E.hyemale* as

well as biogenic silica from HCl-treated *E.hyemale* and ash obtained after the calcination of *E.hyemale* shoots at different temperatures ranging from 300 to 750°C will be described in more detail in Chapter 3.

The SEM images in Fig. 2.13 show impressively that the ash (Fig. 2.13 (B)) and the biogenic silica (Fig. 2.13 (C)) used for the nanostructural studies retained perfectly the original structure of native *E.hyemale* (Fig. 2.13(A)) even though the two rows of knobs have almost merged due to shrinkage. This indicates the accumulation of silica over the whole outer surface, forming a continuous siliceous layer. This is consistent with the results obtained from micro-CT, SEM/EDX, Raman and FTIR.

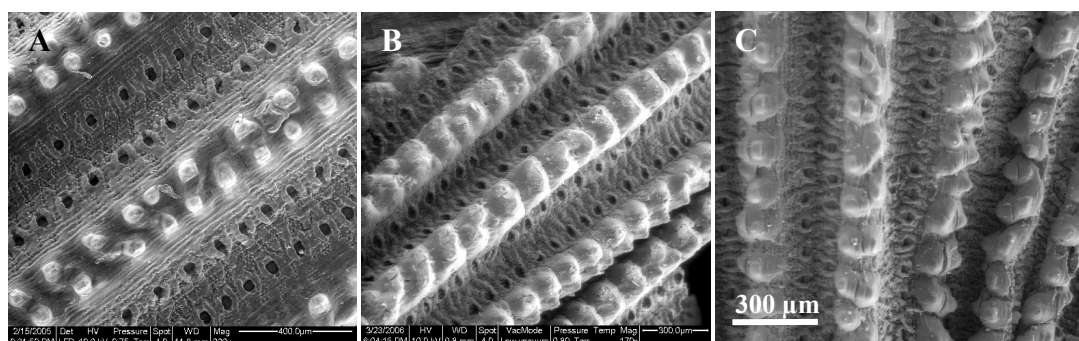


Figure 2.13 Secondary electron images of the outer surfaces of (A) native *E.hyemale*, (B) ash, (C) biogenic silica. Ash and biogenic silica samples were prepared by calcination of *E.hyemale* and HCl-treated *E.hyemale*, respectively at 400°C for 48 hours with a heating rate of 1 K/min.

Figure 2.14 (A) shows the WAXS profiles of these six powdered samples. The epidermal layer, which contains a high amount of silica, also contains a considerable amount of cellulose as evidenced by the broad peak at $q \approx 11 \text{ nm}^{-1}$, corresponding to the $101/10\bar{1}$ doublet from native cellulose¹¹¹. This diffraction pattern is very similar to the diffraction pattern of native *E.hyemale*. The second strong reflection from cellulose, i.e. the 002 reflection at $q = 16.2 \text{ nm}^{-1}$, overlaps with the broad peak from amorphous silica at $q = 15.5 \text{ nm}^{-1}$. In contrast, no cellulose peaks were observed for the knob tips, which agree with the Raman results. It shows a broad peak centred at $q = 15 \text{ nm}^{-1}$ which is attributed to amorphous silica¹¹². After ashing, all organic components, including cellulose were removed. A broad peak at $q = 15.5 \text{ nm}^{-1}$ in the WAXS pattern is attributed to amorphous silica, but there are several other, much sharper peaks visible in particular at higher q values. No detailed phase analysis could be performed due to the missing data at high q . Nonetheless, the detected peaks can be attributed to crystalline compounds, such as CaCO_3 , $\text{Ca}_3(\text{PO}_4)_2$, and KCl for instance. All elements present within

these compounds have also been detected by EDX in *E.hyemale* (Fig. 2.9). Interestingly, these sharp reflections are not visible in the diffraction pattern from the epidermal layer, suggesting that these crystals might have been formed only after the thermal treatment. The WAXS pattern of the HCl-treated and calcined sample (i.e. the profile denoted biogenic silica in Fig. 2.14) showed the fingerprint of pure amorphous silica with a broad peak at around $q = 15.5 \text{ nm}^{-1}$, identical to that obtained from sorghum and very similar to opal¹¹². No indications of other phases were present in this pattern. The WAXS pattern of SiO_2/C was very similar to that of biogenic silica. It appears slightly more diffuse due to the influence of diffraction from amorphous carbon showing a peak at $q \approx 16 \text{ nm}^{-1}$ ¹¹³.

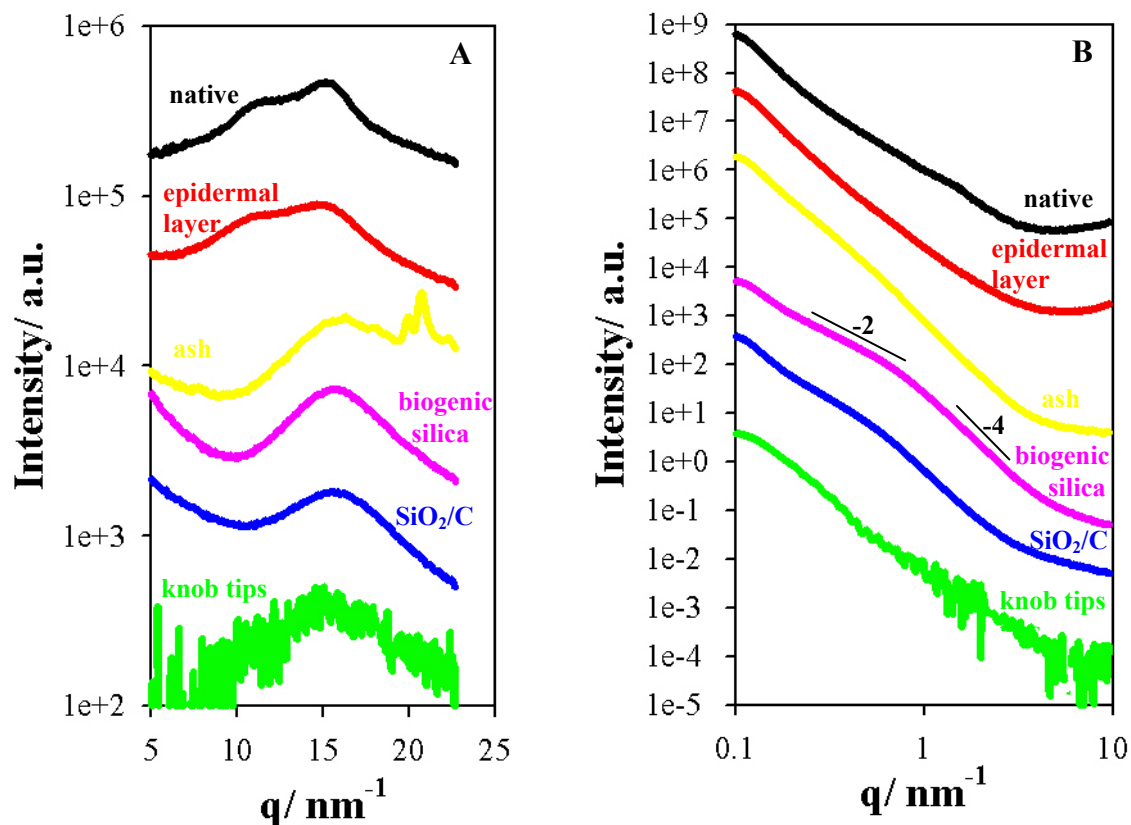


Figure 2.14 WAXS patterns (A) and SAXS patterns (B) from powdered specimens of the native, epidermal layer, ash, biogenic silica, SiO_2/C , and knob from *E.hyemale* internodes (see text). The lines in (B) indicate the power-law behaviour of the scattering intensity with $I \propto q^{-4}$ at large q for the ash and the biogenic silica samples (Porod's law), and a q^{-2} behaviour at low q for the biogenic silica sample. For the knob tips, counting statistics is poor, since only a very small amount of sample could be u

The SAXS profiles for these six samples are shown in Figure 2.14 (B). The ash as well as SiO₂/C and biogenic silica follow clearly Porod's law ¹¹⁴ for $q > 1 \text{ nm}^{-1}$, which means that there are sharp interfaces between spatially separated phases of different electron density. Also for the other samples, a q^{-4} region was present at large q -values after subtraction of a constant background. Porod's law together with the integrated SAXS intensity was used to determine the so called T-parameter (see Equation A.26 - A.28), which can be considered to be a measure for the smallest dimension of particles or interconnected domains ¹¹⁵. The T-parameters as well as BET surface areas from nitrogen sorption for all investigated samples were calculated and listed in Table 2.2. The detailed procedure for T-parameter calculation is described in Appendix C.

Table 2.2 T-parameter calculated from SAXS data and BET surface area

Samples	T parameter (nm)	σ_{BET} (m²/g)
Native <i>E.hyemale</i>	1.4	-
Epidermal layer	1.7	-
Knob tips	1.9	-
Ash, 400°C	4.9	33
SiO ₂ /C, 400°C	2.4	265
Biogenic silica, 400°C	2.1	375

The numerical values of the T-parameters obtained from the ash and the biogenic silica sample are most probably related to a mesoporous silica network, similar to many other types of silica gels. For the ash, this network contains also other inorganic phases such as calcium carbonates, and the corresponding T-parameter value indicates that these particles are considerably larger than the silica particles. No detailed nanostructural information about the silica in the native tissues (native *E.hyemale*, epidermal layer) could be deduced from the SAXS profile, since they consist of a mixture silica with organics (cellulose microfibrils, other cell wall biopolymers such as hemicellulose and pectin, and cuticular compounds). Additionally, also the inorganic substances contribute to the SAXS pattern in an unknown manner. Therefore, the values of the T-parameter from the native plant and its fragments (epidermis, knobs) cannot be interpreted in terms of a single average length scale in the system. It should be noted,

however that the T-parameter from the knob tip (1.9 nm) is very close to the one from the biogenic silica sample (2.1 nm). This underlines again the fact that the knob tips consist of almost pure silica, and indicates that there might be indeed only slight structural changes in silica structure during the chemical and thermal treatment. A second interesting point to be noted is that the scattering profiles of the biogenic silica and the SiO₂/C samples show a decrease of the scattering intensity proportional to q^{-2} at low values of q . This suggests planar or sheet-like structures¹¹⁴, with the T-parameter being a measure of the sheet thickness.

The picture of a highly porous silica gel for the biogenic silica sample is supported by the BET measurement, which shows high surface area of 375 m²/g, whereas the ash has only surface area of 33 m²/g (Table 2.2). The surface area of the native tissues (native *E.hyemale*, epidermal layer, and knob tips) were not measurable by nitrogen sorption, suggesting neglectable amount of open pores. This points to an intimate association of silica with the combination of both, biopolymers and inorganic compounds. The nitrogen sorption isotherm of biogenic silica (Fig. 2.15 (A)) shows a hysteresis loop type H3, indicating slit-shaped mesopores or plate-like particles¹¹⁶, which is in agreement with the SAXS analysis. The pore size distribution from the BJH analysis¹¹⁷ is shown in Fig. 2.15 (B) with the average pore size of about 8 nm.

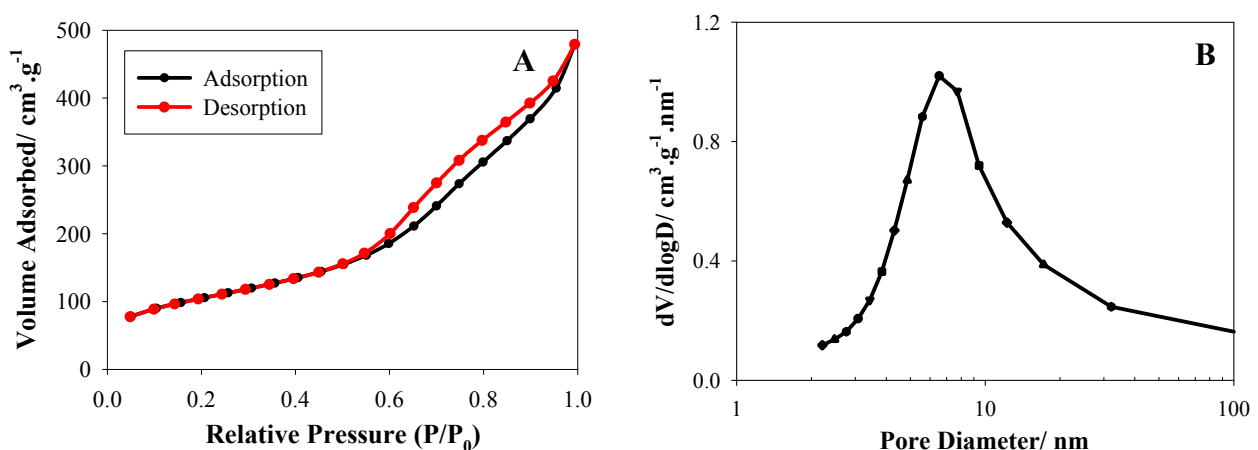


Figure 2.15 Nitrogen sorption isotherms of biogenic silica (A) and pore size distribution from BJH analysis of the sorption data from the adsorption branch (B). Biogenic silica used for nitrogen sorption study is exactly the same sample used for the nanostructural study by WAXS/SAXS.

2.5 H₂O₂-treated *E.hyemale*

A chemical treatment of young shoots of *E.hyemale* with 30% hydrogen peroxide was undertaken for the duration of 18 months by considering the use of hydrogen peroxide not only as a powerful oxidiser for both, organic and inorganic substances, but also the fact that the only by-product is water. A very thin and fully transparent continuous layer remained after the treatment, reflecting perfectly the original morphology of the epidermal layer (Fig. 2.16).

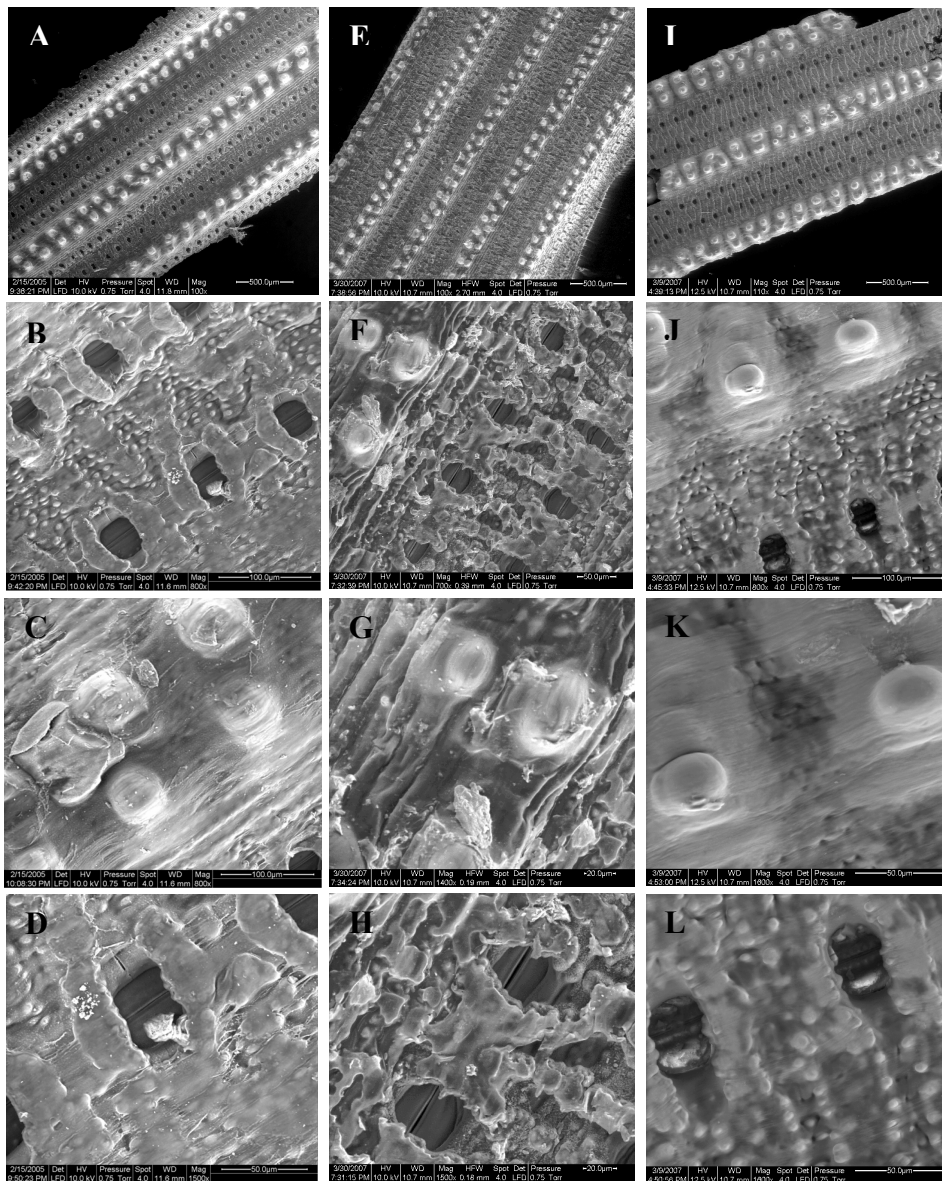


Figure 2.16 Secondary electron images of the outer surfaces of (A-D) mature *E.hyemale*, (E-H) young *E.hyemale*, (I-L) silica layer derived from young shoots. The outer surface of mature *E.hyemale* was taken from the basal internode of a six-month-old shoot while the young *E.hyemale* was taken from the middle internode of a one-month-old shoot. The silica layer was obtained after the treatment of a one-month-old *E.hyemale* shoot with 30% H₂O₂ for 18 months and was kept away from light exposure to slow down the decomposition of H₂O₂.

The “silica” layer appears to be fully intact by showing a smooth and continuous outer surface (Fig. 2.16 (I-L) vs. (A-H)). The knobs on the ridge portions and small wart-like protuberances occupying the rib’s flanks and furrow parts become more conspicuous compared to the native *E.hyemale* due to the removal of cuticular layer. The native *E.hyemale* shows a rougher surface predominantly determined by cuticular and waxy materials such as the wavelike linings in the ribbed region and opaque waxy materials covering the subsidiary cells of stomata and the furrow regions, which obscure the small warty protuberances on the grooves. The morphology of the young *E.hyemale* shows close similarities with the mature one (Fig. 2.16 (E-H) vs. (A-D)) but the outer surface appears to be coarser and not yet perfectly formed. The knobs look somewhat smaller and the waxy cuticles are arranged in a rougher and in more disordered manner compared to the outer surface of the mature stem.

Characterisations of powdered samples of H₂O₂-treated *E.hyemale* by using FTIR as well as SAXS/WAXS and nitrogen sorption were also performed. The FTIR spectrum is depicted in Fig. 2.17 together with the spectrum of silica powder derived from HCl-treated *E.hyemale* calcined at 450°C for comparison. The three typical bands of four-coordinated silica at 1102 cm⁻¹, 800 cm⁻¹, and 471 cm⁻¹ are obviously seen in both, the H₂O₂-treated *E.hyemale* and the silica powder samples and are assigned to the amorphous silica¹⁰⁷. The band at 957 cm⁻¹ may be attributed to silanol¹⁰⁷ and peak at 1636 cm⁻¹ is attributed to adsorbed water¹⁰⁸. The remaining significant sharp peaks at 1385 cm⁻¹ and 667 cm⁻¹ can most probably be attributed to Ca-oxalate (Spectral Database for Organic Compounds¹¹⁸, SDBS no. 12376). Ca-oxalate may be present in *E.hyemale* since it is ubiquitous in higher plant families and has been observed in most plant tissues and organs as an intracellular or extracellular deposit¹¹⁹. Ca-oxalate crystals are also commonly found to be precipitated in high concentration during the pulp bleaching with strong oxidising agents including hydrogen peroxide¹²⁰. Thus, Ca-oxalate is most likely formed during the treatment with hydrogen peroxide as by-product, adding to the amount of Ca-oxalate already present in the system. Since there was almost no Ca found on the knob tip based on EDX analysis and Raman microscopy, Ca-oxalate may be strongly distributed on the continuous epidermal layer. Despite the bands depicted in Fig. 2.17, there was a broad water peak centred at 3405 cm⁻¹ and a small doublet band at 2932 cm⁻¹ and 2860 cm⁻¹ due to C-H stretching⁹⁶

indicating the presence of very low amounts of organic materials after the acidic treatment of *E.hyemale* with hydrogen peroxide. In case of *E.hyemale* derived silica powder, neither water nor organics were observed.

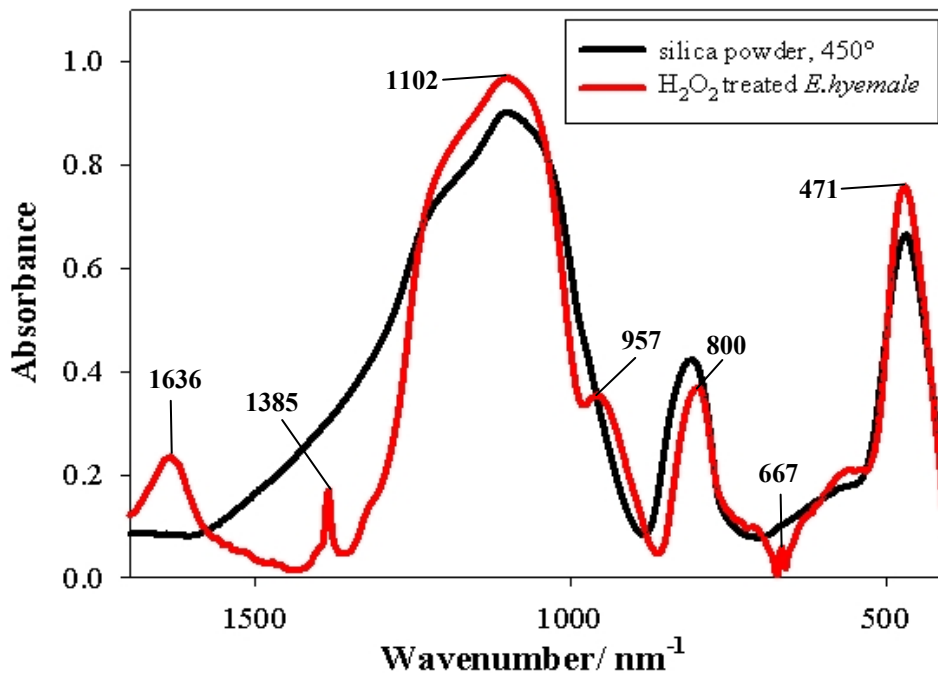


Figure 2.17 FTIR spectra of silica powder derived from *E.hyemale* treated by hydrogen peroxide (red curve) and HCl followed by calcination (black curve). The chemical treatment of *E.hyemale* with 30% H₂O₂ was performed within 18 months without light penetration. The HCl-treated *E.hyemale* was calcined at 450°C for 48 hours with a heating rate of 1 K/min.

WAXS/SAXS measurements were performed on the non-powdered sample as depicted in Fig. 2.18 to see whether there is any anisotropic scattering from oriented, non-spherical nanostructures. Some Bragg-spots from crystalline inclusions are clearly observed from the WAXS pattern (Fig. 2.18 (A)) with sharp peaks at about $q = 10.14 \text{ nm}^{-1}$ and 14.27 nm^{-1} , corresponding to the 001 and $\bar{2}10$ reflections from α -Ca-Oxalate (calcium oxalate monohydrate), respectively. The presence of Ca-oxalate crystals in the system detected by X-ray diffraction is in line with the FTIR analysis. The predominant amorphous silica is marked by the broad peak centred at $q = 15.5 \text{ nm}^{-1}$. The deposited Ca-oxalate crystals seem to be randomly distributed within the *E.hyemale* shoots by showing no preferred orientation with respect to the cell axis (Fig. 2.18 (A), (B)). The

spotty appearance of the reflections in the 2D patterns points to the presence of rather crystallites at least of several 10 μm .

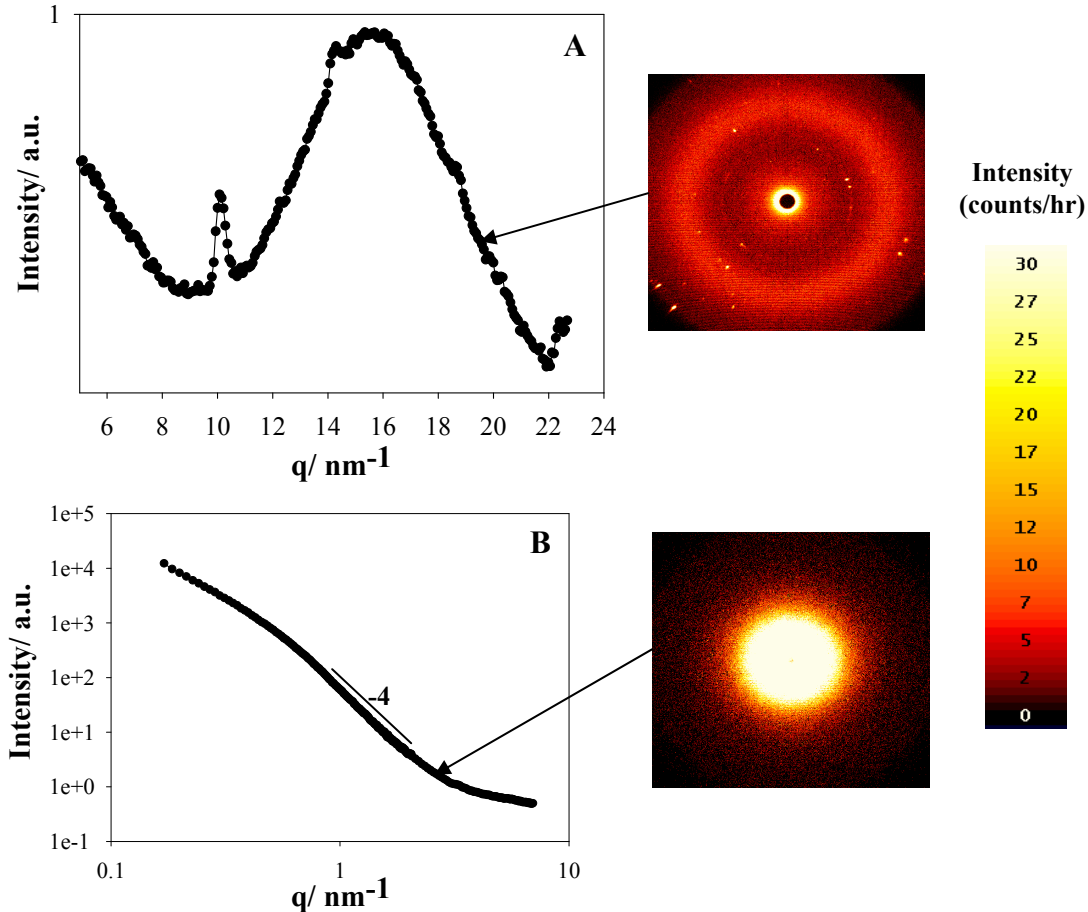


Figure 2.18 WAXS pattern (A) and SAXS pattern (B) of “silica” layer derived from *E.hyemale* treated with 30% H_2O_2 for 18 months without light penetration. The line in (B) indicate the power-law behaviour of the scattering intensity with $I \propto q^{-4}$ at large q .

The SAXS profile follows Porod’s law¹¹⁴ for $q > 1 \text{ nm}^{-1}$ (Fig. 2.18 (B)). The slope at low q is larger than 2, and the shape of the curve is somehow intermediate between the ash and the biogenic silica samples presented in the previous sub-section. The calculated T-parameter is about 4.4 nm, which is almost double than that of pure amorphous silica obtained from the calcination of HCl-treated *E.hyemale* at 400°C , but still lower than the one of the ash (Table 2.2). This suggests that the silica particles obtained after the treatment with H_2O_2 are considerably larger due to the influence of the inclusions of Ca-oxalate crystals, which have larger crystal sizes.

The nitrogen sorption isotherm of H₂O₂-treated *E.hyemale* sample (Fig. 2.19 (A)) showed a hysteresis loop, though rather narrow indicating the characteristic of mesoporous silica network. The specific surface area obtained was quite high, i.e. about 245 m²/g. The pore size distribution is rather broad compared to that of the biogenic silica described in the previous sub-section with a considerable larger average pore size of about 15 nm (Fig. 2.19 (B) vs. Fig. 2.15 (B)). The summary of nanostructural parameters of H₂O₂-treated *E.hyemale* sample based on SAXS and nitrogen sorption analysis is presented in Table 2.3. The SAXS surface is only slightly larger than the BET surface, which means that the sample exhibited significant open porosity after the hydrogen peroxide treatment.

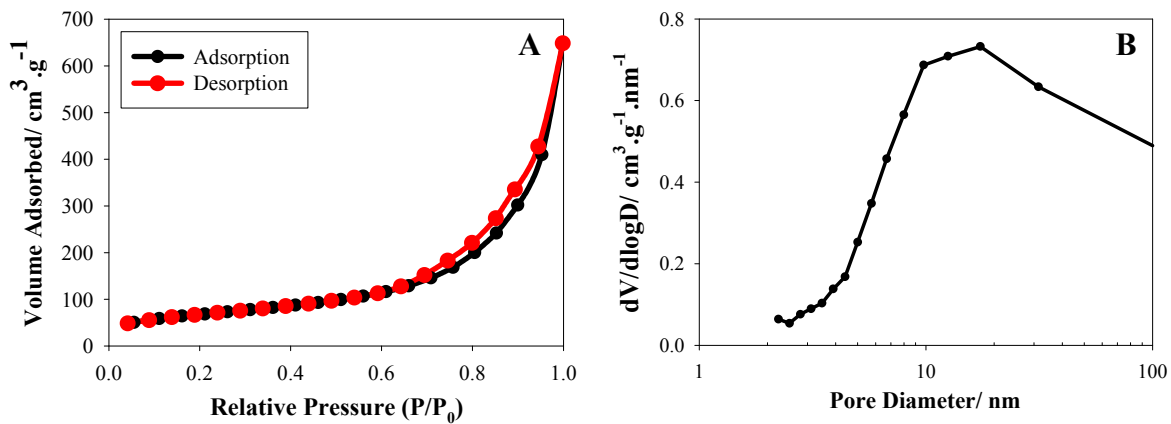


Figure 2.19 Nitrogen sorption isotherms of H₂O₂-treated *E.hyemale* (A) and pore size distribution from BJH analysis of the sorption data from the adsorption branch (B). *E.hyemale* stems were treated by 30% H₂O₂ for 18 months without light penetration.

Table 2.3 Nanostructural parameters of H₂O₂-treated *E.hyemale* based on SAXS and nitrogen sorption analysis.

Parameters	H ₂ O ₂ -treated <i>E.hyemale</i>
T-parameter (nm)	4.4
Porod constant, P	55.55
Integrated Intensity	181.02
BET surface area, σ_{BET} (m ² /g)	242.3
Total pore volume, V_p (cm ³ /g)	0.997
Porosity, ϕ	0.68
Average pore size, D_p (nm)	16.46
SAXS surface area, σ_{SAXS} (m ² /g)	289.95
Pore chord length, l_p (nm)	13.76
Wall chord length, l_w (nm)	6.57
Pore thickness, a_p (nm)	6.88
Wall thickness, a_w (nm)	3.28
$\sigma_{\text{SAXS}}/\sigma_{\text{BET}}$	1.2

P is the Porod constant (see Eq. A.26); (\tilde{I}) is the integrated intensity (see Eq. A.27); T is the mean chord length defined as $T = (4/\pi) (\tilde{I} / P)$ (see Eq. A.28); ϕ is the porosity calculated from the specific pore volume by $(V_p) / (V_p + 1/\rho)$ with ρ being the true density. ρ H₂O₂-treated *E.hyemale* sample is assumed to be 2.1 g/cm³, which is the density of *E.hyemale* derived silica powder obtained from the pycnometer measurement (Appendix B). σ_{SAXS} is calculated by $4\phi (1-\phi) / (T \cdot \rho_{\text{bulk}})$ (see Eq. A.28); l_p and l_w are mean chord lengths of pore and wall, respectively by applying the equation $1/T = 1/l_p + 1/l_w = 1/(\phi \cdot l_w) = 1/((1-\phi) \cdot l_p)$; whereas a_p and a_w are the mean thickness of pores and wall, respectively, calculated by using the equation $1/T = 1/2 \cdot (\phi \cdot a_w) = 1/(2(1-\phi) \cdot a_p)$ when slit/ plate morphology are taken into account (see Eq. A.29).

2.6 Discussion

Macroscopic silicification pattern and essentiality of silica for growth

Within mature *E.hyemale* stalks, silica content decreases basipetally from about 15% to 10% without any significant differences between internodes and nodes. This acropetal silicification pattern in *E.hyemale* suggests the requirement of Si as an essential nutrient for the normal growth, considering that the younger tissue requires more nutrient supplies compared to the older tissue as the maturity goes basipetally⁹². In addition, this silicification pattern towards the uppermost part of the stems of *E.hyemale* could also be facilitated by the higher transpiration rate on the distal region. The apical region undergoes more intensive transpiration because the radiation incident on them would be higher, thus water is lost in a greater quantities¹²¹, leaving the silica depositions in larger quantities within the upper part compared to the lower internodes. The role of Si as an indispensable element for *E.hyemale* is also supported by the presence of a relatively high silica content (about 11%) within the cone. This may corroborate the essential requirement of silica to keep the spores viable and to maintain its life activity against some abiotic stresses²³. However, the mechanism on how Si is involved in the metabolism during the growth of *E.hyemale* is still very elusive and need further investigation.

Local distribution of silica in *E.hyemale* internodes

Local distribution of silica within the *E.hyemale* internodes is on the entire epidermal layer with the highest concentration on the knob tips, followed by the area between the knobs, and finally the rest of the continuous epidermal layer according to micro-CT, SEM/ backscattered electron, SEM/EDX map of Si, Raman microscopy, and FTIR investigations. This continuous silicification pattern as a particularity of *E.hyemale* was already recognized by Kaufman *et al.*²⁷. This is quite in contrast to other plants (e.g. *Poaceae/ Gramineae*) where silica is mostly deposited in the cell walls and cell lumina as silica bodies or phytoliths²¹. Kaufmann *et al.*²⁷ also claimed that this uniform silicification pattern in *E.hyemale* is unique within the *Equisetum* family, and does not apply for instance to *E.arvense*, where they found silica primarily in discrete knobs and rosettes on the epidermal surface. More recent SEM investigations coupled

with EDX mapping of Si demonstrated however a thin continuous silica layer on the outer epidermis also in *E.arvense*²⁶. Moreover, the accumulation of silica in the knob tips appears to be more conspicuous in the developing shoots in contrast to the mature shoots where silica seems to be more predominantly deposited on the continuous epidermal layer (Fig. 2.6 (E)). This result is contrary to the investigation of Kaufman *et al.*²⁴, claiming that the deposition of SiO₂ in long epidermal cell walls of *E.hyemale* occurs after internodal extension has ceased and should be therefore considered as one of the final stages in internodal differentiation that involves strengthening the cellulosic framework of the cell wall. He found out that the silicification of the knobs of the ribbed portions occurred when the internodes reached maturity and silica was first detected in the stomatal apparatus beginning with internode 3 from the apex, then the epidermal papillae (internode 8), and finally the in radial cell walls of the long epidermal cells (internode 10). Probably, this was because he investigated only very local areas using SEM/EDX. Thus, he could not represent the general silicification pattern of the whole *E.hyemale* shoot due to the sample heterogeneity and variations of silica patterns present within the local regions.

Forms of silica deposited in *E.hyemale*

Raman microscopy and FTIR investigation revealed two different silica modifications in *E.hyemale*. The first type which is restricted exclusively to the knob tips is pure hydrated amorphous silica with almost no interaction with polysaccharides. The second type, which is deposited in the continuous layer adjacent to the epidermal cells, lacks silanol groups and is closely associated with the cell wall biopolymers such as pectin, hemicellulose and cellulose in addition to the Ca, K, Na, Mg containing inorganic compounds based on the SEM/EDX analysis. The pure hydrated amorphous silica deposited particularly in the knob tips of *E.hyemale* is similar to those deposited in the tip of macrohairs of grass *Phalaris canariensis* L¹²² which most probably has a colloidal silica network with Si-OH groups at the particle surfaces¹⁰ without being associated with other elements in contrast to the silica bodies deposited in other plants, which are generally interfered by the presence of other elements, such as Al, K, Ca, P, and S¹²³. In contrast to first silica type, the second type is anhydrous. The lack of silanol groups may be influenced by the presence of biopolymers and inorganics which

act as catalysts accelerating the condensation process of water contained in the silanol groups. Cell wall biopolymers may also act as a polymeric template that regulates the silica deposition process and controls the shape and size of the colloidal silica particles similar to many other biominerals and mineralised tissues. However, it is still unclear whether there are some direct connections between silica with organic or inorganic substances. The presence of organic silicon compounds (Si-C- or Si-O-C-) is possible based on Raman/FTIR studies but they remain ambiguous since the spectra are mostly overlapped with those of polysaccharides. Some papers report that there is no experimental evidence of organosilicon complexes (Si-O-C- organic bonds) ^{124, 125, 126} nor organic binding via Si-C- ¹²⁵ in plant or animal tissue under physiological condition. There is also no organo-silicon complexes found in *E.hyemale* sap ¹²⁷. Thus, it may be speculated that siloxane bonds (-Si-O-Si-) are prevailing over the surface silica particle (Fig. 2.20) and silica may have strong association with the polysaccharides (cellulose, hemicellulose, and/or pectin) for instance via hydrogen bonding between oxygen atoms in silica network with the hydroxyl groups from polysaccharides.

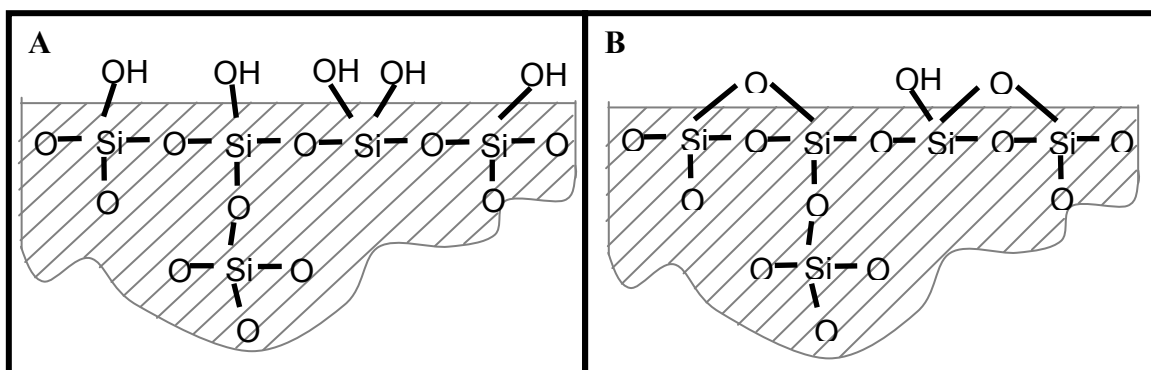


Figure. 2.20 Illustration of two silica forms present in native *E.hyemale*. (A) silica in knob tips. (B) silica in continuous layer adjacent to epidermal cells. The hydrated silica in (A) is referred to as silica type 1, whereas the anhydrous type in (B) is referred to as silica type 2.

Nevertheless, it is not impossible that particular organic silicon compounds may exist in *E.hyemale*. Schwarz ¹²⁸ found a bound form of Si in polyuronides in 456 ppm in horsetail kelp. A detailed study of *E.hyemale* mapping using confocal Raman microscopy ¹²⁹ has revealed a large amount of pectin and relatively high hemicellulose content in the epidermal cells below the grooves and perhaps silica has some linkages with pectin/hemicellulose which has definitely different chemical structure than silica

deposited on the knob tips. Freitas *et al.*¹³⁰ also found two distinct forms of silica in rice husk based on NMR study, namely amorphous hydrated silica and organically bound silicon species. All of these facts may trigger a more detailed study to reveal all possible silica forms found in the nature and particularly in *E.hyemale* either in the form of organically or inorganically (cations) bonded silicon compounds.

Crystallinity and nanostructure of silica deposited in *E.hyemale*

Crystalline silica in the form of α -quartz was found above a stomatal opening of a mature *E.hyemale* internode and was detected by Raman even though silica was found to be mostly amorphous according to the X-ray diffraction analysis. It might be possible that amorphous silica is converted into quartz during the ageing since it is likely to be found in the senescent shoots of *E.hyemale*. However, quartz may also derive from the dust contamination which was trapped by the fluid exerted through the stomata and precipitated *in situ*. Such crystalline inclusions are not part of the *E.hyemale* appendages, and due to its rather low quantity (less than 7% based on analysis of the X-ray diffraction patterns), it is neglected.

Primary silica particles have a sheet-like structure with a thickness in the order of 2 nm based on SAXS analysis. SAXS also indicates a network of mesoporous silica structure with a relatively high surface area of about 375 m²/g (according to BET). The conditions during chemical and thermal treatments were relatively mild, thus it may not significantly alter the structure of silica accumulated in the native tissues of *E.hyemale*. It is of no doubt that some biomolecules, such as polysacharrides or proteins or inorganic substances play role in regulating size, shape, and crystallinity within the plant system¹⁰, besides the genetic control which may also be considerably involved.

Possible biological roles of silica in *E.hyemale*

Finally, some possible biological functions of silica in *E.hyemale* are speculated. Since silica is accumulated in the peripheral region, it is very likely to play a role in strengthening the cuticle, protecting the plant body, controlling the excessive water loss, and serving as a defence against contact-probing insects and fungi^{103, 131}. Hauke¹³² observed that *Equisetum* was avoided by insects and largely immune from fungus and other diseases perhaps due to the presence of the silica coating. Silica rich containing

plant such *E.hyemale* has been attracting some researchers in order to study the role of silica in the enhancement of the mechanical properties of this slender hollow stem plant¹⁸. No evidence for an essential tensile nor compressive reinforcement by silica was found after scrapping off part of the epidermis. There was no drastic change in the stress-strain behaviour, except a reduction of the initial Young's modulus by about 20%. However a continuous outer silica layer associated with the polysaccharides adjacent to the epidermis cell wall would at least be very beneficial for the enhancement of flexural rigidity of the stalk due to the high Young's modulus of silica¹³³ and silica may also act as mechanical reinforcement agents within the cell wall biocomposites. The hydrated amorphous silica accumulated in the knob tips would not much contribute to the improved overall mechanical properties of the stalks due their discrete distribution and without any interaction with the cell wall biopolymers. This would be then in line with the results of Speck *et al.*¹⁸ supposed they removed only the hydrated silica deposited on the knob tips. Final evidence for a definite mechanical function of silica in the internodal system of *Equisetum* needs however still to be proved by properly designed micromechanical tests.

2.7 Summary

Within this chapter, a comprehensive study of silica accumulations in *E.hyemale* was performed from macroscopic length scales down to the molecular level using several sophisticated analytical techniques.

The overall silica content within the *E.hyemale* tissue increased from about 6% to 14% during the growing period. The silica content within mature *E.hyemale* stalks decreased basipetally from about 15% to 10% without significant differences between internodes and nodes. Silica is mainly deposited on the continuous epidermal layer with the highest concentration on the knob tips. The knob, epidermal flank, and inner lower knob comprised of about 33%, 17%, and 6%-wt silicon, respectively whereas almost no silicon was found in the interior parts. A thin continuous silica layer with an intact structure was remaining after the treatment of *E.hyemale* stems with 30% hydrogen peroxide, showing clearly that knobs, stomatal apparatus including the guard cells and

subsidiary cells, wart-like protuberances on the furrows, and epidermal cell walls are highly silicified.

Silica is deposited mostly in amorphous form and two different silica modifications are found in *E.hyemale*. The first type is pure hydrated amorphous silica which is restricted to the knob tips with almost no interaction with polysaccharides. The second type is a non-hydrated amorphous silica which is deposited in the whole continuous layer adjacent to the epidermal cells. This type lacks silanol groups and is closely associated with the cell wall biopolymers such as pectin, hemicellulose and cellulose in addition to the inorganic compounds like Ca-oxalate. Silica primary particles have a sheet-like structure with a thickness of about 2 nm.

It is concluded that silica is not only an essential nutrient for the growth of *E.hyemale*, but it may also strengthen the cuticle, and protect the plant body, in preventing the excessive water loss and as a barrier against insects / fungi. Since silica is deposited on the continuous outer layer adjacent to the epidermis cell walls, it is likely to enhance the overall flexural rigidity of the *E.hyemale* stalks.

Chapter 3

Isolation of Silica from *Equisetum hyemale*

This chapter describes the results from the attempt to isolate pure biogenic amorphous silica from *E.hyemale*. Biogenic silica from plant sources has a great potential as sustainable, low cost bio-resource for value-added new materials production. Examples include for instance reactive silica, filler, chromatographic supports, absorbent, and catalyst base ⁷. Based on the results from the previous chapter, silica in *E.hyemale* is present predominantly in close association with organic and other inorganic components. Thus, chemical and thermal treatments were applied to remove the inorganic impurities and the organic matrix in the raw materials and to obtain the remaining residue of pure biogenic amorphous silica. Two sets of samples were prepared:

- i) Native, dry *E.hyemale* was calcined in air at seven different temperatures (300°C, 350°C, 400°C, 450°C, 500°C, 600°C, 750°C) and a low heating rate of 1 K/min for 48 hours. This treatment delivers the biogenic ash, which might for instance be an interesting material as filler in polymer industries or for concrete or cement production due to its high silica content ^{38, 49}. Based on the present investigation, *E.hyemale* contains a very high amount of minerals, and its ash content can be up 20% of the total weight of the dry plant, where around 60% thereof is silica.
- ii) A chemical treatment using 10% HCl was performed to largely remove all inorganic compounds except silica, prior to the calcination in air at the same temperatures and conditions as applied for the ash production. This treatment intended to produce high grade, pure biogenic amorphous silica from *E.hyemale*.

The nanostructures of the obtained ashes and biogenic silica samples were then characterised by means of powder diffraction (WAXS), SAXS, and nitrogen sorption to obtain detailed information about crystallinity, primary particle size, surface area, and pore size distribution. The effects of chemical and thermal treatments on the quality of the resulting materials were analysed in order to optimise the process for further

potential development into the pilot and industrial scales for the mass production of high value materials based on low cost and abundant raw materials.

3.1 Native and HCl-treated *E.hyemale*

All of the samples used in this study were harvested in November 2002 and were stored for about 4.5 years in contrast to the fresh samples investigated in Chapter 2. Also, the native *E.hyemale* samples were powdered before being subjected to the subsequent chemical and thermal treatments. Thus some structural features may differ from those found in the previous section due to the different history.

XRF measurement for elemental analysis proved that the acidic treatment of *E.hyemale* using 10% HCl was powerful enough to significantly reduce the total amount of alkali and alkaline-earth metals from about 3% in the native tissue down to less than 0.2% (Table 3.1). The HCl-treated samples were therefore almost free of the inorganic compounds that were intermixed with the silica in the native plant mainly in the continuous epidermal layer, based on the results from the previous chapter.

Table 3.1 Elemental analysis of *E.hyemale* after chemical treatment with 10% HCl at boiling temperature for 2 hours for inorganics removal by using XRF.

Elements	Native <i>E.hyemale</i> (%-dry weight)	After HCl Treatment (%-dry weight)
Na	0.24	0.10
K	1.3	0.02
Mg	0.09	< 0.0097
Ca	1.1	0.005
Al	< 0.003	< 0.003
Fe	0.026	0.002
P	0.13	< 0.0006
S	0.11	0.03
Cl	0.25	0.02

Fig. 3.1 shows WAXS and SAXS patterns from the native and HCl-treated samples of *E.hyemale*, which were used as the starting materials for the thermal treatments to produce ash and biogenic silica, respectively. Nitrogen sorption was also performed on these samples to determine the surface area, pore size distribution, and porosity. Similar to the previous chapter, no adsorption data could be obtained from

native *E.hyemale*, indicating the inaccessibility of the pores for nitrogen gas due to the very close association between organic and inorganic compounds and perhaps the pores are fully occupied by mainly organic substances. After the HCl treatment, the samples became accessible to the nitrogen gas and a surface area of about $60 \text{ m}^2/\text{g}$ was obtained. The nitrogen isotherm and the pore size distribution of HCl-treated *E.hyemale* are depicted in Fig. 3.2.

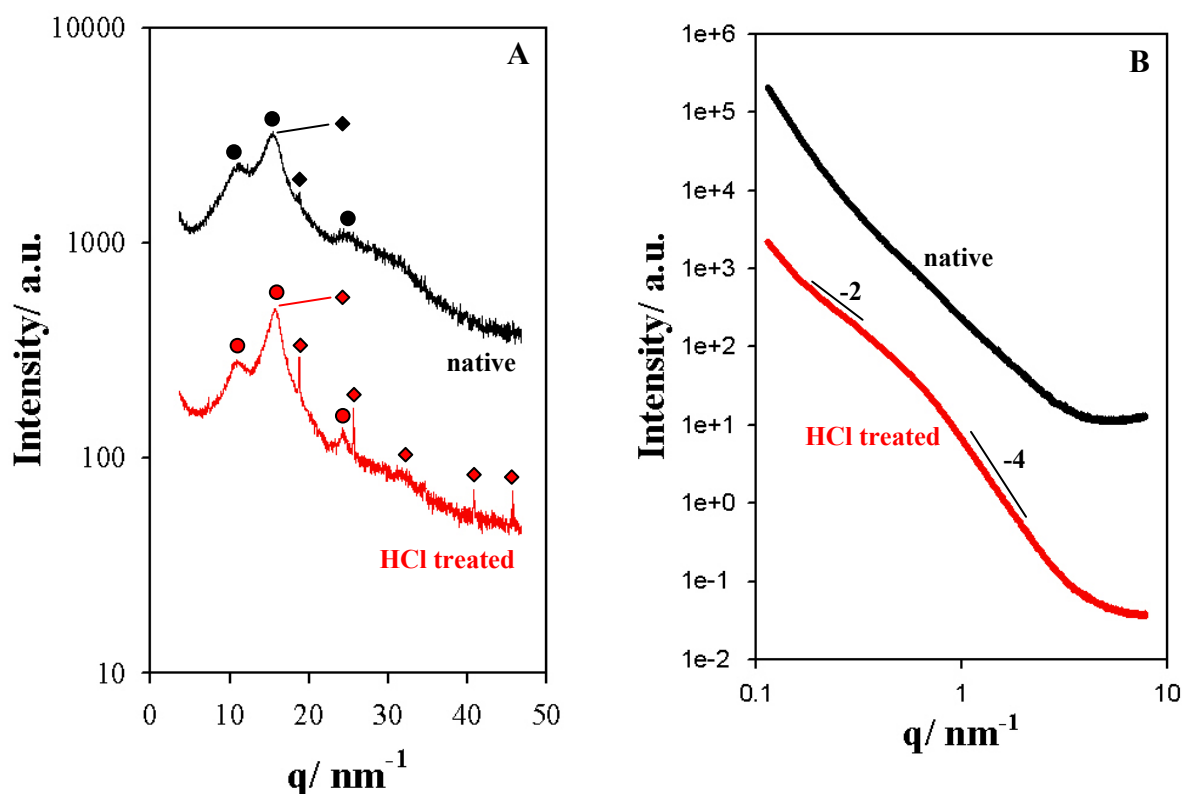


Figure 3.1 Powder diffractograms (A) and SAXS patterns (B) from powdered specimens of the native and HCl-treated *E.hyemale*. ● and ◆ in powder diffraction patterns denote cellulose and quartz, respectively. The lines in (B) indicate the power-law behaviour of the scattering intensity with $I \propto q^{-4}$ (Porod's law) at large q and a q^{-2} behaviour at low q for the HCl treated sample.

The diffraction patterns of the native and HCl-treated *E.hyemale* show substantial similarities (Fig. 3.1 (A)). Some minor reflections from crystalline silica polymorph such as α -quartz with the main peak at $q = 18.9 \text{ nm}^{-1}$ was better visible after the removal of inorganic substances and cell wall matrix, namely pectin and hemicellulose as the consequence of acidic treatment with HCl. Reflections from crystalline cellulose are visible in both samples, i.e. the $101/10\bar{1}$ doublet at $q \approx 11 \text{ nm}^{-1}$, the 002 reflection at $q = 16.2 \text{ nm}^{-1}$ (which was overlapped with the broad peak of

amorphous silica at $q = 15.5 \text{ nm}^{-1}$), and the 040 reflection at $q = 24.3 \text{ nm}^{-1}$ ¹¹¹. Calcium oxalate which was supposed to be present in the native *E.hyemale* as suggested by Raman microscopy and FTIR was not clearly observed in the diffraction pattern. Probably, its main peak at $q = 10.7 \text{ nm}^{-1}$ was masked by the broad $101/10\bar{1}$ cellulose peaks.

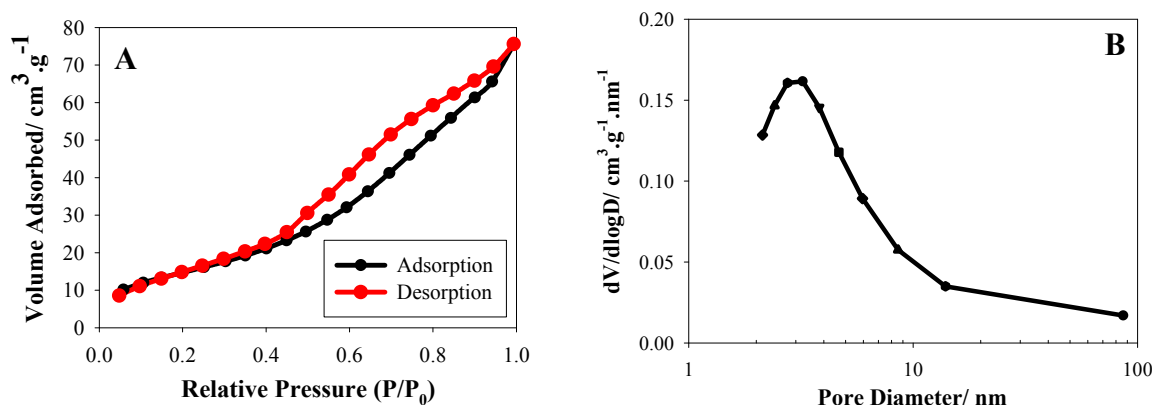


Figure 3.2 Nitrogen sorption isotherms of HCl-treated *E.hyemale* (A) and pore size distribution from BJH analysis of the sorption data from the adsorption branch (B). *E.hyemale* stems were treated by 10% HCl at boiling temperature for 2 hours.

The SAXS signal (Fig. 3.1 (B)) from the HCl-treated specimen which looks quite different than that of untreated sample is believed to be primarily derived from the scattering of a highly porous silica framework due to a change of the respective contrast contribution. Replacing the scattering contrast $\Delta\rho^2 = (\rho_{\text{SiO}_2} - \rho_{\text{M}})^2$ between silica and organic matrix as in the case of native sample by $\Delta\rho^2 = (\rho_{\text{SiO}_2})^2$ between silica and pores as in the case of HCl-treated sample would indeed lead to an increase of the scattering contrast by more than an order of magnitude (the electron densities were estimated to be $\rho_{\text{M}} \approx 5.0 \cdot 10^{23} \text{ e}^-/\text{cm}^3$ and $\rho_{\text{SiO}_2} \approx 6.6 \cdot 10^{23} \text{ e}^-/\text{cm}^3$). Furthermore, the region at low q is proportional to a power law with a slope of -2, which is an indication of the presence of plate-like structures (see also previous chapter, Fig. 2.14), which appeared only after the HCl treatment. This result is again supported by the BET isotherm (Fig. 3.2 (A)) showing a type H3 hysteresis loop. This indicates a mesoporous structure with slit-shape pores or plate-like particles¹¹⁶ that become "visible" after the removal of the inorganic compounds and organic matter other than cellulose (e.g. pectin and hemicellulose). The summary of nanostructural parameters of native and HCl-

treated *E.hyemale* obtained from the combination of SAXS and nitrogen sorption analysis and can be seen in Table 3.2.

The differences in nanostructural parameters between native and HCl-treated *E.hyemale* are obviously seen in Table 3.2. The inaccessibility of nitrogen in native *E.hyemale* powder indicates an extremely close association among all of organic and inorganic compounds present. After the HCl treatment, the porosity of more than 15% was created, leading to a surface area of about 60 m²/g according to the BET analysis. This is due to the removal of inorganic substances besides also the dissolution of cell wall matrix polymers namely pectin and hemicellulose which are easily hydrolysed by acid in contrast to cellulose. Interestingly, the surface area determined by SAXS is larger by a factor of 2 as compared to the BET value. Since BET only measures the open porosity and SAXS is sensitive to both, open and closed pores, it is concluded that the area occupied by closed pores is comparable with the area occupied by the open pores. The other parameters derived from SAXS analysis listed in Table 3.2 are to be interpreted with caution since many cell wall polymer phases are still present and influence the SAXS signal.

Table 3.2 Nanostructural parameters of native and HCl-treated *E.hyemale* based on SAXS and nitrogen sorption analysis.

Parameters	Native <i>E.hyemale</i>	HCl-treated <i>E.hyemale</i>
T-Parameter (nm)	1.56	3.04
Porod constant, P	53.60	170.68
Integrated intensity	65.50	407.99
BET surface area, σ_{BET} (m ² /g)	-	56.38
Total pore volume, V_p (cm ³ /g)	-	0.117
Porosity, ϕ	-	0.17
Average pore size, D_p (nm)	-	8.30
SAXS surface area, σ_{SAXS} (m ² /g)	-	128.31
Pore chord length, l_p (nm)	-	3.65
Wall chord length, l_w (nm)	-	18.34
Pore thickness, a_p (nm)	-	1.82
Wall thickness, a_w (nm)	-	9.17
$\sigma_{\text{SAXS}}/\sigma_{\text{BET}}$	-	2.28

E.hyemale derived silica $\rho = 2.1 \text{ g/cm}^3$ obtained from the pycnometer measurements (Appendix B) and cellulose $\rho = 1.5 \text{ g/cm}^3$ ¹³⁴. Here it is considered that the HCl-treated sample is composed of 30% silica and 70% cellulose under the assumption that native *E.hyemale* consisted of 80% organics and 20% minerals and 60% silica thereof and during the HCl treatment, there was a mass loss of organics (pectin and hemicellulose) of about 65% and total removal of inorganics except silica.

3.2 Ash and biogenic silica from *E.hyemale*

Calcination in air was done for both, native and HCl-treated samples at 7 different temperatures (300°C, 350°C, 400°C, 450°C, 500°C, 600°C, 750°C) with a very slow heating rate of 1 K/min, and were then held for 48 hours. The WAXS and SAXS patterns of the ashes (calcined native *E.hyemale*) and biogenic silica (calcined HCl-treated *E.hyemale*) for the different temperatures are depicted in Fig. 3.3 and Fig. 3.4, respectively.

The diffraction patterns of the ashes are very similar, except for the sample treated at 750° (A7) as can be seen in Fig. 3.3 (A). The ashes of *E.hyemale* (A1-A6) contained amorphous silica marked by the broad peak at around $q = 15.5 \text{ nm}^{-1}$ and in addition several crystalline mineral phases. Reflections from crystalline silica in the form of α -quartz are predominantly seen at $q = 18.9 \text{ nm}^{-1}$ and $q = 14.8 \text{ nm}^{-1}$. The conspicuous peak at $q = 20 \text{ nm}^{-1}$ can be attributed to KCl, together with 2 further peaks at $q = 28.3 \text{ nm}^{-1}$ and $q = 34.6 \text{ nm}^{-1}$. Another obvious peak at $q = 20.8 \text{ nm}^{-1}$ together with other reflections indicated in Fig. 3.3 (A) by a filled square can unambiguously be attributed to calcite (CaCO_3). Sample A7 was calcined at 750°C and shows a clear transformation of the amorphous silica into α -cristobalite marked by the pronounced peaks at $q = 15.7 \text{ nm}^{-1}$ and $q = 25.7 \text{ nm}^{-1}$, while the presence of a trace amount of quartz is still noted.

In the calcined HCl-treated samples (Fig. 3.3 (B)), α -quartz reflections were observed for all temperatures together with the broad peak from amorphous silica. Quartz is the only crystalline component detected in these samples, and comparing qualitatively the height of the peaks, the amount is similar in the two types of samples. The concentration of α -quartz can roughly be estimated by the integral intensity ratio of Bragg-peaks from α -quartz and total integrated intensity from amorphous and crystalline silica (see Appendix C). This yields an amount of α -quartz of less than 7%, i.e., the major phase is amorphous silica. In contrast to the ash (A7, Fig. 3.3 (A)) which showed a structural transformation of amorphous silica into α -cristobalite at the highest heat treatment temperature, the corresponding calcined HCl-treated sample (B7, Fig. 3.3 (B)) did not show the phase transformation at 750°C. The phase transition temperature from amorphous silica into α -cristobalite within standard conditions is reported between

1200°-1400°C³². Thus, the presence of inorganic impurities in the ash samples seems to account for the much early transformation since they could act as catalysts accelerating the transformation between these two silica polymorphs.

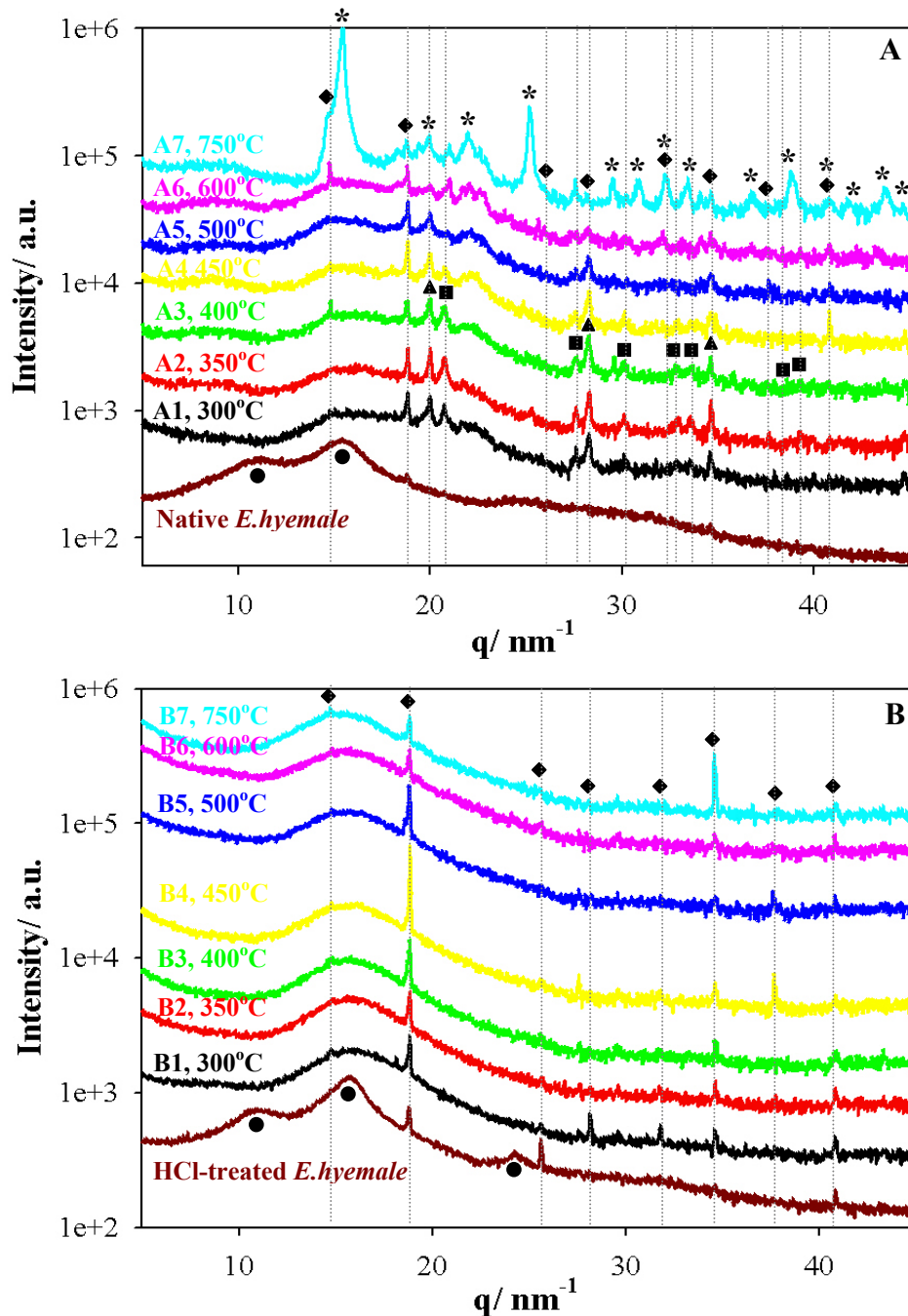


Figure 3.3 X-ray powder diffractograms of ashes (A) and biogenic silica (B), derived from calcination of the native and the HCl-treated samples, respectively. ■, *, ▲, ●, and ◆ in the powder diffraction patterns denote calcite, cristobalite, KCl, cellulose, and quartz, respectively.

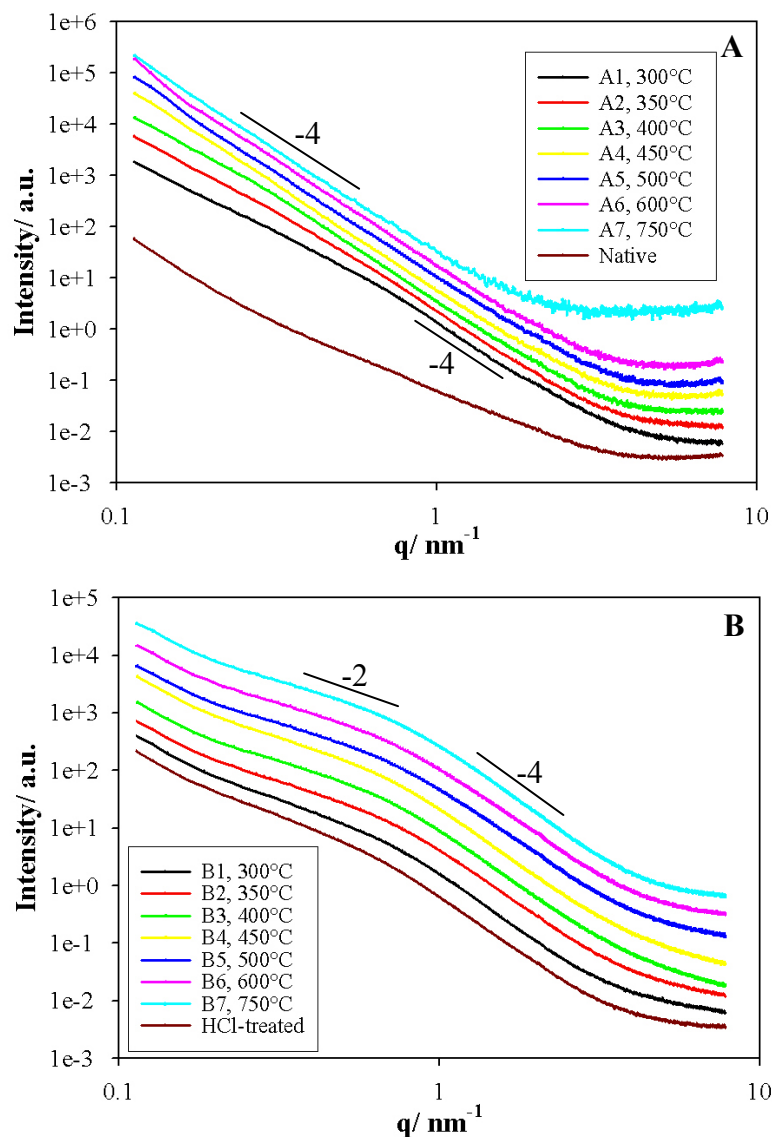


Figure 3.4 SAXS patterns of ash (A) and silica-ash (B). The lines indicate the power-law behaviour of the scattering intensity with $I \propto q^{-4}$ at large q for the ash and silica ash samples (Porod's law), and a q^{-2} behaviour at low q for the silica ash samples.

From the SAXS patterns (Fig. 3.4), quite clear differences are observed between the profiles of ash and calcined HCl-treated samples, but the differences were less pronounced within the same sample type treated at different temperatures. For the ash treated at low temperatures ($< 400^\circ\text{C}$), a shoulder is recognised at $q \approx 1 \text{ nm}^{-1}$ with a q^{-4} slope at larger q and a somewhat lower slope ($\approx q^{-3}$) at smaller q . With increasing temperature, this behaviour changes to a q^{-4} slope over the whole measured range (pure Porod scattering). This means that there is no specific length scale of porosity in these specimens lower than about 50 nm. In the case of the calcined HCl-treated samples, Porod's law was obviously fulfilled in large q region ($q > 1 \text{ nm}^{-1}$), while at low q , the

intensities were proportional to q^{-2} for all specimens with only very little change with temperature. This indicates the scattering from sharp interfaces with a typical correlation length below 10 nm. At very low q , the intensity always increased strongly, suggesting the presence of large structures, such as cracks or large voids. The calculated T-parameters and other nanostructural parameters obtained from the SAXS analysis are listed in Table 3.3 (A) and Table 3.3 (B) for the ash (A1-A7) and the calcined HCl-treated (B1-B7) samples, respectively. The nanostructural data for the native and HCl-treated sample are also displayed to make the comparison easier. It should be noted that due to the shape of the SAXS curves for the ash (increase of intensity towards low q with a negative power law exponent > 2), only a lower boundary for the integrated intensity is given. This means, that the T-parameters given in Table 3.3 (A) are lower estimates.

The SAXS data were complemented by nitrogen sorption analysis. The corresponding sorption isotherms as well as the pore size distributions determined by a BJH analysis¹¹⁷ are presented in Fig. 3.5. Hysteresis loops are clearly seen for all samples at all temperatures, suggesting the typical characteristics of mesoporous systems. The hysteresis loops type H3 in the calcined HCl-treated samples were more pronounced than those of the ash samples, suggesting slit-shaped mesopores or plate-like particles¹¹⁶.

For the ash samples, there is a decrease of the adsorbed amount and a shift of the hysteresis loop to higher relative pressures with increasing temperature. This suggests a decrease of the total surface area as well as an increase of the average pore size (D_p) with temperature, which is confirmed by the numerical values extracted from the nitrogen sorption analysis in Table 3.3 (A). A peculiar behaviour is observed at the isotherm at 600°C which shows a slight transition at low relative pressure of about 0.2 (Fig. 3.5 (A)). This may be related to some additional microporosity in this sample which is observed at about 2 nm in the pore size distribution (Fig. 3.5 (C)), even though the large pores are clearly shifted to the right as compared to the lower temperatures. This peculiarity might be associated with the phase transition of amorphous silica into cristobalite which seems to start already at 600°C as supported by XRD (Fig. 3.3). However, this effect should not be overinterpreted. It could also be due to an experimental artefact since the BJH model does not generally perfectly fit in the

micropore regions and there is no clear evidence of such microporosity from SAXS (Fig. 3.4 (A)). At 750°C (A7), there was almost no sorption of nitrogen anymore by the ash sample, suggesting that the phase transformation of amorphous silica into cristobalite has led to a full collapse of the pore structure in this sample. The pore size distribution of ash samples is very broad and does not show any clear maximum. The average pore sizes tended to increase with increasing temperatures (Fig. 3.5 (C)).

In contrast to the ash samples, the calcined HCl-treated samples showed much higher pore volumes and in particular much higher surface areas (Fig. 3.5 (B), Table 3.3 (B)). The adsorbed amount first increased with temperature until 500°C and then decreased again. The pore size distributions of these samples are quite narrow and look very similar for all temperatures with an average pore size of about 7 nm (Fig. 3.5 (D)).

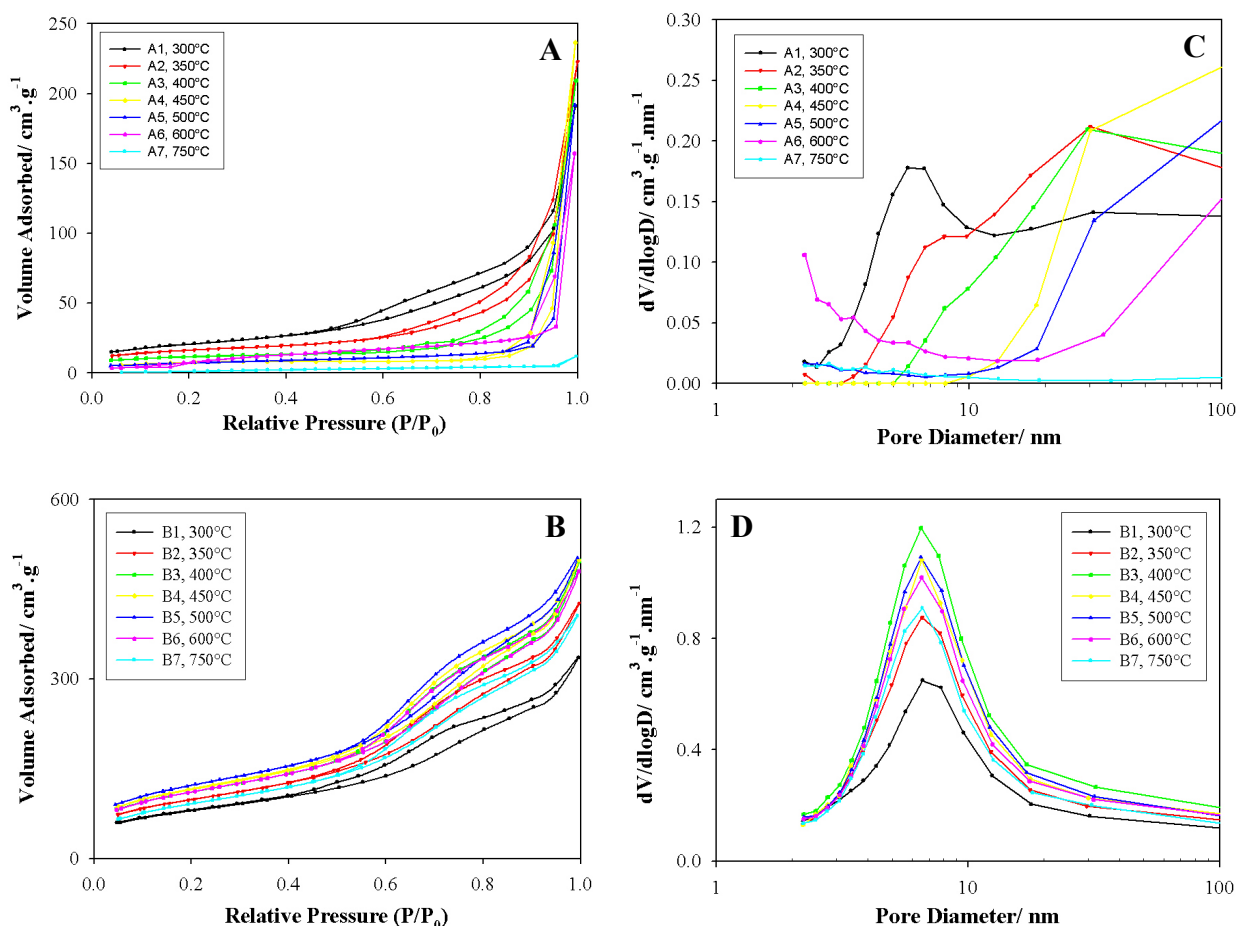


Figure 3.5 Nitrogen sorption isotherms and pore size distributions of ashes and calcined HCl-treated samples prepared at different temperatures during calcination. (A) and (B) show the nitrogen sorption isotherms of various ashes and biogenic silica respectively, whereas (C) and (D) show the corresponding pore size distributions from BJH analysis of the adsorption branches, respectively.

The summary of the nanostructural parameters of the ashes (A1-A7) and the calcined HCl-treated samples (B1-B7) obtained from SAXS and nitrogen sorption investigations are presented in Table 3.3. Additionally, this nanostructural information is also represented in several graphs depicted in Fig. 3.6 and Fig. 3.7 for a clearer data presentation and to ease data interpretation.

Table 3.3 (A) Nanostructural parameters of ash samples from *E.hyemale* based on SAXS and nitrogen sorption analysis.

Parameters	Native <i>E.hyemale</i>	A1 (300°C)	A2 (350°C)	A3 (400°C)	A4 (450°C)	A5 (500°C)	A6 (600°C)	A7 (750°C)
Color	Dark yellow	dark grey	grey	grey	grey	grey	grey	pink whitish
T (nm)	1.52	4.08	5.34	5.91	5.71	5.39	6.07	31.94
P	53.60	78.01	50.16	38.08	29.56	31.46	17.60	0.29
Integrated Intensity	65.50	250.31	210.64	176.82	132.61	133.23	83.99	7.37
σ_{BET} (m ² /g)	-	74.04	58.01	40.97	27.23	25.50	16.51	9.21
V_p (cm ³ /g)	-	0.293	0.342	0.322	0.364	0.295	0.242	0.018
ϕ	-	0.41	0.45	0.44	0.47	0.41	0.37	0.04
D_p (nm)	-	15.85	23.59	31.42	53.43	46.21	58.55	7.87
σ_{SAXS} (m ² /g)	-	168.64	140.61	122.92	136.06	128.06	100.74	2.18
l_p (nm)	-	6.96	9.73	10.48	10.70	9.20	9.59	33.25
l_w (nm)	-	9.88	11.85	13.56	12.25	13.02	16.54	808.48
a_p (nm)	-	3.48	4.87	5.24	5.35	4.60	4.80	16.63
a_w (nm)	-	4.94	5.93	6.78	6.12	6.51	8.27	404.24
$\sigma_{\text{SAXS}}/\sigma_{\text{BET}}$	-	2.28	2.42	3.00	5.00	5.02	6.10	0.24

Table 3.3 (B) Nanostructural parameters of calcined HCl-treated samples from *E.hyemale* based on SAXS and nitrogen sorption analysis.

Parameters	HCl- treated <i>E.hyemale</i>	B1 (300°C)	B2 (350°C)	B3 (400°C)	B4 (450°C)	B5 (500°C)	B6 (600°C)	B7 (750°C)
Color	dark brown	dark brown	brown	light brown	dull white	white	white	white
T (nm)	3.04	2.84	2.48	2.53	2.64	2.33	2.38	2.58
P	170.68	304.06	417.30	406.84	368.83	470.68	455.51	403.64
Integrated Intensity	407.99	679.53	814.67	810.23	765.48	859.99	852.56	817.18
σ_{BET} (m ² /g)	56.38	285.50	350.80	395.80	408.40	435.10	398.00	332.30
V_p (cm ³ /g)	0.117	0.515	0.656	0.764	0.766	0.773	0.738	0.624
ϕ	0.17	0.52	0.58	0.62	0.62	0.62	0.61	0.57
D_p (nm)	4.15	7.22	7.48	7.72	7.50	7.11	7.42	7.51
σ_{SAXS} (m ² /g)	128.31	348.07	444.03	463.01	444.65	506.83	486.06	419.22
l_p (nm)	3.65	5.92	5.90	6.60	6.89	6.10	6.07	5.95
l_w (nm)	18.34	5.47	4.29	4.11	4.28	3.76	3.92	4.54
a_p (nm)	1.82	2.96	2.95	3.30	3.44	3.05	3.04	2.98
a_w (nm)	9.17	2.74	2.14	2.06	2.14	1.88	1.96	2.27
$\sigma_{\text{SAXS}}/\sigma_{\text{BET}}$	2.28	1.22	1.27	1.17	1.09	1.16	1.22	1.26

The true densities of biogenic silica (calcined HCl-treated) and ash samples are 2.1 g/cm³ and 2.4 g/cm³, respectively which were obtained from the pycnometer measurements based on the samples treated at 600°C (Appendix B) and were assumed to be constant over the whole temperature range; ρ α -cristobalite = 2.21 g/cm³ ²⁹.

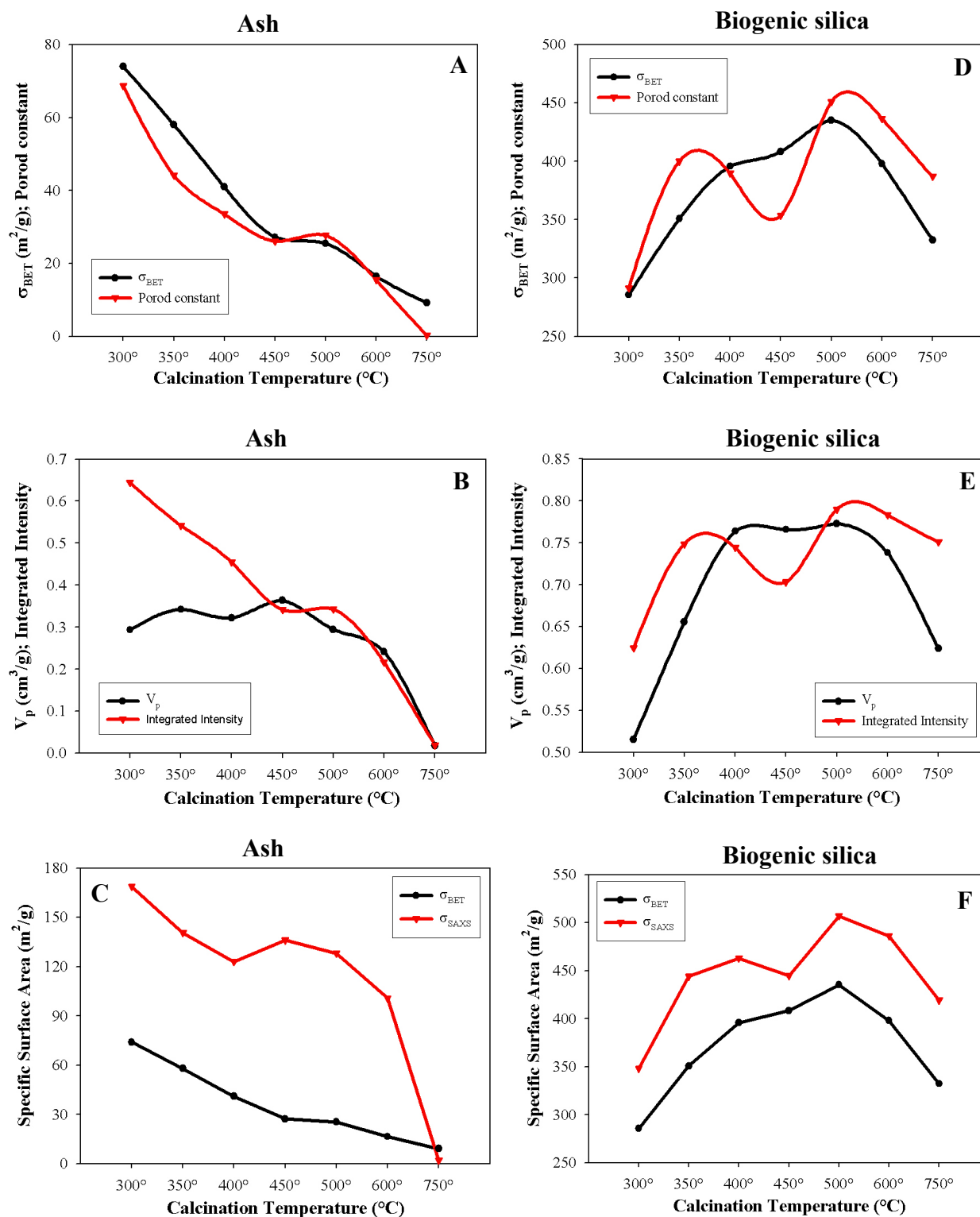


Figure 3.6 Comparisons of Porod constant vs. surface area from BET analyses, Integrated Intensity vs. pore volume, and surface area obtained from SAXS vs. surface area from BET analysis of ashes (A-C) and calcined HCl-treated samples (D-F). Since the Porod constant and Integrated Intensity are only known up to a constant factor, they were normalised with respect to the average values of σ_{BET} and pore volume of the corresponding 3 samples treated at 450°C, 500°C, and 600°C.

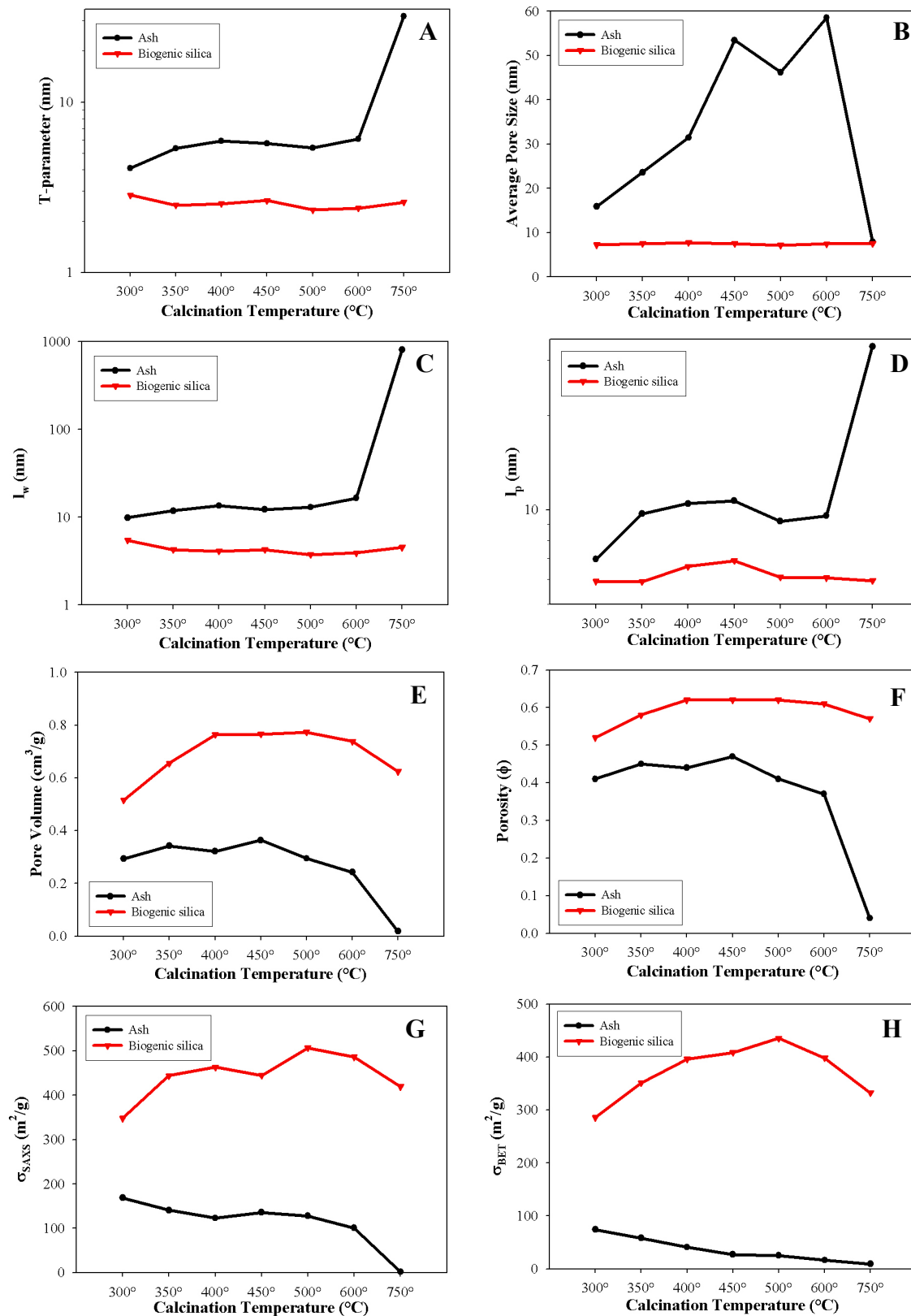


Figure 3.7 Comparisons of nanostructural parameters obtained from SAXS and nitrogen sorption analyses, such as T-parameter (A), average pore size (B), l_w (C), l_p (D), pore volume (E), porosity (F), σ_{SAXS} (G), and σ_{BET} (H) between ash and calcined HCl-treated samples.

Fig. 3.6 (A) and (D) show the comparisons between the Porod constant determined from SAXS (which is proportional to the total surface areas) and surface area from BET analysis of various ashes and calcined HCl-treated samples, respectively. Since the proportionality constant between the Porod constant and the SAXS surface area σ_{SAXS} (Eq. A.26) is not known, the data were normalized to the average values at 450°, 500°, and 600°C where all of the organics were considered to be fully burnt-off. The temperature dependence of these parameters obtained from SAXS and BET are qualitatively similar, but not identical. In particular for the ashes, there seems to be a discrepancy at low temperatures, which suggests a considerable amount of closed porosity in the ash samples at low temperatures. The consistency of SAXS and BET data was additionally corroborated by the similar patterns of the values of the integrated intensity from SAXS analysis (which is proportional to total pore volume fraction (Eq. A.27) and pore volumes obtained from BET analysis (Fig. 3.6 (B) and (E)).

Combining the porosity data obtained from nitrogen sorption analysis with Eq. A.28, the absolute value of the specific surface area from the SAXS analysis could be estimated without any assumption about the proportionality factor. Fig. 3.6 (C) and (F) show that the surface areas of the ash and calcined HCl-treated samples obtained from BET analysis (σ_{BET}) show similar temperature dependence as those calculated from the SAXS data (σ_{SAXS}). For the ash samples, the surface area decreased more or less continuously with temperature to a value close to zero at 750°C. The SAXS surface area is however considerably higher (up to a factor of four) as compared to the BET surface area. This confirms the speculation that the porosity in the ash sample is mostly not accessible. For the calcined HCl-treated samples, the maximum total surface area (500 m²/g) is reached at 500°C (Fig. 3.6 (F)). There were only insignificant differences between σ_{SAXS} to σ_{BET} for all calcined HCl-treated samples (Fig. 3.6 (F) and Table 3.3 (B)), thus suggesting a negligible amount of close pores in these samples.

Fig. 3.7 shows the comparisons of several nanostructural parameters for the ash and calcined HCl-treated samples, such as the mean chord length (T-parameter), the chord length of the pore walls (l_w) and the pores (l_p), the average pore size, the pore volume, the porosity, as well as the total surface area (σ_{SAXS}) and the BET surface area (σ_{BET}). The ash samples show higher values of the T-parameter, average pore size, l_w ,

and l_p (Fig. 3.7 (A)-(D)) in comparison to the calcined HCl-treated samples. In contrast, pore volume, porosity, σ_{SAXS} , and σ_{BET} of the calcined HCl-treated samples are superior compared to the ash samples. The T-parameter, l_w , l_p , and average pore size of the ash samples increase as the temperature increases, whereas those of calcined HCl-treated samples appear constant over the whole temperature regions. Furthermore, the pore volume, porosity, σ_{SAXS} , and σ_{BET} of the ash samples are gradually decreased with the increasing temperatures, whereas for calcined HCl-treated samples, these parameters appear to reach their optimum values within the temperature region between 400°C-500°C. Several fluctuated data are not only due to the instrument errors during the measurements but also due to the sample inhomogenities.

3.3 Discussion

Ashes containing of about 60% silica were obtained after thermal processing of the native samples in oxidising atmosphere. Amorphous silica was observed for the temperature range between 300°C and 600°C which was transformed into crystalline α -cristobalite during the heat treatment at 750°C. This may be due to the presence of inorganic impurities such as sodium and potassium containing compounds which are known to accelerate the formation of cristobalite at temperatures as low as 800 °C⁷⁵. In rice husk, cristobalite was identified upon calcination from 800°C onwards⁴⁴. In the present work, the removal of organics by calcination in air at 300°C was able to create an open porosity with surface area of about 80 m²/g. However, with increasing calcination temperature, the surface area decreased continuously to a value close to zero at 750°C when the amorphous silica was transformed into cristobalite.

Treatment of the native *E.hyemale* with HCl does not only substantially remove the inorganic impurities such as K and Ca, but also dissolves pectin¹³⁵, and hemicelluloses^{135, 136} in the organic matrix. Moreover, amorphous cellulose may also be dissolved¹³⁷ and crystalline cellulose undergoes partial hydrolysis leading to a reduction in degree of polymerisation yielding so-called hydrocellulose, which is the swelling state of cellulose¹³⁸. Due to the HCl action, about 95% inorganic impurities and 65% organics are removed leaving cavities and voids. Thus, a highly porous

material with BET surface area of about $60 \text{ m}^2/\text{g}$ is obtained, which is comparable to the maximum BET surface area of the ash samples at 300°C . Additionally, the siloxane bridging (-Si-O-Si-) on the surface of silica type 2 is likely to undergo hydrolysis leading to the formation of silanol groups identical to silica type 1 (see Fig. 2.20). Further calcination of HCl-treated samples leads to the more progressive pore development by the removal of the remaining organic tissue with a drastically increasing BET surface area by a factor of more than 5 ($\approx 300 - 450 \text{ m}^2/\text{g}$). In comparison to the ash specimens, there is no phase transformation of the amorphous silica into cristobalite at 750°C . Since inorganic impurities were removed here, the transformation is expected to occur at much higher temperature ($1200-1400^\circ\text{C}$,³²).

What needs to be discussed further is the instability of the porous silica structure upon calcination without prior HCl-treatment. The most probable reason is the interaction of silica with the inorganic impurities, mainly potassium^{47, 73}. Real *et al.*⁷⁴ provided some evidence from XAFS measurement that potassium oxide leads to the disruption of SiO_4 network into chain like structures of non-bridging oxygen atoms. Krishnarao *et al.*⁷³ correlated the formation of black (carbon fixed) particles in rice husk silica ash due to the surface melting of silica in the presence of potassium impurities. As the consequence, the weight loss due to the removal of moisture and adsorbed gases was low. This also explained the huge discrepancy between the high surface area of calcined HCl-leached rice husk ($260 \text{ m}^2/\text{g}$) and the low surface area of calcined untreated rice husk ($1 \text{ m}^2/\text{g}$) described by Real *et al.*⁴⁷. Although slow heating may eliminate the tendency of silica for carbon retention since carbon formation and its oxidation occurs before the dissociation of K_2O (620 K) and surface melting, the silica formed from untreated rice husks is not so bright (white) as silica formed from treated rice husks⁷³. Krishnarao *et al.*⁷³ also tried to impregnate the acid-leached rice husks with 4%-wt K_2CO_3 followed by calcination at 700°C for 3 hours to study the effect of potassium, and found similarities with the untreated samples. It seems plausible that the same mechanism is applicable to *E.hyemale*. Even though the concentration of potassium is much higher in rice husk as compared to *E.hyemale*, potassium is the most abundant inorganic elements present in *E.hyemale* besides calcium. The ash obtained from the calcination up to 600°C was grey indicating the remaining of carbon trapped in the samples. Only the ash obtained after calcination at 750° is pink whitish since silica

was transformed into cristobalite and the light pink color may derive from other impurities, such Fe and Mn ⁴⁹. In contrast, the HCl-treated samples calcined from 500°C onwards were perfectly white suggesting highly pure biogenic silica derived from *E.hyemale*. An alternative explanation for the stability of silica structure after HCl-treatment may be the pore opening. Since about 60% of the total plant mass was removed by the chemical treatment, a large accessible surface was present already prior to the thermal treatment. This may allow volatile reaction products to leave the solid framework without the creation of large internal stresses, which in the case of the ash might be partly responsible for the collapse of the pore structure.

Calcination of HCl-treated samples delivered biogenic silica with mostly open porosity. This can be interpreted as the effective removal of all remaining biopolymers without changing or destroying the structural integrity of the biogenic silica network. In comparison, silica obtained by treating *E.hyemale* with 30% H₂O₂ without subsequent thermal treatment (see chapter 2) also exhibits mostly open porosity. However, the BET surface area is around a factor of 2 lower ($\approx 250 \text{ m}^2/\text{g}$) and the treatment is very time consuming. Treatment of *E.hyemale* with HCl without calcination exhibits a much lower surface area, but the SAXS surface area is by more than a factor of two larger than the BET surface area. This indicates a considerable amount of closed pores after HCl treatment. Crystalline cellulose is still remaining in this case, which may be rearranged as a result of drying after chemical treatment, closing some of the pores again. For the ash samples, the close porosity relative to open porosity is larger by a factor of 2 to 6 as the calcination temperature increases, while the total surface area (σ_{BET} and σ_{SAXS}) decreases. This may occur because the volatile products from organics decomposition such CO₂ and CO increase as temperature increases. These gases remain mostly trapped inside the structure and cannot be easily released due to the surface melting of silica by the influence of potassium ⁷³. A coarsening of the silica particles in the ash samples due to interaction of silica with potassium is also reflected by the higher T parameter value, while the T parameter of the calcined HCl-treated samples is more or less constant over the whole calcination temperature range. The silica derived from the H₂O₂ treated sample has a T parameter lying in between the values of calcined native and calcined HCl-treated samples. This may be explained by the presence of Ca-

oxalates crystals which are additionally formed during the oxidation as proved by XRD and FTIR (see chapter 2).

Therefore it is clear that the inorganic impurities are unfavourable for the effective isolation of the biogenic silica from *E.hyemale*, and need to be removed in order to obtain high grade and high purity nano-sized silica. Chemical treatment without subsequent thermal treatment is not very useful for an effective and economic silica isolation due to the length of the treatment. Chemical treatment using HCl followed by calcination is found to be the most effective way to get high grade, amorphous silica with nanometer sized open porosity with very high surface area (activated biogenic silica). Thermal treatment at a low heating rate appears crucial for the pore development not only because of the removal of all organics but water in the silanol groups is also evaporated during heating leaving additional pores and cavities, which leads to structural rearrangements of silica into a highly mesoporous silica network. The optimum calcination temperature for HCl-treated sample was found to be around 500°C where pure biogenic silica with the highest surface area was obtained. Above this temperature, the surface area decreases, most probably due to the collapse of pores.

3.4 Summary

In this chapter, amorphous silica was isolated from *E.hyemale* by purification via both, chemical and thermal treatments. Two sets of samples, namely ash and biogenic silica samples were prepared by calcination of native and HCl-treated *E.hyemale*, respectively. Calcination was carried out at 7 different temperatures between 300°C and 750°C with a very slow heating rate of 1 K/min and holding time of 48 hours. The resulting ash and biogenic silica samples were subjected to nanostructural investigations using the combination of powder diffraction, SAXS, and nitrogen sorption.

The ash samples contain roughly 60% silica mostly in the form of amorphous silica. The remaining 40% consist of other inorganic compounds such as CaCO₃ and KCl. The amorphous silica in these ash samples was transformed into α -cristobalite during the heat treatment at 750°C. In contrast, this transformation did not take place in the corresponding calcined HCl-treated sample. SAXS and nitrogen sorption reveal the presence of slit-like pores with a thickness of 6-7 nm in the biogenic silica samples with a rather narrow size distribution. The calcined HCl-treated samples show considerably higher pore volume, porosity, and total surface area as compared to the corresponding ash samples. The optimum calcination temperature appears to be about 500°C, where high grade pure amorphous silica with completely white colour and BET surface area of $\approx 400 \text{ m}^2/\text{g}$ is obtained. This *E.hyemale* derived biogenic silica may well have potential applications as adsorbents or catalyst supports for instance and also as raw materials for the synthesis of versatile industrial silicon-based products.

Chapter 4

Silicon Carbide (β -SiC) from *Equisetum hyemale*

In this chapter it was attempted to produce silicon carbide (β -SiC) based on the abundant and low-cost naturally growing "material" horsetail. With silica as the source of silicon and the organic biomolecules as the source of carbon, one simple thermal conversion step is in principle sufficient for this purpose. The highly reactive biogenic amorphous silica is expected to react with carbon present in high amount to form silicon carbide upon pyrolysis at high temperature ($>1300^{\circ}\text{C}$)⁶⁸. One main advantage of this process is that there is no need to add any additional precursor material. The goal of the present work was to show the principle feasibility to produce the β type of SiC which has a cubic crystal structure. All *E.hyemale* samples were tempered in inert atmosphere at temperatures from 1500°C - 1600°C to prevent the formation of α -SiC which starts at about 2000°C ⁶⁸.

Several preliminary studies on the formation of β -SiC under different inert atmospheres, namely under vacuum (SiC/C 1) and argon (SiC/C 2) were performed using a two-step pyrolysis approach. The first step consisted of the pyrolysis of native *E.hyemale* internodes at 1000°C with a heating rate of 2 K/min and a holding time of 2 hours at the maximum temperature for the transformation of all biopolymers into amorphous carbon. In the second step, the samples were transferred to a second furnace for the heat treatment at high temperature (1600°C) to allow the reaction between amorphous carbon and amorphous silica delivering β -SiC. A fast heating rate of 13 K/min and a short holding time of 0.5 h were applied during this latter process.

A second attempt for β -SiC synthesis was conducted in a different furnace by applying a single pyrolysis step from room temperature to 1500°C in argon atmosphere (SiC/C 3). A longer holding time (2 h) was maintained to allow more contact time between carbon and silica with the aim to eventually obtain higher yield of SiC. This sample was further purified by calcination at 750°C to remove the remaining carbon and finally chemically treated with hydrofluoric acid (HF) to remove all unreacted silica and

also silica which might have additionally been formed by the oxidation of SiC. With this procedure, pure β -silicon carbide was obtained (SiC 1).

In a third attempt, the HCl-treated *E.hyemale* samples were used as precursor for the β -SiC synthesis. The HCl-treated sample (see previous section) was first pyrolysed at 400°C, held for 100 h, followed by further heating to 1500°C, held for 6 h. The final material was then subjected to calcination at 750°C and HF treatment, and SiC 2 was obtained.

All samples together with their corresponding treatments are summarised in Table 4.1. Several characterisation techniques were applied for the structural investigation of the resulting materials. WAXS was used to identify the different phases present in each system. Additional structural analysis using SEM, SEM/EDX, microtomography, SAXS and nitrogen sorption were performed in some of the samples.

Table 4.1 *E.hyemale* derived SiC samples and their preparation

Samples	Pre-treatment	Heat Treatment 1	Heat Treatment 2	Post-treatment
SiC/C 1	-	Pyrolysis in vacuum atmosphere from room temperature to 1000°C (2 K/min, 2 h, furnace 1).	Pyrolysis in vacuum atmosphere from room temperature to 1600°C (13 K/min, 0.5 h, furnace 2).	-
SiC/C 2	-	The same procedure as SiC/C 1.	The same procedure as SiC/C 1 but in Ar atmosphere.	-
SiC/C 3	-	Pyrolysis in Ar atmosphere from room temperature to 1500°C (12 K/min, 2 h, furnace 3).	-	-
SiC 1	-	The same procedure as SiC/C 3.	-	Calcination at 750°C for 1 h. Chemical treatment with 40% HF at boiling temperature.
SiC 2	Chemical treatment with 10% HCl (48 h) at boiling temperature.	Pyrolysis in Ar atmosphere from room temperature to 400°C (1 K/min, 100 h, furnace 3).	Pyrolysis in Ar atmosphere from 400°C to 1500° (2 K/min, 6 h, furnace 3).	Calcination at 750°C for 1 h. Chemical treatment with 40% HF at boiling temperature.

See Appendix B for the detailed specifications of furnace 1,2,3 and for the detailed heat treatment processes for the SiC production.

4.1 Microtomography

Three dimensional visualisation images of SiC/C samples (SiC/C 1, SiC/C 2, and SiC/C 3) acquired by microtomography are depicted in Fig. 4.1. SiC/C 1 and SiC/C 2 show that the original macroscopic shape of the samples was largely retained after the heat treatment, in contrast to SiC/C 3 sample which was mostly collapsed and the original stalk structure is only partly retained.

The "contrast" from blue to red is proportional to the grey-values, and therefore a measure of the local X-ray absorption coefficient. Similar to Chapter 2, the outer surface and in particular the knobs in SiC/C 1 and SiC/C 2 samples show the highest contrast, whereas in the SiC/C 3 sample a rather homogeneous absorption contrast is seen on the entire outer surface. These patterns are supposed to reflect the distribution of β -SiC formed within the pyrolysed *E.hyemale* stalks which were more or less similar to the distribution of silica in native *E.hyemale* internodes (see Fig. 2.5 for comparison). However, the more homogeneous contrast within the samples treated under argon (SiC/C 2 and SiC/C 3) in comparison to SiC/C 1 which was thermally treated in vacuum qualitatively suggested the higher yield of β -SiC formation over the outer surface of the pyrolysed *E.hyemale* stalks.

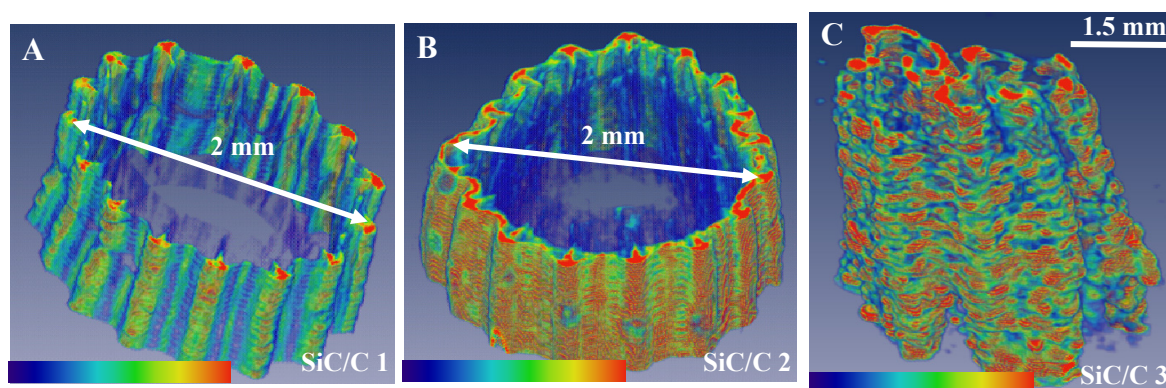


Figure 4.1 3D rendering of X-ray micro-CT reconstructed images of SiC/C 1 (A), SiC/C 2 (B), and SiC/C 3 (C) acquired by Amira software.

4.2 SEM/ EDX analysis

The microstructure of β -SiC (SiC 1 and SiC 2) obtained after the post-treatment processes was investigated by SEM. Interestingly, the final SiC materials resembled the original structure of the outer surface of the native *E.hyemale* stalks. One can still distinguish the furrow region occupied by two parallel rows of stomata separated by the ribbed portion (Fig. 4.2 and Fig. 4.3 vs. Fig. 2.16). However, the structure is strongly distorted as compared to the biological template marked by the much denser and coarser structure due to a strong shrinkage. Furthermore, merging of the two knob rows in the ribbed portion is noticed in SiC 1 sample (Fig. 4.2) and even the knobs containing pure hydrated amorphous silica (see chapter 2) vanished in SiC 2 sample. The silica in the knobs might be converted into silicon monoxide gas which is either diffused into the epidermis and react with carbon to form SiC or diffused over the reaction chamber and was probably driven away by the flowing argon gas before reacting with carbon to form β -SiC within the selected process condition (Fig. 4.3). The morphology of SiC 2 retained the original silica structure to a larger extent in comparison to SiC 1, even though the knobs are missing in this sample. It is seen in Fig. 4.3 (C) that the stomata and warty-like protuberances within the furrow region are more pronounced as compared to (Fig. 4.2 (B) (compare also with the native tissue Fig. 2.16 (L)).

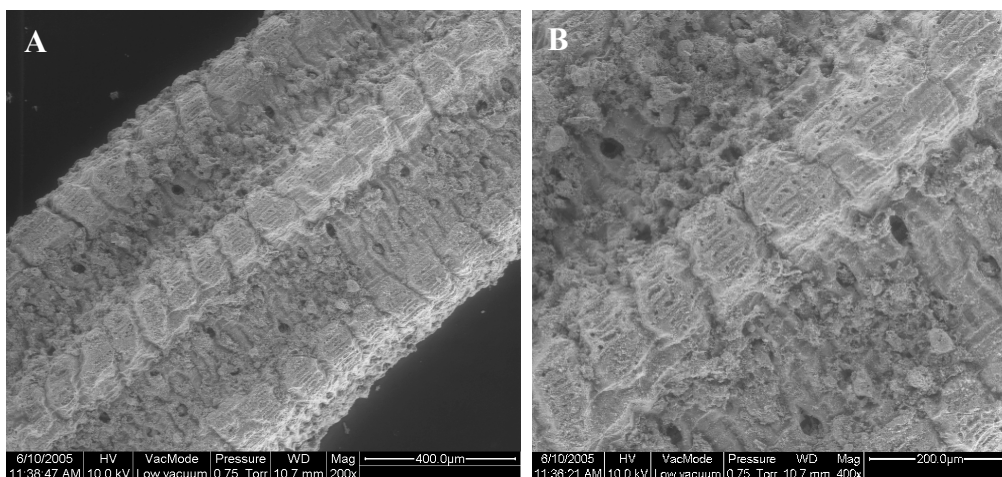


Figure 4.2 SEM images of SiC 1

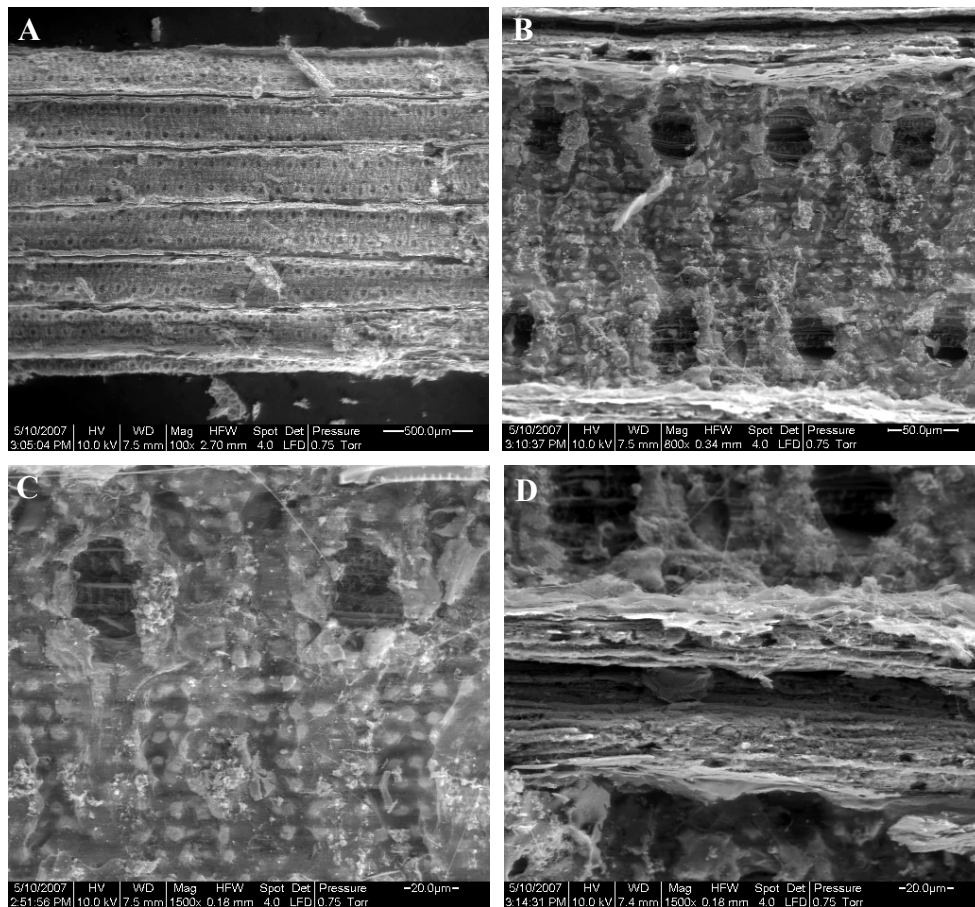


Figure 4.3 SEM images of SiC 2 showing the morphology taken on different regions: *E.hyemale* derived SiC body (A), the furrow region (B), the stomatal region (C), and the ridge/ knob region (D).

Fig. 4.4 shows the semi-quantitative SEM/EDX analysis of SiC/C 3 sample. Silicon was found at its highest concentration up to 53% in the knob, followed by the other regions at epidermal flank, stomata, and small particles in the furrow region of which silicon contents are about 24%, 35%, and 42%, respectively. This pattern is consistent with the previous SEM/EDX analysis in the native *E.hyemale* showing the highest silicon content in the knob tip of around 33% (see Fig 2.9). However, the silicon content in this sample is by a factor of about 2 larger compared to those detected in the native *E.hyemale*. The decrease of the total illuminated volume due to a significant shrinkage during the heat treatment would mostly account for this discrepancy. Furthermore, only Ca and Al elements were detected in the pyrolysed *E.hyemale*. Al was most probably derived from the alumina crucible since it is hardly

found in the native *E.hyemale* (see Table 3.1). K, Mg, and Na which were also found in the native *E.hyemale* were not detected since they probably volatilized after being subjected to high temperature above 1400°C¹³⁹. Spherical particles lying over the outer surface in the furrow region (Fig. 4.4 (B)) were formed during the pyrolysis of *E.hyemale* within the selected condition for SiC/C 3. They are suggested to be mainly β -SiC particles mixed with a small amount of Ca and Al containing silicate compounds as suggested from the SEM/ EDX analysis.

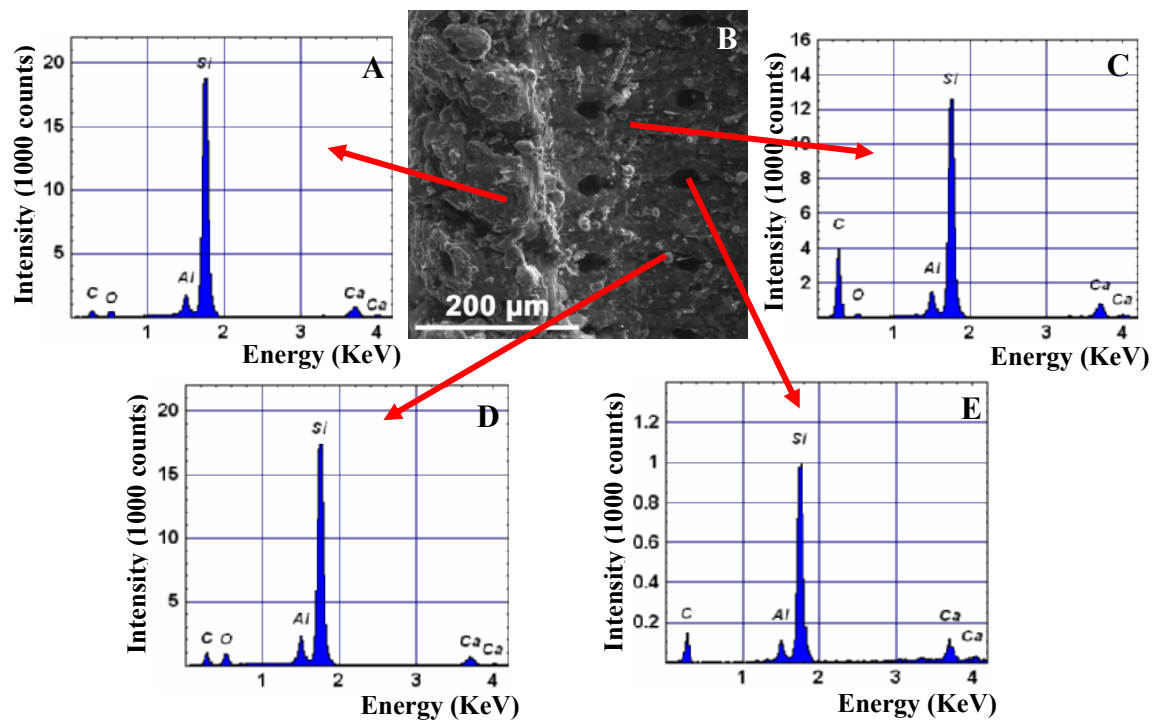


Figure 4.4 Secondary electron image of SiC/C 3 (A) with several EDX spectra taken at four different positions indicated by the arrows at the knob tip (A), epidermal flank (C), small particle (D), and stomata (E). The silica content in weight percent relative to all elements detected within the local illuminated sample volume was calculated for A,C,D,E as about 53%, 24%, 42%, and 35% \pm 2%, respectively.

4.3 Powder Diffraction/ WAXS

The WAXS patterns of SiC/C 1, SiC/C 2, SiC/C 3, and SiC 1 can be seen in Fig. 4.5, exhibiting some clear differences. In SiC/C 1 and SiC/C 2 samples, there was still large amount of carbon remained after the pyrolysis compared to SiC/C 3 sample. This was clearly seen in the WAXS signals from carbon (002) reflection at $q = 17 \text{ nm}^{-1}$ which is anisotropic and reflect a preferred orientation of the carbonaceous graphene

layers with respect to the original cellulose orientation¹¹³. Another carbon peak (10) ascribed to in-plane ordering of the aromatic carbonaceous structures is observed at $q = 11 \text{ nm}^{-1}$ ¹¹³. The other reflections are homogeneous powder rings, i.e. there is no texture of the SiC crystals. β -SiC was formed in all samples marked by the main reflection (111) at $q = 25 \text{ nm}^{-1}$. The other peak at $q = 28.9 \text{ nm}^{-1}$ is corresponding to (200) reflection of β -SiC. This peak is not seen in SiC/C 1 which was treated in vacuum. Additionally, the peak of (111) reflection of β -SiC was rather small and broad in SiC/C 1 indicating the formation of β -SiC at the initial stage. In contrast to SiC/C 1, which was treated in vacuum, the argon treated samples (SiC/C 2, SiC/C 3) showed much sharper peak of β -SiC, indicating greater amount of β -SiC with larger grain sizes formed under this condition. Furthermore, in comparison to SiC/C 2, the SiC/C 3 sample shows much stronger and sharper peak of β -SiC besides the lower carbon peak, revealing that the one-step processing approach gives the highest SiC yield. Additionally, the longer holding time at high temperature most probably favours a higher conversion of silica and carbon into SiC. The shoulder at $q = 23.8 \text{ nm}^{-1}$ might be attributed to stacking faults in β -SiC¹⁴⁰.

In the argon treated samples (SiC/C 2 and SiC/C 3), several additional reflections are observed that cannot be attributed to carbon or β -SiC. There was no cristobalite observed in these samples, which is known to be formed at low temperature ($< 1250^\circ\text{C}$) during the thermal treatment⁵⁵. This suggests the transformation of amorphous silica into silicate compounds containing probably Ca and Al as suggested by EDX. The peaks at $q = 22.5 \text{ nm}^{-1}$ and 26.5 nm^{-1} in SiC/C 2 may be attributed tentatively to $\text{Al}_2\text{O}_3 \cdot 3\text{CaO} \cdot 2\text{SiO}_2$ (gehlenite) and the prominent peak at $q = 18.4 \text{ nm}^{-1}$ in SiC/C 3 can be ascribed to Al_2SiO_5 (sillimanite).

Further purification of SiC/C 3 samples by calcination followed by HF treatments leads to pure β -SiC (SiC 1 sample). Nevertheless, the β -SiC product is again accompanied by insoluble inorganic compounds, for instance CaF_2 ($q = 20 \text{ nm}^{-1}$) as a result of the reaction of silicate compounds with HF during the chemical treatment (Fig. 4.5). Therefore, in a final attempt it was tried to produce pure β -SiC within the laboratory scale by using the HCl-treated *E.hyemale* (see App. B) as precursor (SiC 2). With this approach, any silicate compounds formation due to the inorganic impurities would be eliminated. The fingerprint of highly crystalline, pure β -SiC was obtained as

being proved by the powder diffraction (WAXS) pattern shown in Fig. 4.6. Thus, the use of HCl-treated *E.hyemale* as precursor, i.e. starting material which is free of inorganic impurities is very crucial in determining the desired final purity of β -SiC

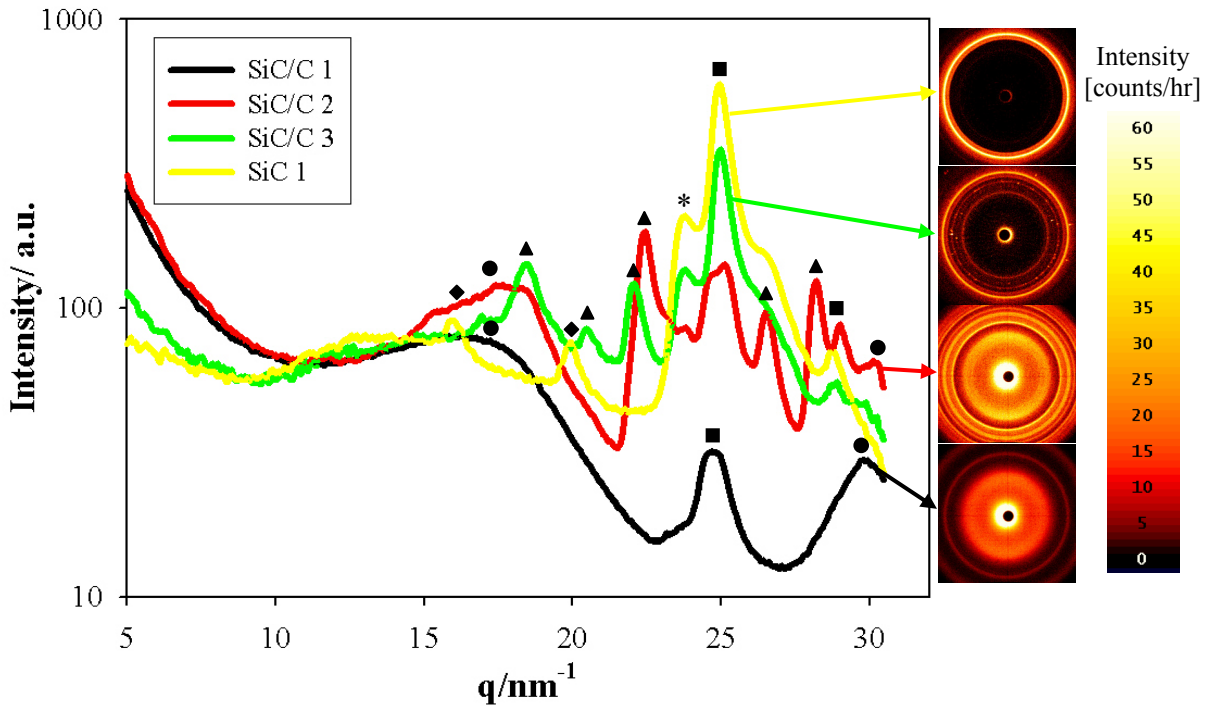


Figure 4.5 WAXS patterns of SiC/C 1, SiC/C 2, SiC/C 3, and SiC 1. SiC/C samples were derived from the *E.hyemale* pyrolysed at high temperatures in an inert atmosphere, whereas SiC 1 sample was obtained after the post-treatment of pyrolysed *E.hyemale* by HF treatment and calcination (see Table 4.7 for the details). ■: β -SiC, ●: carbon, ▲: silicates, ◆: insoluble inorganic compounds after post-treatment, and * might indicate stacking faults in β -SiC crystal.

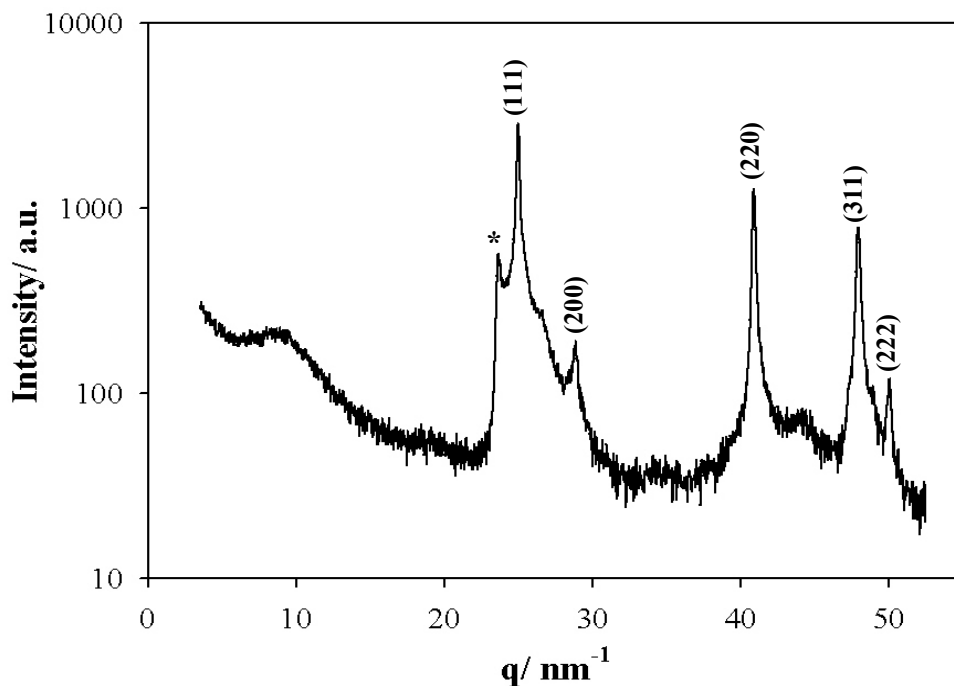


Figure 4.6 Powder diffractogram of SiC 2 showing the fingerprint of pure β -SiC. * might indicate stacking faults.

4.4 SAXS

SAXS was carried out only in two samples, namely SiC/C 3 and SiC 1 of which patterns are displayed in Fig. 4.7. Porod's law marked by the proportionality of the curve to q^{-4} prevailing over almost the whole q range in SiC 1 in contrast to SiC/C 3 sample. This indicates that the scattering in the SiC/C 3 sample is dominated by the amorphous carbon compound which is expected to be highly microporous, supported by the clear shoulder at $q \approx 2 \text{ nm}^{-1}$. In contrast, the SiC 1 SAXS profile shows no structure over the whole measured q -range, indicating a very broad pore size distribution. The mean chord length (T-parameter) of SiC/C 3 and SiC 1 were about 1 nm and 7 nm (see Table 4.2), respectively. It should be noted, that in particular for SiC 1, this is a lower estimate, since the integrated intensity cannot be reliably estimated for low q -values.

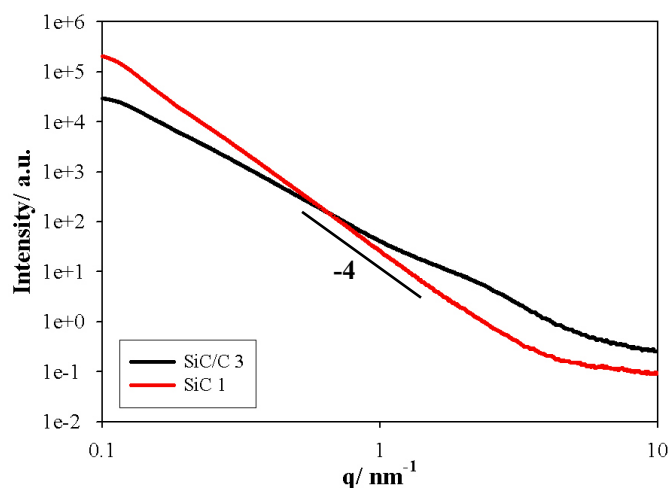


Figure 4.7 SAXS patterns of SiC/C 3 and SiC 1. The lines indicate the power-law behaviour of the scattering intensity with $I \propto q^{-4}$ (Porod's law).

4.5 Nitrogen sorption

Nitrogen sorption experiments in 3 samples, i.e. SiC/C 3, SiC 1, and SiC 2 were performed in order to study their surface area, pore size distribution, and pore structure. These parameters will determine the features of *E.hyemale* derived SiC materials whether they fulfil the required standard qualifications for certain technical applications or not.

The nitrogen sorption isotherms of all samples showed hysteresis loops which are characteristic for mesoporous structures (Fig. 4.8 (A)-(C)). The BET surface area for SiC/C 3, SiC 1, and SiC 2 are 42 m²/g, 17 m²/g, and 12 m²/g, respectively (Table 4.2). Pore size distribution of SiC 1 is much broader in comparison with that of SiC/C 3 (Fig. 4.8 (E) vs. (D)) and qualitatively consistent with SAXS. Other nanostructural parameters of these samples are listed in Table 4.2. The SiC/C 3 sample has a very large total area according to the SAXS data, which may be mainly attributed to microporosity in the carbon phase, which is not accessible to the nitrogen. In case of SiC 2 sample, the pore size distribution is narrower compared to SiC 1 by only showing several peaks in the mesoporous region in addition to the presence of micropores at pore diameter \approx 2 nm (Fig. 4.8 (F)) resulting in a much lower average pore diameter (\approx 11 nm) which is around a factor of 2 lower than that of SiC 1 sample (see Table 4.2).

Table 4.2 Nanostructural parameters of SiC/C 3, SiC 1, and SiC 2 based on SAXS and nitrogen sorption analysis.

Parameters	SiC/C 3	SiC 1	SiC 2
Mean chord length, T (nm)	1.14	7.11	
BET surface area, σ_{BET} (m ² /g)	41.73	17.14	12.06
Pore Vol., V_p (cm ³ /g)	0.204	0.114	0.034
Porosity, ϕ	0.32	0.27	0.10
Average pore diameter, D_p (nm)	19.52	26.52	11.36
SAXS surface area, σ_{SAXS} (m ² /g)	483.48	46.86	
Pore chord length, l_p (nm)	1.69	9.71	
Wall chord length, l_w (nm)	3.51	26.51	
$\sigma_{\text{SAXS}}/\sigma_{\text{BET}}$	11.59	2.73	

SiC 2 sample is only characterised by nitrogen sorption without being coupled with SAXS measurement.

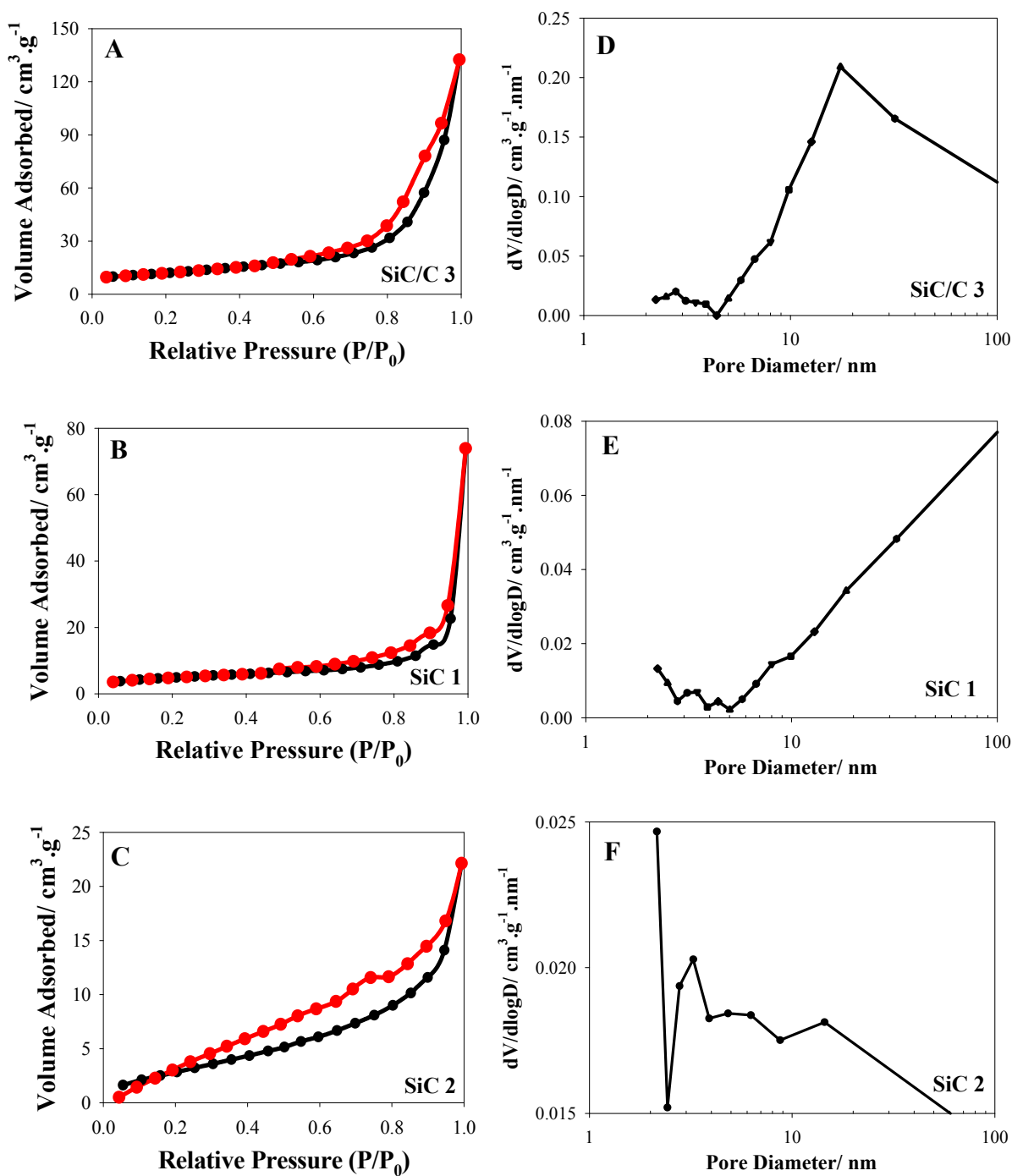


Figure 4.8 Nitrogen sorption isotherms and pore size distributions of SiC/C 3, SiC 1, and SiC 2. (A), (B), and (C) are figures of the nitrogen sorption isotherms of SiC/C 3, SiC 1, and SiC 2, respectively, whereas (D), (E), and (F) show their pore size distributions from BJH analysis of the adsorption branches, respectively.

4.6 Discussion

There are significant differences between β -SiC obtained from thermal treatment of HCl-treated *E.hyemale* and native *E.hyemale*. SiC derived from HCl-treated *E.hyemale* (SiC 2) shows a more pronounced hysteresis loop compared to the SiC derived from native *E.hyemale* (SiC 1) indicating a more defined mesoporous structure with a considerably lower average pore size. The much lower surface area of SiC in comparison to that of biogenic silica from calcined-HCl treated *E.hyemale* (see chapter 3) may be due to sintering of particles during the heat treatment at high temperature (1500°C). Therefore, collapsing of pores is more intense compared to silica obtained after calcination at relatively low temperature (< 1000°C).

The SiC distribution in *E.hyemale* is restricted to the outermost layer where silica and carbon are intimately associated in the continuous layer adjacent to the epidermal cell wall (see chapter 2). The micromorphology of pyrolysed HCl-treated *E.hyemale* (SiC 2) by SEM reveals similarity with that of the native *E.hyemale*. Only the knobs are missing since they are most probably converted into silicon monoxide gas, and due to the missing carbon source in the knob tips, SiC formation is not possible. It is obvious that SiC will be easily formed when silica and carbon are intimately present or if they are getting into close contact during the pyrolysis. This study shows the possibility of conversion of sustainable and low-cost *E.hyemale* into biomorphous β -SiC, which is of technical interests, for instance as high performance advanced ceramics.

4.7 Summary

In this chapter, attempts towards the synthesis of β -SiC from *E.hyemale* were undertaken. Different inert atmospheres (vacuum and argon) and different precursor materials (native and HCl-treated *E.hyemale*) were subjected to selected processing conditions. It was found that direct pyrolysis and pyrolysis in argon atmosphere is more promising to obtain higher yield of β -SiC. Additionally, HCl-treatment of the native *E.hyemale* prior to pyrolysis is highly recommended to get β -SiC with high purity without the formation of undesirable silicates or insoluble inorganic compounds after post-treatment using HF. Removal of such silicate compounds after the pyrolysis is not only very difficult but also implies additional costs. A mesoporous β -SiC structure with a moderate surface area of about 12 m²/g is obtained which may be improved by future optimisation. Potential applications include refractory materials, adsorbents, or catalyst supports.

Chapter 5

Conclusions and Outlook

5.1 Conclusions

The first part of this thesis reports a comprehensive analytical and microstructural investigation of silica in the perennial scouring rush, *Equisetum hyemale*. The scientific interest concentrates on the better understanding of the role of silica in higher plants in general and in *Equisetum*, which is one of the strongest silica accumulating plant, in particular.

Silica accumulations within *E.hyemale* stalks increased from about 6% to 14% during the growing period (June – November 2005). Silica contents within mature *E.hyemale* stalks decreased basipetally from about 15% to 10% without any significant differences between internodes and nodes and the cone contained about 11% silica. These results support the idea already formulated in the literature that silica is an essential nutritional element for the development of *E.hyemale*.

Within the internodes of *E.hyemale*, silica is mostly amorphous and is distributed in a continuous manner on the entire epidermal layer with the highest silica concentration on the knob tips. One of the key results of the present work is that there are two different silica modifications present in *E.hyemale*. The first type is pure hydrated amorphous silica without any interactions with polysaccharides, and is restricted to the knob tips. The second type is non-hydrated amorphous silica which is deposited in the continuous layer adjacent to the epidermal cells. This silica modification appears to be intimately associated with polysaccharides (cellulose, hemicellulose, pectin) and inorganic compounds. The primary silica particles have generally a sheet-like structure with a thickness of only a few nanometers. Taken together, these results demonstrate clearly that silica in *E.hyemale* is definitely not an unwanted by-product which the plant needs to get rid of. The strong (chemical) association with the cell wall polymers together with its colloidal appearance and plate like shape strongly suggests that the plant biopolymers act as a biological template, controlling essentially the silica synthesis in the plant.

Several possible functional roles of silica in *E.hyemale* are proposed based on the results of this study and in accordance with literature: a) silica is an essential element for the plant growth; b) silica supports and strengthens the main functions of the cuticle in protecting the plant body, in controlling the excessive water loss, and in serving as a defence against contact-probing insects and fungi; c) silica may play a beneficial role in improving the biomechanical properties such for instance flexural rigidity of the *E.hyemale* stem.

The second part of the thesis is devoted to the isolation of the biogenic silica from *E.hyemale* while trying to retain its nanostructure and also the whole hierarchical structure as far as possible. The goal was to lay the grounds for a cheap and efficient synthesis of high grade mesoporous biogenic silica from the renewable plant resource *E.hyemale*.

A chemical treatment with 30% hydrogen peroxide for 18 months resulted in pure silica that perfectly resembled the original outer shape of the original plant stalk, showing all ornamental surface features such as knobs, stomatal apparatus including the guard cells and subsidiary cells and wart-like protuberances on the grooves. Moreover, the nanostructure is characterized by small pores, an open porosity and quite large surface area. This demonstrates and supports impressively the results of the first chapter about the continuous silica "jacket" with a pronounced nanostructure. This H₂O₂ treatment is however not of practical use due to its extremely long duration. Heat treated *E.hyemale* also retain largely the original structure, even though not as perfect since shrinkage leads to distortions in the original hierarchical structure.

Silica isolation by thermal treatment of native *E.hyemale* in air leads to ash with only moderate surface area, which decreases with increasing calcination temperature and vanishes at 750°C. Moreover, at 750°C crystalline cristobalite replaces the amorphous silica found at the lower temperatures. In contrast, when native *E.hyemale* is subjected to a treatment with hydrochloric acid, high purity mesoporous silica with high surface area (up to 400 m²/g) is obtained, with only little temperature dependence up to 750°C. Also no phase transformation to cristobalite takes place for the HCl treated silica. These differences between HCl treated and native precursor are attributed to two beneficial

effects of the chemical pre-treatment: a) HCl removes all the inorganic alkali ions that are known to strongly interact with silica during the thermal treatment, and thus may destroy the unique nanostructure of the biogenic silica framework. b) The removal of inorganic compounds together with a considerable part of the organic polymers (except crystalline cellulose) opens up the porous structure already before the thermal treatment. In the subsequent calcination process, reaction gases can escape, which in turn avoids the collapse of the pore structure due to internal stresses. Additionally, during the HCl treatment, hydrolysis of siloxane bridging (-Si-O-Si-) on the surface of silica type 2 into silanol groups identical to silica type 1 takes place.

Therefore, a main conclusion of this study is that an HCl treatment prior to calcination is very advantageous in order to produce highly porous biogenic silica with high purity. The optimum calcination temperature lies around 500°C for this process. *E.hyemale* derived biosilica with its high specific surface area may well have potential industrial applications, e.g. as adsorbents or catalyst supports.

The third part of this thesis finally attempted to synthesise biomorphous SiC from the sustainable and low-cost raw material *E.hyemale* by simple pyrolysis using silica as the silicon source and the biopolymers as carbon source.

It could be shown that β -SiC can indeed be produced by simple pyrolytic decomposition of *E.hyemale* while at least partially retaining the original stalk structure. Direct (single step) pyrolysis and in particular pyrolysis in argon atmosphere promote higher conversion rates of silica into β -SiC as compared to treatment in vacuum. HCl-treated *E.hyemale* turns out to be a suitable precursor to get high grade β -SiC with high purity and low pore size. Similar to the case of the silica isolation in chapter 2, this better performance of the HCl treated samples as compared to the native tissue is explained by the negative influence of the additional alkali ions present in native *E.hyemale*, leading to the formation of undesirable silicates or insoluble inorganic compounds after the post-treatment with HF. The mesoporous SiC with a moderate surface area of about 12 m²/g derived from pyrolysed HCl-treated *E.hyemale* may find applications as refractory material, catalyst support, or advanced ceramics.

5.2 Outlook

1. A comprehensive study of silica in *E.hyemale* using different techniques at all hierarchical levels was performed in the present thesis in order to characterise and understand local silica distribution, silica type, crystallinity, and nanostructure. Some conclusions about the possible role of silica could be drawn, however, many issues related to the detailed biological function of silica remain unanswered. For instance the question why *Equisetum* tends to accumulate the largest amount of silica on their tissues among all higher plant and how silica is taken up by the roots into *E.hyemale* stalks are still elusive and further studies would be required. Also many physiological aspects such as more detailed investigations of silica in the different locations (e.g. nodes, leaves) and at different age (e.g. during the overwintering and over several seasons) would have to be investigated in more detail. Also the detailed mechanism of the Si involvement in the plant metabolism during the growth of *E.hyemale* needs definitely further investigations. Finally, the specific biological roles of silica in particular as a protective layer against excessive water loss, against insects and fungi, and its role in improving biomechanical properties are still rather speculative and therefore more specifically designed experiments would have to be performed.
2. An important aspect to be further investigated is the interaction of organic matter with silica in the living plant, and the possibility of the existence of organosilicon or other chemical forms of silicon compounds in *E.hyemale*. Particularly, it would be very interesting to understand how silica formation is controlled by the different biomolecules. This may enable new ways to tailor bioinspired inorganic materials such as nanostructured silica with novel properties *in vitro*.
3. Process optimisation and/or modification for a low-cost mass production of high yield and high purity biomorphous ceramics (SiO_2 , SiC) from *E.hyemale* need certainly further work. Basic investigation of the chemical and physical properties of these biomorphous ceramics (SiO_2 , SiC) are needed to verify, for instance, their superior mechanical and thermal properties. This would enable one to evaluate the

specific requirements for diverse industrial applications, such as for instance medicine, cosmetics, catalysts, chromatography columns, foods, paints, adhesives, fillers, refractory materials, and semiconductors.

Appendix A

CHARACTERISATION METHODS

Biological materials, such as plant tissues or bone, have a hierarchical structure, which is optimized at all levels^{141, 142}. Therefore, it is essential to characterise the structure of such biological tissues at all levels to understand their complex behaviour. The structure of such plant tissues is dispersed over at least eight orders of magnitude, thus many different techniques are necessary to be applied as there is no single technique cover such a large scale¹⁴¹. Characterisation techniques used for the structure investigations at different levels within this research work are represented in Figure A.1.

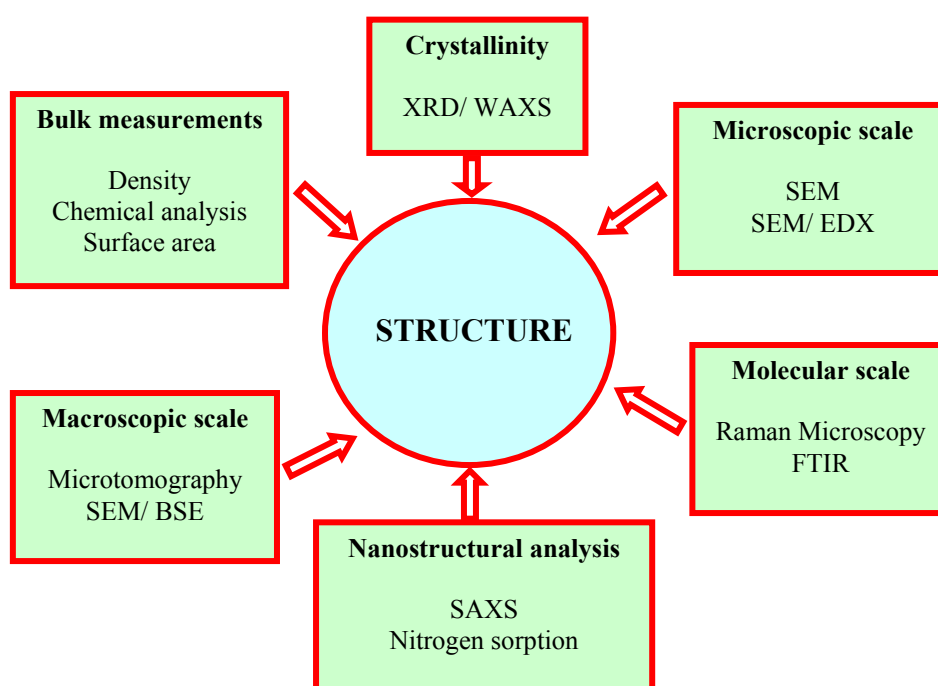


Figure A.1 Schematic view of a characterisation methodology at different hierarchical levels used for the study of amorphous silica in *E.hyemale*.

The methods such X-ray microtomography, Raman, FTIR, SAXS/WAXS are in principle based on the interaction of electromagnetic waves with matter, whereas scanning electron microscopy (SEM) is based on the interaction of electrons with matter. According to quantum theory, electromagnetic radiation can also be considered as a stream of *particles* called quanta or photons. Electrons also exhibit wave-particle

duality after the experiment of Louis de Broglie in 1924. The electromagnetic spectrum covers wavelengths from thousands of kilometres down to fractions of the size of an atom. The shorter the wavelength is the higher is the frequency and energy of the electromagnetic wave. They are related according to the Equation A.1.

$$E = h\nu = h\frac{c}{\lambda} \quad (\text{Equation A.1})$$

Where E is energy, h is Planck's constant ($h \approx 6.63 \cdot 10^{-34}$ J.s), ν is frequency, c is speed of light ($c \approx 3 \cdot 10^8$ m/s) and λ is wavelength.

X-rays, unlike ordinary light, are invisible. They travel in straight lines and affect photographic film in the same way as light, much more penetrating than light, and can easily pass through the human body, wood, quite thick pieces of metal, and other "opaque" objects ¹⁴³. Thus, X-rays are a powerful tool in material science for investigating the internal structure of the objects without any destruction.

A.1 X-ray Microtomography

Tomography refers to the cross-sectional imaging of an object from either transmission or reflection data collected from many different directions, rendering a non-destructive three dimensional visualisation of the internal structures of objects ¹⁴⁴. X-ray computed tomography (CT) is a relatively new technique developed in the late 1970's. Tomography is widely used for medical applications. Micro-CT instruments are based on the same principles as medical CT, but they have the advantage of an enhanced resolution down to 5 μm by the use of a microfocus ¹⁴⁵.

The technique is based on the interaction of X-rays with matter where X-rays are attenuated as passing through an object. For monoenergetic X-rays, the attenuation in matter is given by Lambert-Beer's law of absorption, which states that each layer of equal thickness absorbs an equal fraction of radiation that traverses it and is expressed mathematically as follows:

$$\frac{dI}{I} = -\mu \cdot ds \quad (\text{Equation A.2})$$

Where I is the intensity of the incident radiation, dI/I is the fraction of radiation removed from the beam as it traverses a small thickness of material, ds and μ is the linear attenuation coefficient. After integration, the more familiar form of Equation A.2 is obtained:

$$I = I_0 \cdot e^{-\int \mu(s) \cdot ds} \quad \text{or} \quad \int \mu(s) \cdot ds = -\ln \frac{I}{I_0} \quad (\text{Equation A.3})$$

Where the I_0 is the intensity of the unattenuated radiation and I is the intensity of the transmitted beam after it has passed a layer of material of thickness s and the linear attenuation coefficient μ . The linear attenuation coefficient is a measure for the attenuation per unit distance. It is specific for the used X-ray energy and for the type of absorber. This attenuation is dependent on the density and atomic number of the object as well as the X-ray energy used, according to Eq. A.4 since the photoelectric absorption and Compton scattering processes are predominantly involved in the energy ranges used¹⁴⁶.

$$\mu(E) = a(E)\rho \frac{1}{E^n} \frac{Z^m}{A} + b(E)\rho \frac{Z}{A} \quad (\text{Equation A.4})$$

Where E is the X-ray energy, ρ is the density of the absorber, Z is the atomic number, A is the atomic weight, and m and n values that depend on the energy and atomic number, respectively. At low energy (< 100 KeV), the first term is dominant, whereas at high energy (> 100 KeV) the second term is dominant.

Tomography uses the radiographic images (two dimensional projections) of the object obtained from different angles. After the detection of the transmitted X-rays at different sample rotation angles, one can reconstruct the full 3D image from the projection data. The simplest case for reconstructing this image from the projection data is when the beam of X-rays is parallel. In this situation, each point on the projection image contains the information of the attenuation inside the 3D object integrated along the path of the corresponding partial X-ray beam. In other words, for a parallel geometry it is possible to divide the problem of a three-dimensional reconstruction from two-dimensional projections into the serial reconstruction of two-dimensional object slices from one-dimensional projection lines. Reconstruction of the virtual slice through

the object is possible using an algorithm based on the filtered back projection algorithm. The two-dimensional Fourier transform of the object is defined as

$$F(u, v) = \int_{-\infty}^{\infty} \int_{-\infty}^{\infty} f(x, y) e^{-j2\pi(ux+vy)} dx dy \quad (\text{Equation A.5})$$

The projection along lines of constant x for a parallel projection is described as

$$P_{\theta=0}(x) = \int_{-\infty}^{\infty} f(x, y) dy \quad (\text{Equation A.6})$$

The Fourier transform of the projection defined in Equation A.6 is equal to the two-dimensional Fourier transform of the object along a line rotated by θ . This is the Fourier slice theorem, which is stated in Kak and Slaney¹⁴⁴: The Fourier transform of a parallel projection of an image $f(x, y)$ taken at angle θ gives a slice of the two-dimensional transform, $F(u, v)$, subtending an angle θ with the u -axis. In other words, the Fourier transforms of $P_{\theta}(t)$ gives the values of $F(u, v)$ along the line BB in Figure A.2

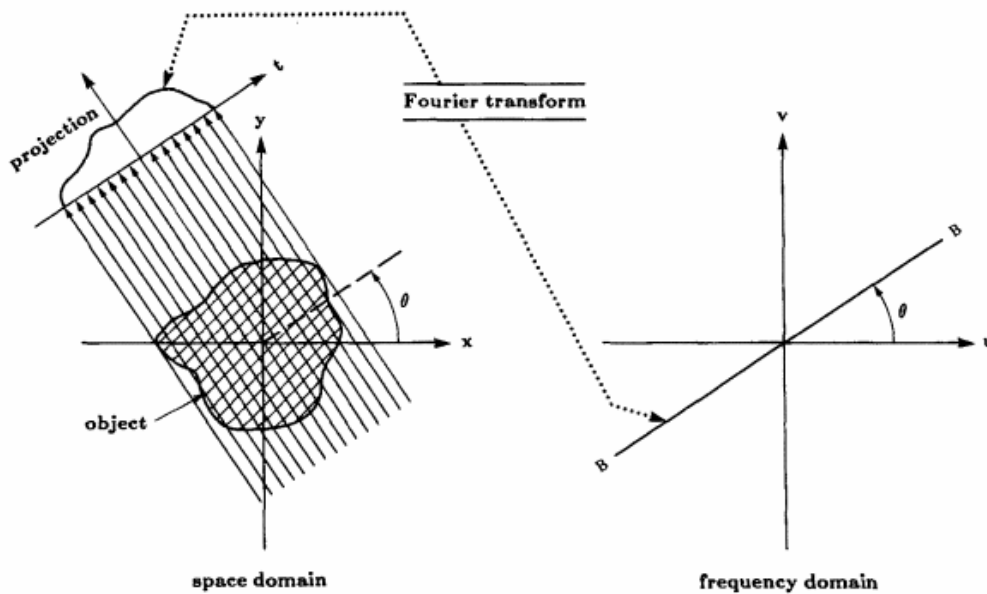


Figure A.2 The Fourier Slice Theorem relates the Fourier transform of a projection to the Fourier transform of the object along a radial line¹⁴⁴.

The filtered back-projection algorithm derived by using the Fourier Slice Theorem has been shown to be extremely accurate and amenable to fast implementation and used currently in almost all applications of straight ray tomography¹⁴⁴. Recalling the formula for the inverse Fourier transform, the object function, $f(x, y)$, can be expressed as

$$f(x, y) = \int_{-\infty}^{\infty} \int_{-\infty}^{\infty} F(u, v) e^{j2\pi(ux+vy)} du dv \quad (\text{Equation A.7})$$

This equation leads to the filtered back-projection equation:

$$f(x, y) = \int_0^{\pi} Q_{\theta}(x \cos \theta + y \sin \theta) d\theta \quad (\text{Equation A.8})$$

Where

$$Q_{\theta}(t) = \int_{-\infty}^{\infty} S_{\theta}(w) |w| e^{j2\pi wt} dw \quad (\text{Equation A.9})$$

$Q_{\theta}(w)$ is called a “filtered projection”, where the frequency response of the filter is given by $|w|$ towards the projection data transform $S_{\theta}(w)$. The resulting projections for different angles θ are then added to form the estimate $f(x, y)$, thus Equation A.8 represents the back-projection of each filtered projection in the reconstruction area. By increasing the number of projections from different views, this localisation becomes more and more defined. This is illustrated in Figure A.3.

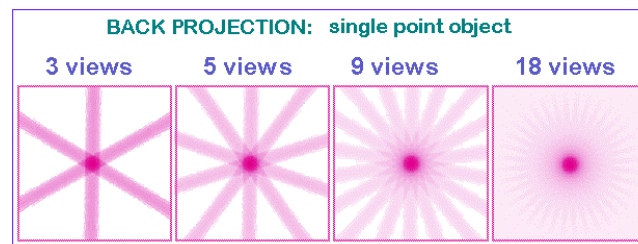


Figure A.3 The dependence of quality of the reconstruction image of a point object on the available projection data from different views¹⁴⁷.

A 3D visualisation is then obtained through the reconstruction of the whole consecutive two dimensional slices. The whole imaging and reconstructions processes using micro-CT is summarised in Figure A.4.

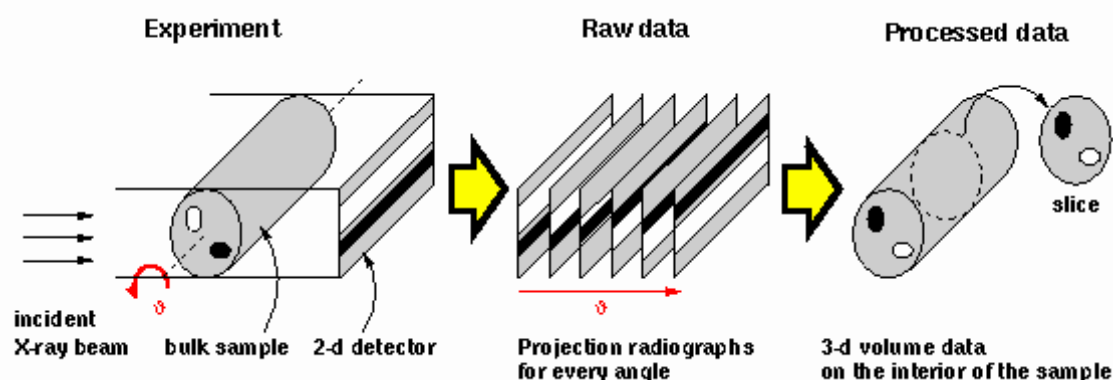


Figure A.4 Schematic illustration of the basic principle of non-destructive reconstruction 3D object with X-ray Microtomography.

Most X-ray sources in the laboratory scale are not able to generate parallel beams. In a real case, a point source which produces a cone X-ray beam in the object area is used. In a fan beam geometry, the reconstructed slices will show some distortions far from the optical axis. Thus, a 3D cone beam reconstruction algorithm (such as Feldkamp) is used to reduce the errors.

One of the first and most difficult artefacts one meets while working with μ -CT is beam hardening due to the polychromaticity of X-rays. There is no possibility to use monochromatic X-rays source for the tomography device in laboratory scale since the intensity is not brilliant enough to illuminate the sample in order to get reconstructed images with sufficient quality. The polychromatic X-rays consist of X-rays with a spectrum of different energies. Consequently, when the X-ray bundle passes the object, the lowest X-ray energies will be preferentially absorbed, leaving the rest portion of X-ray with higher energies, which are less likely to be attenuated. The beam hardening artefacts can be corrected by many methods but this will lead to either increased noises or lowered image quality. Besides, the beam hardening will be just lowered to some extents without being completely removed out of the system. A quantitative analysis of μ -CT data seems to be not possible by the presence of significant beam hardening. One can go to synchrotron tomography, where monochromatic X-ray can be easily produced, thus avoid the beam hardening artefacts. However, some other problems, such as beam stability and background noises may rise during the measurements.

The resolution values in micrometer decreases with increasing magnification and will saturate towards a resolution limit, which is the focal spot size of the source. The

resolution of the microtomograph is a function of the size of the focal spot of the source, the pixel size of the detector system, and the position of the object. Furthermore the resolution of the imaging system is found to be independent of the sample materials¹⁴⁸.

A.2 Scanning Electron Microscopy

Scanning electron microscopy (SEM) is the most widely used form of electron microscopy in the field of materials sciences¹⁴⁹. The large depth of focus, the excellent contrast and the straightforward preparation of solid specimens are the reasons for the considerable success and widespread use of scanning electron microscopy in the imaging of surfaces over the past decades¹⁵⁰. It has become an ideal tool to examine and interpret the microstructure of materials because of its high spatial resolution, high depth of field, and its analytical power¹⁴⁹. The SEM is much simpler and easier in the sample preparation in comparison to the transmission electron microscope (TEM) for which sample preparation is quite difficult since very thin specimen of several nm is required. Therefore, TEM is not used in this study due to its complexity, especially when being applied to a highly porous and heterogeneous systems such biological tissues.

The principle of scanning electron microscopy (SEM) is shown in Figure A.5. Electrons from a thermionic or field emission cathode are accelerated by a potential of 1-50 kV between cathode and anode. Using a set-up of a number of lenses, the electron beam is focused on to the sample in a single spot of cross section 1-10 nm carrying an electron probe current of $10^{-10} - 10^{-12}$ A¹⁵¹. A deflection coil system in front of the last lens scans the electron probe in a raster across the specimen and in synchronism with the electron beam of a separate cathode-ray tube (CRT). The intensity of the CRT is modulated by one of the signals recorded to form an image. The magnification can be increased simply by decreasing the scan-coil current. The bombarding of the sample with electrons leads to generation of X-rays and emission of secondary electrons or backscattered electrons. These effects can be used in probing the sample surface. Secondary electrons (SE) can be used to reveal surface topography, backscattered electrons (BSE) provide composition or orientation information, and emitted X-rays

may be collected for chemical analysis. Energy dispersive X-ray (EDX) analysis using electrons for excitation, and X-ray fluorescence (XRF) using X-rays for excitation, are both used in this study for chemical analysis.

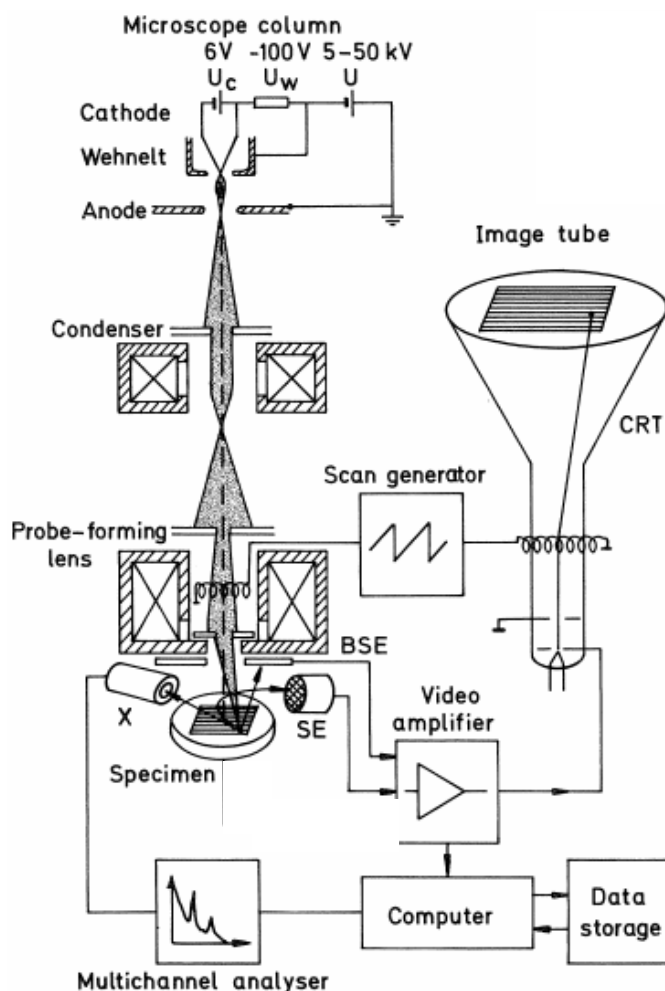


Figure A.5 Principle of the scanning electron microscope (SE= secondary electron, BSE= backscattered electrons, X= X-rays, CRT= Cathode-ray Tube ¹⁵¹).

Elastic and inelastic scattering are the elementary atomic interaction processes, though the final signal used for image formation is not a result of a single scattering processes but of the complete electron diffusion caused by the gradual loss of the electron energy and by lateral spreading due to multiple elastic large-angle scattering ¹⁵¹. Thus electrons have a finite penetration depth R of the order of $0.1-10 \mu\text{m}$ depending on electron energy and target density as the consequence of the gradual diminution of electron energy. However, the information depth and the lateral extension of the information volume that contributes to each of the possible signals depend on

where the corresponding interaction takes place. Figure A.6 shows the most important interaction processes and their information volumes. Secondary electron (SE) shows a peak at low energies with a most probable energy of 2-5 eV ($E_{SE} \leq 50$ eV). The broad spectrum of BSE between 50 eV and the primary electron energy is caused by the deceleration of electrons that have suffered multiple energy losses and undergone multiple scattering through large angles ($E_{BSE} > 50$ eV). Auger electrons (AE) are one of the by-products, along with X-rays, which result from the inner-shell ionizations of the atoms in the sample caused by primary beam electrons. Considering the fact that electrons can get scattered by any particle in their way, including air, electron microscopes must be operated in vacuum.

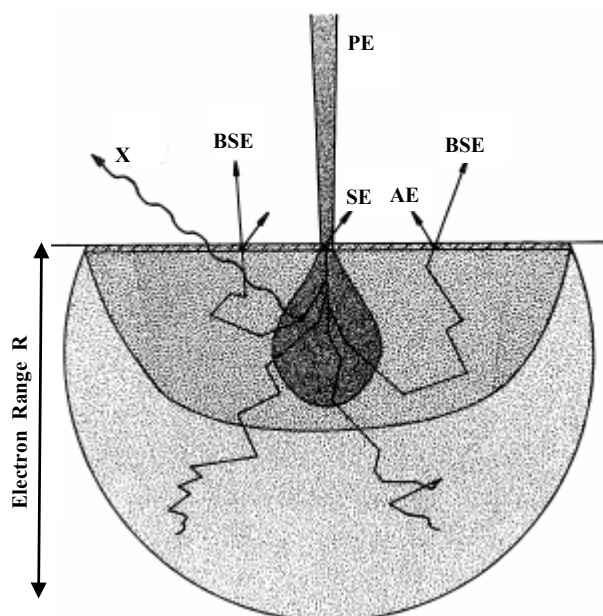


Figure A.6 Interactions of electron-specimen in an electron microscopy. Origin and information depth of secondary electron (SE), backscattered electron (BSE), Auger Electrons (AE) and X-ray quanta (X) in the diffusion cloud of electron range R for normal incidence of the primary electrons (PE) ¹⁵¹.

Secondary electrons (SE), which are loosely-bound outer-shell electrons from the atoms in the sample, are the primary electron signal collected for imaging in the SEM and to provide topographical information about the top surface of the sample. They can be collected easily by means of a positively biased collector grid placed on one side of specimen. Behind the collector grid, the secondary electrons are accelerated onto a scintillator and the light quanta generated are recorded by a photomultiplier. Such an Everhart-Thornley detector is generally used as an amplifier. The dependence of SE image on the tilt of angle of a surface element, the enhanced emission at edges and small area and the shadow contrast makes it useful for the imaging of the surface

topography. The secondary electrons are retarded by a positive bias and repelled by a negative bias of the specimen surface and are influenced by the electrostatic field between regions at different biases. These effects result in voltage contrast, negatively biased areas appearing bright and positively biased regions, dark¹⁵¹. This contrast leads to evaluation of the detailed morphology of the sample surface. Due to the low exit energy, the secondary electrons trajectories are also affected by the magnetic fields, creating magnetic contrast. Additionally, a typical backscattered electrons contrast is superimposed on every secondary electron micrograph since some fractions of the secondary electrons emitted is excited by the backscattered electrons.

Unlike secondary electrons, backscattered electrons (BSE) move on straight trajectories and are not affected by electrostatic collection fields, thus the detectors have to be mounted with a large solid angle of collection. Since the backscattered electrons emission also depends on the surface tilt, the surface topography can be imaged at lower magnifications with a better shadow effect than secondary electrons and at high magnification with a worse resolution, due to the larger information volume and exit area. The most important contrast is the dependence of the backscattering coefficient on the mean atomic number, \bar{Z} which allows phases with differences in \bar{Z} to be recognised. In addition, the backscattering coefficient also depends on the relative orientation of the incident electron beam and the lattice planes.

Many SEMs are equipped with an energy-dispersive lithium-drifted silicon detector, which allows characteristic X-ray lines to be recorded with a resolution $\Delta E \approx 150\text{-}200$ eV of the X-ray quantum energy¹⁵¹. Energy-dispersive spectrometers are advantageous since all quantum energies within 1-20 keV can be recorded simultaneously and the spectrum, which contains information about composition of the internal constituents of the area, is displayed directly by means of a multichannel analyser. The quantitative analysis can be done by comparing the number of counts from an element in the specimen with the number of counts from a pure-element standard. However, the analysis is valid only if the specimen is flat and homogeneous within the diameter of the electron diffusion cloud. Thus, quantitative analysis of inhomogeneous specimens, such as biological tissues becomes more problematic. Nevertheless, energy dispersive X-ray (EDX) analysis is one the most widely-used and most powerful of the analytical capabilities available in electron microscopy.

As the sample is bombarded with electrons, charge is built on the surface and if the sample is non-conducting it is not dissipated. As a result, charging effect will occur and the sample appears bright everywhere. To stop the charge from building up, the sample needs to be conducting. For these reasons the samples are generally coated with a very thin layer of metal such as gold or palladium or subjected to carbon sputtering prior to analysis. Furthermore, the emergence of Environmental SEM (ESEM) in the mid eighties has opened wider SEM investigations that were previously impossible¹⁵². This is because ESEM removes the high vacuum constraint on the sample environment while still retaining all of the performance advantages of a conventional SEM. The investigation of wet, oily, dirty, non-conductive samples in their natural state without modification or preparation becomes possible. The ESEM offers high resolution secondary electron imaging in a gaseous environment of practically any composition, at pressures as high as 50 Torr, and temperatures as high as 1500°C¹⁵².

A.3 Vibrational Spectroscopy

Vibrational spectroscopy is a powerful tool to investigate materials at the molecular levels. In this study, chemical analysis is performed by using the vibration spectra as “fingerprint”. Other information such symmetry of molecules, the nature of bonding and interactions of atoms within the molecules may also be obtained. Vibrational spectroscopy is useful for qualitative as well as quantitative investigations¹⁵³. Two important methods are infrared (IR) and Raman spectroscopy, which are complementary to each other. Vibrations which modulate the molecular dipole moment are visible in the infrared spectrum while those which modulate the polarizability appear in the Raman spectrum.

The simplest model of an atom bound in a molecule is given as a mass m bound to neighbours a weightless spring. The force F that is necessary to move the atom by a certain distance x from an equilibrium position is proportional to the force constant f , a measure of the strength of bond by Hooke’s law given in Equation A.10.

$$F = -f \cdot x \quad \text{(Equation A.10)}$$

By Newton's law
$$F = m \frac{d^2 x}{dt^2} \quad (\text{Equation A.11})$$

$$\Rightarrow m \frac{d^2 x}{dt^2} = -f \cdot x \quad (\text{Equation A.12})$$

One of solutions of this second order differential equation is given as

$$x = x_0 \cdot \cos(2\pi\nu t + \varphi) \quad (\text{Equation A.13})$$

describing the motion of the atom as a harmonic oscillation. Here ν is the vibrational frequency and φ the phase angle. The second derivative of x by the time is found to be:

$$\frac{d^2 x}{dt^2} = -4\pi^2 \nu^2 x_0 \cos(2\pi\nu t + \varphi) = -4\pi^2 \nu^2 x \quad (\text{Equation A.14})$$

Combining Equation A.17 with Equation A.15 yields

$$4\pi^2 \nu^2 m = f \quad \text{or} \quad \nu = \frac{1}{2\pi} \sqrt{\frac{f}{m}} \quad (\text{Equation A.15})$$

If we consider a diatomic molecule, the mass m is called reduced mass of diatomic molecule with the masses m_1 and m_2 :

$$\frac{1}{m} = \frac{1}{m_1} + \frac{1}{m_2} \quad (\text{Equation A.16})$$

Thus the frequency of vibration of a diatomic molecule is given as

$$\nu = \frac{1}{2\pi} \sqrt{f \left(\frac{1}{m_1} + \frac{1}{m_2} \right)} \quad (\text{Equation A.17})$$

A diatomic molecule is said to have one vibrational degree of freedom as it can have only one mode of vibration. Similarly, a molecule containing n atoms will have $3n-6$ degree of vibrational modes and a molecule can be excited from one vibrational energy level to the other by getting radiation of certain frequency. Thus every molecule shows characteristic vibrational spectra depending on the mode of vibration and the frequency of radiation used for excitation. In general, the vibrational frequency is given in wave number units $\tilde{\nu}$ (waves per unit length), which is reciprocal to the wavelength λ .

A.3.1 Confocal Raman Microscopy

Confocal Raman microscopy is simply combining Raman spectroscopy with non-destructive and high-resolution imaging methods like confocal microscopy. This technique provides chemical and structural information in situ without any staining or complicated sample preparation, thus allowing to understand structure-function relationships of plant cells for instance, to learn from nature¹⁵⁴.

The Raman effect is most simply described as the inelastic scattering of light by matter. The incident light causes the molecules to vibrate, and the result is an energy shift between the excitation and the Raman-scattered photon. The energy shift is a function of the mass of the involved atoms and the binding strength and coordination, so every chemical species shows its own, distinct fingerprint¹⁵⁵. When light is scattered by a molecule there can be one of three outcomes (Figure A.7):

1. Elastic (Rayleigh) scattering, where there is no net energy loss or gain to the incident light beam.
2. Inelastic (Stokes) scattering, where the light is scattered to lower energy and frequency corresponding to the excitation of a molecular vibration.
3. Inelastic (anti-Stokes) scattering, where the light is scattered to higher energy and frequency corresponding to the annihilation of a molecular vibration.

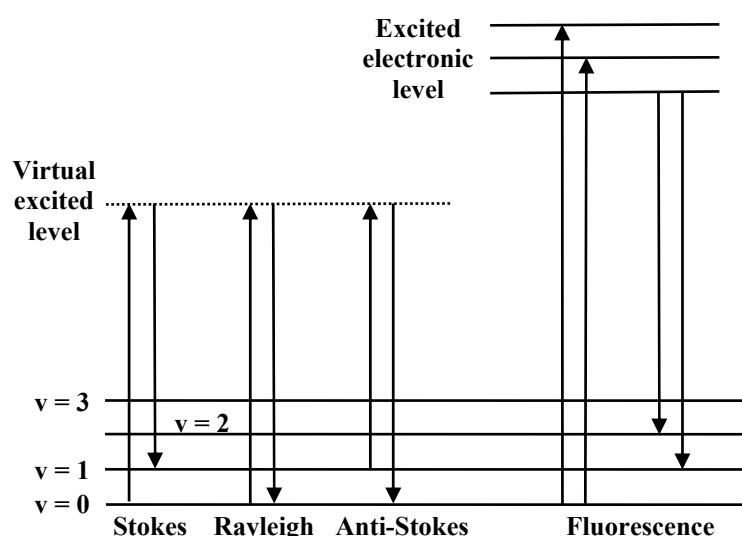


Figure A.7 Schematic representation of various modes of scattering processes.

Elastic (Rayleigh) scattering is the dominant process, whereas inelastic (Raman) scattering is inherently a very weak process where only one in every 10^6 - 10^8 photons shows the Raman effect¹⁵⁶. Besides this disadvantage, fluorescence is also likely to occur in Raman spectroscopy. This fluorescence is caused by the excitation of atoms in a material during the sample irradiation, thus electromagnetic radiation in the form of visible light is emitted. Fluorescence is not desirable since it can exceed the quantum yield of the Raman effect by a factor of about one million¹⁵³ and obscure the Raman spectra. The term fluorescence here should not be interchanged with the X-ray fluorescence which is intentionally generated and widely used for the chemical analysis of trace elements within a material and will be discussed in the following section. However, Raman spectroscopy shows its superiority on FTIR due to its little interference from water and its better spatial resolution than that achievable by IR spectroscopy, making it advantageous for the study of many biological specimens¹⁵⁷.

On many modern Raman spectrometers, a microscope is already an integral part of the spectrometer. The microscope has many advantages enabling to look at extremely small samples and detect very small amounts of materials despite Raman scattering is weak. The theoretical spatial resolution is $\sim 1 \mu\text{m}$ ¹⁵⁶. Raman microscopy is very useful in the analysis of inhomogeneous biological samples, since the imaging of specific chemical constituents with high resolution becomes possible. The application of confocal arrangement allows segmenting a specimen along the optical axis and a depth profile or a 3D image can be generated. Additionally, in this setup, light from the sample is detected through the pinhole placed in the back focal plane of the microscope. Thus, the out-of-focus Raman light will be excluded and fluorescence background is greatly reduced.

As the Raman effect is very weak, a medium-power laser for excitation and a sensitive detector to obtain a good signal-to-noise ratio within a reasonably short time are required. The schematic operating system of confocal Raman microscopy is shown in Figure A.8. The laser beam is delivered through a single-mode optical fiber and then through a series of mirrors and the objective on to the sample. The reflected (Raman scattered) light is collected with the same objective and is focused into a multi-mode fiber, which directs the beam to the spectrometer equipped with a CCD camera and a photon counting APD. Holographic notch filters are used as beam splitter and to

selectively filter out the Rayleigh scattered light from the scattered radiation. During the scan, the data acquisition electronics creates a trigger signal for every image pixel. The CCD camera is read out at every pixel trigger and the resulting spectrum is stored in the computer.

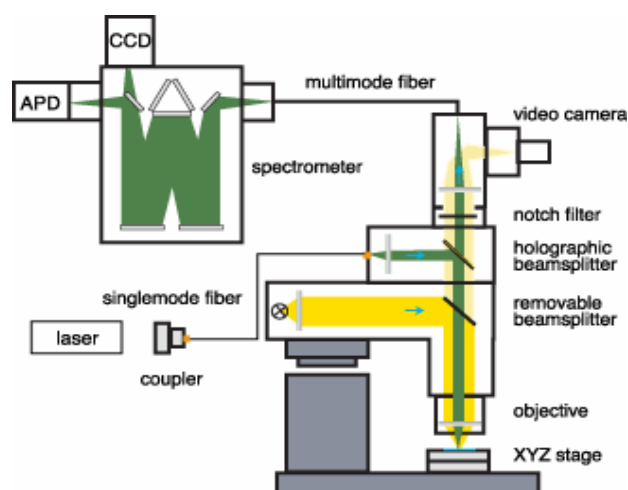


Figure A.8 Schematic representation of a confocal Raman microscope system¹⁵⁸.

A.3.2 FTIR Spectroscopy

The advantages of using infrared spectroscopy for the study of biological specimens are evident. IR spectroscopy has higher intensity, a larger spot size and fast acquisition times since a broadband light source is used in contrast to Raman which uses a monochromatic beam. Thus, a higher signal-to-noise ratio is obtained and it is very useful for studies in which spatial averaging is acceptable or desirable. IR spectroscopy also has the advantage that using it on biological specimens entails no problems with fluorescence¹⁵⁷. However, the large background absorption of water has become a major problem of infrared spectroscopy.

The IR regions are subdivided into three, namely near-IR, mid-IR, and far-IR, of which the mid-IR region of radiation with the vibrational frequency range of 4000 cm^{-1} to 400 cm^{-1} corresponds to the changes in fundamental vibrational levels of most of the molecules. Thus, the radiation in this region is generally used to probe the vibrational

behaviour of the sample molecules and to obtain the characteristic fingerprint of certain chemical substances.

IR radiation of a certain vibrational frequency is observed only if a change in the dipole moment of the molecule occurs. The vibrations accompanying dipole moment changes are thus termed as *IR active*, whereas those without any changes in dipole moment are *IR inactive*. Infrared spectra are usually recorded by measuring the transmittance of light quanta with a continuous distribution of the sample. The fundamental equation which governs the relation between the intensities of the incident and the transmitted radiation (I_0 and I) and the concentration c is referred to as the Lambert-Beer law, which is basically the same principle applied for X-rays absorption (see Eq. A.2), expressed as

$$\log \frac{I_0}{I} = \log \frac{1}{\tau} = A = a.c.d \quad (\text{Equation A.18})$$

I = intensity of transmitted radiation

I_0 = initial intensity

τ = transmittance

A = absorbance

a = absorption coefficient

c = concentration of the sample

d = cell thickness

Fourier Transform Infrared Spectroscopy (FTIR), based on a Michelson Interferometer has replaced the conventional dispersive IR spectroscopy because it offer two advantages¹⁵³: 1) multiplex and 2) Jaquinot advantage. The multiplex advantage allows a drastic reduction of the measuring time, whereas the Jaquinot advantage is related to the increment of light intensity, which can lead to a quadratic increase in the signal-to-noise ratio. FTIR is very reliable in detecting small absorption changes with a time resolution of a few nanoseconds.

In principle, an FTIR instrument consists of a Michelson interferometric arrangement as is shown in Figure A.9. A parallel, polychromatic beam of radiation from a light source G (globar) is directed to a beam splitter BS, made from an infrared transparent material, such as KBr. The beam splitter reflects approximately half of the

light to a mirror, known as the fixed mirror FM, which in turn reflects the light back to the beam splitter. The rest of the light passes through to a movable mirror MM, moving continuously, at a known velocity, back and forth along the direction of the incoming light. Upon reflection from the moving mirror, radiation is then directed back to the beam splitter. At the beam splitter some of the light that has been reflected from the fixed mirror combines with light reflected from the moving mirror and is directed towards the sample. After passing through the sample, the radiation is focused onto the detector. The very sensitive MCT detectors generally operate best in the mid-IR region. The complex pattern of overlaid sinusoidal waves of light (in the time domain) is known as an interferogram, which is a function of the intensity versus the distance x of the movable mirror. The interferogram can be converted back to the original frequency distribution (spectrum) by means of a discrete Fourier transform (DFT), which can be done very rapidly using a computer.

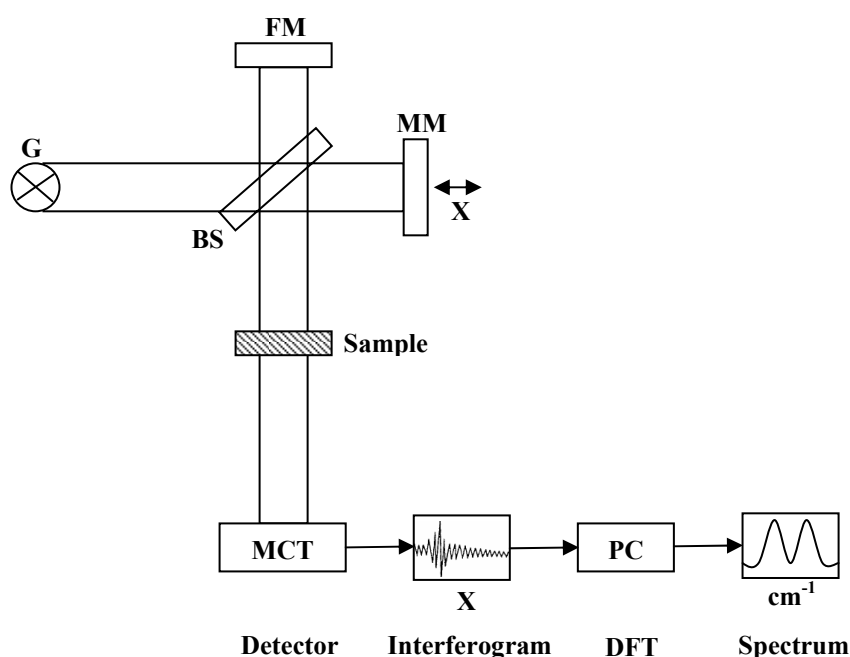


Figure A.9 Schematic representation of an FTIR apparatus ¹⁵³.

Attenuation Total Reflection (ATR) FTIR is a spectrophotometric analytical technique using optical interface energy reflection of two media having different refractive indices. Reflection spectroscopy technique has advantages in many aspects,

such as easy sample preparation, study of complete optical properties, area selectivity and sensitivity for the study of surface or monolayer on a substrate¹⁵³.

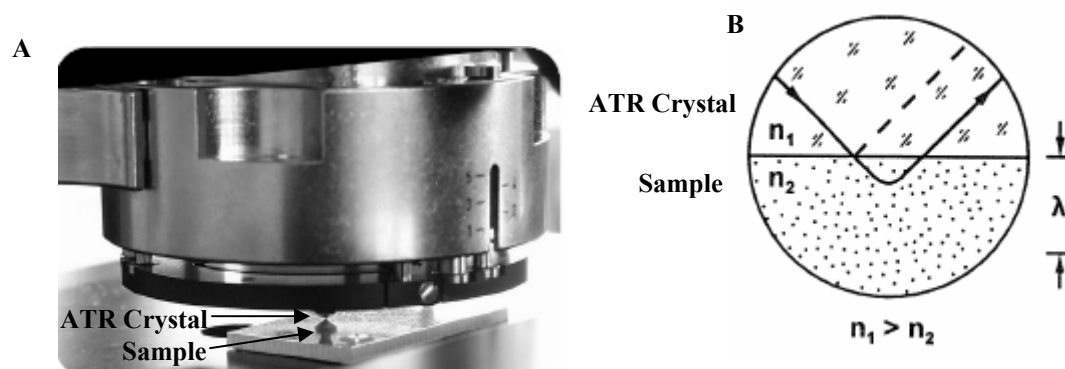


Figure A.10 Attenuated Total Reflection. (A) ATR crystal in contact with the sample surface during the measurement; (B) Schematic of the internal reflection in FTIR-ATR mode, n_1 and n_2 are the refractive index of medium 1 (ATR crystal) and medium 2 (sample), respectively.

The infrared light is passed through the ATR crystal in such a way and reflected internally at the interface of the sample, thus this technique is also referred to as internal reflection (Figure A.12). This reflection will then form the evanescent wave which travels across the sample, typically by a few microns, before being collected to the detector as it exits the crystal. In case of a solid sample, it should be firmly clamped since it pressed into direct contact with the crystal during the measurement. The penetration depth, d_p for the evanescent field can be calculated using the following equation:

$$d_p = \lambda_1 / \left[2\pi \left(\sin^2 \varphi_1 - n_2^2 / n_1^2 \right)^{1/2} \right] \quad (\text{Equation A.19})$$

Where $\lambda_1 = \lambda / n_1$ denotes the effective wavelength in the denser medium (medium 1) or ATR crystal, φ_1 is the incident beam angle in medium 1, n_1 and n_2 are the refractive index of medium 1 and 2, respectively. The ATR crystal must be infrared transparent and of high refractive index¹⁵³. Typical materials for ATR crystals include germanium, KRS-5 and zinc selenide, while silicon is ideal for use in the Far-IR region of the electromagnetic spectrum. Diamond is an ideal material for ATR, particularly when studying very hard solids, but it is less widely used due to its high cost.

A.4 X-ray Fluorescence (XRF)

X-rays interact in different ways with matter. The chief effects associated with the passage of X-rays through matter are summarised schematically in Figure A.11. The incident X-rays are assumed to be of high enough energy, i.e., of short enough wavelength, to cause the emission of photoelectrons and characteristic fluorescent radiation¹⁴³.

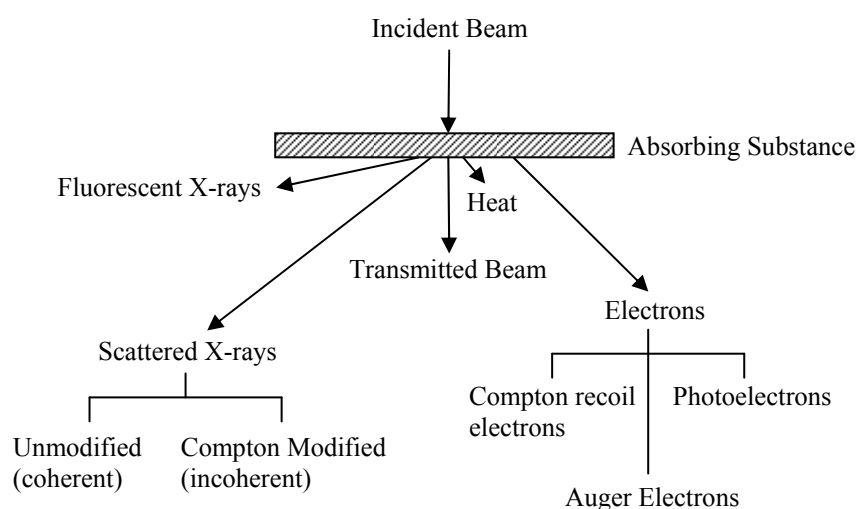


Figure A.11 Effects produced by the passage of X-rays through matter¹⁴³.

X-ray fluorescence spectrometry has become a powerful tool for the elemental analysis and its use becomes more increasing in the field of materials characterisation in terms of chemical compositions, particularly in the investigation of metals, glass, ceramics and building materials, and for research in geochemistry, forensic science and archeology.

Fluorescence occurs when the primary X-ray photons are energetic enough to create core electron vacancies in the specimen, which leads in turn to the generation of the secondary radiation (fluorescence) as the outer electrons fill the electron vacancies of the inner shell. This radiation is characteristic of the elements making up the specimen, thus the technique is useful for elemental identification and quantifications of elemental concentrations estimated from the characteristic line intensities. This technique has the same principle as SEM coupled with Energy dispersive X-ray (EDX) analysis. They just differ in the excitation source of the inner electrons, i.e. the X-ray fluorescence use X-ray as the excitations sources rather than electron excitation.

Electron excited X-ray fluorescence is relatively inefficient since about 99% of the electron energy is converted to heat energy. On the other hand, the use of X-rays to excite characteristic X-ray radiation avoids the problem of the heating of the specimen since X-ray photons can be produced inside a sealed X-ray tube under high vacuum and efficient cooling conditions, which means the specimen itself need not be subject to heat dissipation problems or the high vacuum requirements of the electron beam system¹⁴⁹. XRF has rather poor sensitivity for the very low atomic number elements ($Z < 9$), for instance the detection limits for carbon ($Z = 6$) and Oxygen ($Z = 8$) are typically of the order of 3-5%¹⁴⁹. However, X-ray fluorescence techniques offers good overall performance characteristics, particularly in the high speed, accuracy, and versatility.

Laboratory based X-ray fluorescence spectrometry typically uses a polychromatic beam of short wavelength X-ray radiation to excite longer wavelength characteristic lines from the sample for analysis, but modern X-ray spectrometers use either the diffracting power of a single crystal to isolate narrow wavelength (*wavelength dispersive spectrometry/ WDX*) and, or a proportional detector to isolate narrow energy bands, from the polychromatic radiation (including characteristic radiation) excited in the sample (*energy dispersive spectrometry/ EDX*). There are also special spectrometers category, including total reflection spectrometers (TRXRF), synchrotron source spectrometers (SSXRF), and proton induced X-ray emission spectrometers (PIXE)¹⁴⁹.

The schematic arrangements of these two types' spectrometers can be seen in Figure A.12 and Figure A.13, respectively. In EDX spectrometer, the emitted fluorescent X-rays from the sample are directed typically to a Si(Li) detector, which is a proportional detector of high intrinsic resolution and a continuous distribution of pulses are produced. These pulses are voltages which are proportional to the incoming photon energies and then processed by a multichannel analyser (MCA). The output is a digital spectrum that can be processed to obtain analytical data. In WDX analysis, the emitted fluorescent X-rays are directed at first into a diffraction grating monochromator, which is usually a single crystal. A single X-ray wavelength can be selected by varying the angle of the incidence according to the Bragg's law ($n\lambda = 2.d.\sin\theta$), which will be further discussed in the next section. The collimators or slits are generally used to determine the width of the diffracted lines.

The WDX system is roughly one to two orders of magnitude more sensitive than the EDX system. However, the EDX spectrometer measures all elements within its range at essentially the same time, whereas the WDX spectrometer identifies only those elements for which it is programmed. To this extent, the energy dispersive system is more useful in recognizing unexpected elements ¹⁴⁹.

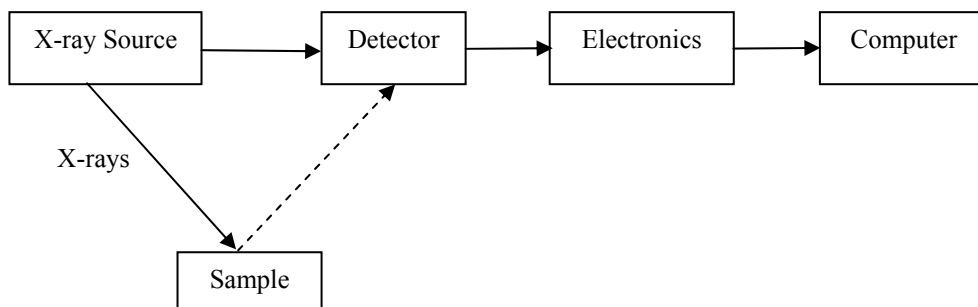


Figure A.12 Schematic arrangement of EDX Spectrometer

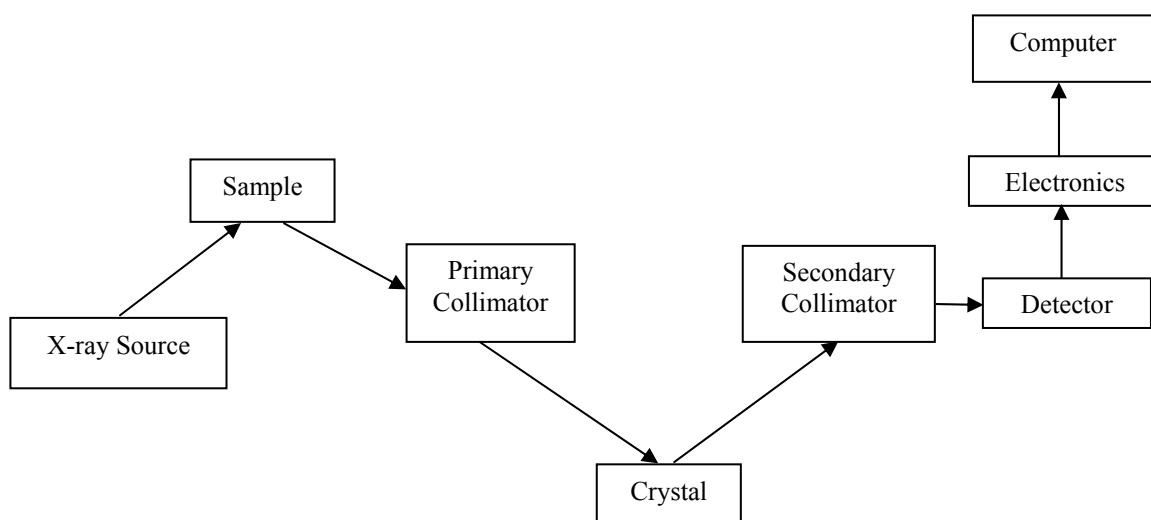


Figure A.13 Schematic arrangement of WDX Spectrometer

A.5 X-ray Scattering

X-ray scattering is very useful for the material characterisation down to the nanometer scale and has become an indispensable tool both in research and industrial fields. It is a high-tech, non-destructive technique for analysing a wide range of materials, including fluids, metals, minerals, polymers, catalysts, plastics, pharmaceuticals, thin-film coating, ceramics, and semiconductor. Structure properties such as crystal structure, crystallinity, texture, particle size, particle shape, orientation as well as porosity and pore structure can be obtained. X-ray scattering is also very powerful in investigating biological tissues which have a hierarchical structure since it requires only a minimum of sample preparations and produces structural parameters averaged over a large irradiated sample volume. However, one needs to create models for the evaluation of the scattering patterns to extract the indirect information from the reciprocal space.

An electron in the path of X-rays is excited to periodic vibrations and it becomes a source of electromagnetic waves of the same frequency and wavelength. From this interaction, a new spherical wave front of X-rays arises, with the electron as its origin, deriving its energy from the impinging beam. This means the electron scatters the original beam¹⁵⁹. In an atom, the scattered waves from the several electrons combine and the resulting scattering intensity is dependent on the atomic number and direction. X-rays are scattered mainly by the loosely bound outer electrons of an atom¹⁴⁹. Scattering of X-rays may be coherent or incoherent (Figure A.11). Coherently scattered photons may undergo subsequent mutual interference, leading in turn to the generation of X-ray diffraction. The X-ray scattering phenomenon can be simply described by Figure A.14. If the wavelength of the scattered wave is the same as that of the incident one, the scattering is elastic¹⁶⁰. This elastic scattering is the main process that is exploited in investigations of the structure of materials.

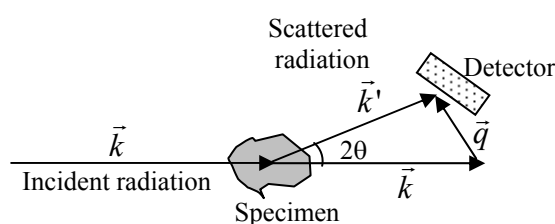


Figure A.14 The elastic X-ray scattering phenomenon.

In Figure A.14, \vec{k} and \vec{k}' are the incident X-ray wave vector and the wave vector of X-rays scattered at an scattering angle 2θ , respectively. The scattering vector \vec{q} defined as $\vec{q} = \vec{k}' - \vec{k}$ determines the geometry of the experiment. In case of elastic scattering, $k' = k$, thus $q = 2k \sin \theta = (4\pi / \lambda) \sin \theta$.

The measured scattering intensity $I(\vec{q})$ is proportional to the square of the scattering amplitude which is related to the square of the Fourier transform of the scattering length density distribution. Scattering length density denotes the variation in the inhomogeneities of the electron density.

$$I(\vec{q}) = K \frac{d\Sigma}{d\Omega}(\vec{q}) = \frac{K}{V} \left| \int_V \rho(\vec{r}) \exp(i\vec{q} \cdot \vec{r}) d^3r \right|^2 \quad (\text{Equation A.20})$$

Where $\frac{d\Sigma}{d\Omega}(\vec{q})$ corresponds to the macroscopic differential scattering cross-section of the sample, V is the sample volume, K is an instrumental constant and ρ is the scattering length density.

A.5.1 Wide-angle X-ray Scattering (WAXS)

Wide angle X-ray scattering is most powerful when applied to crystalline materials, but it can yield fundamental and important data when applied to liquids and amorphous solids¹⁵⁹. Crystalline materials, such as metals, rocks and soil, concrete, wood, and textile fibers consist of a periodic arrangement of repeating units of atoms in space. On the other hand, amorphous solids, such as glasses, gels, and opal show the absence of the long-range order. There is no translational periodicity, however, a degree of short-range order remains. This fundamental difference can be seen in Figure A.15. An elementary knowledge in crystallography is essentially required for an understanding the simple geometry of X-ray diffraction by crystals.

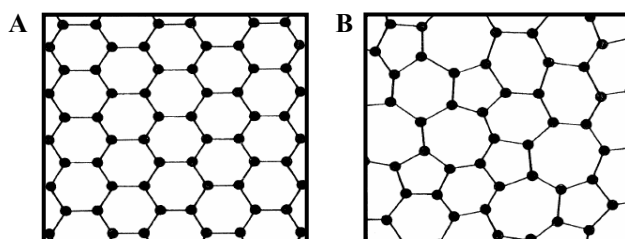


Figure A.15 Schematic sketches of the atomic arrangement in: A. Crystalline solid, B. Amorphous solid¹⁶¹.

A.5.1.1 Crystal Systems and Reciprocal Lattice

A crystal is represented by a lattice, that is, a three-dimensional array of points in a space (lattice points). The six scalar lattice parameters (the lengths of the three lattice translation vectors a , b , c and the three inter-axial angles α , β , γ) define the unit cell, which is the smallest portion or *building block* making up the whole crystal structure by translation as depicted in Figure A.16.

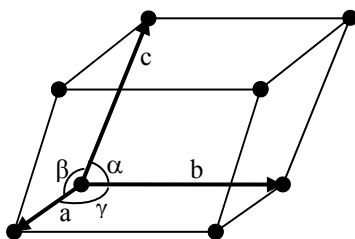


Figure A.16 Schematic of a unit cell.

There are seven crystal systems based on the variations of the length and orientation of the vectors as listed in Table A.1. Many elements crystallize in a cubic or hexagonal structure. For this reason, and also because of their high symmetry, the cubic and hexagonal coordinate systems are particularly important¹⁶².

Table A.1 Seven Crystal Systems.

Axial Lengths	Angles	System
$a = b = c$	$\alpha = \beta = \gamma = 90^\circ$	cubic
$a = b \neq c$	$\alpha = \beta = \gamma = 90^\circ$	tetragonal
$a \neq b \neq c$	$\alpha = \beta = \gamma = 90^\circ$	orthorhombic
$a = b = c$	$\alpha = \beta = \gamma \neq 90^\circ$	rhombohedral/ trigonal
$a = b \neq c$	$\alpha = \beta = 90^\circ, \gamma = 120^\circ$	hexagonal
$a \neq b \neq c$	$\alpha = \gamma = 90^\circ \neq \beta$	monoclinic
$a \neq b \neq c$	$\alpha \neq \beta \neq \gamma \neq 90^\circ$	triclinic

The orientation of a plane of lattice points is denoted by Miller indices (hkl), which are defined as the reciprocals of the fractional intercepts which the plane makes with the crystallographic axis. Planes whose indices are negative are parallel and lie on opposite sides of the origin. The spacing between two crystallographic planes hkl is denoted by d_{hkl} . The use of a reciprocal lattice is more convenient to visualise the crystal planes, their slopes and their spacing in much easier way¹⁵⁹, and the reciprocal lattice

representation of a crystal is a powerful tool for understanding diffraction¹⁴³. A reciprocal lattice vector \vec{b}_i (i.e. a lattice vector in *reciprocal space*) can be defined for every direct space lattice vector \vec{a}_i in *real space* by

$$\begin{aligned}\vec{b}_1 &= 2\pi \frac{\vec{a}_2 \times \vec{a}_3}{\vec{a}_1 \cdot (\vec{a}_2 \times \vec{a}_3)} \\ \vec{b}_2 &= 2\pi \frac{\vec{a}_3 \times \vec{a}_1}{\vec{a}_2 \cdot (\vec{a}_3 \times \vec{a}_1)} \\ \vec{b}_3 &= 2\pi \frac{\vec{a}_1 \times \vec{a}_2}{\vec{a}_3 \cdot (\vec{a}_1 \times \vec{a}_2)}\end{aligned}\quad (\text{Equation A.21})$$

The length H_{hkl} of a reciprocal lattice vector $\vec{H}_{hkl} = h\vec{b}_1 + k\vec{b}_2 + l\vec{b}_3$ equals the reciprocal of the periodicity of (hkl), i.e., $H_{hkl} = 2\pi/d_{hkl}$ ¹⁴³. The length H_{hkl} is equal to the modulus of scattering vector, q . Furthermore, the intensity scattered from atoms on a regular lattice is different from zero if and only if the scattering vector, \vec{q} coincides with a reciprocal lattice vector \vec{H} .

$$\vec{q} = \vec{H} \quad (\text{Equation A.22})$$

This is the condition for the observation of diffraction from a crystalline lattice which satisfies also Bragg's law discussed in the following section.

A.5.1.2 Bragg's Law

Laue's hypothesis¹⁴³ stated that "if crystals were composed of regularly spaced atoms which might act as scattering centres for X-rays and if X-rays were electromagnetic waves of wavelength about equal to the interatomic distance in crystals, then it should be possible to diffract X-rays by means of crystals", was successfully analysed by W.L. Bragg. The diffraction maxima occur only during the constructive interferences when the incident beam encounters the lattices at certain angles and the phase shift is proportional to 2π according to the Bragg's law:

$$n \lambda = 2 d_{hkl} \sin \theta \quad (\text{Equation A.23})$$

where n is an integer (the order of reflection or diffraction), λ is the wavelength, d_{hkl} is the interplanar spacing.

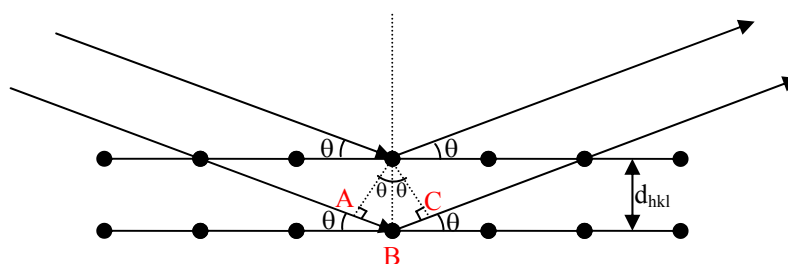


Figure A.17 Diffraction of X-rays by a crystal. $AB=BC= d_{hkl} \sin \theta$. For constructive interference ($AB+BC$), $2 d_{hkl} \sin \theta = n \lambda$.

A.5.1.3 Powder Diffraction

In the powder method, the solid to be examined is crushed into powder of many crystals so that the individual crystals are randomly oriented with respect to the incident monochromatic beam. Thus, every set of lattice planes will be capable of diffraction. The mass of powder is equivalent, in fact, to a single crystal rotated, not about one axis, but about all possible axes¹⁴³. The presence of a large number of crystal particles having all possible orientations is equivalent to the sample rotation, since among these particles there will be a certain fraction whose (hkl) planes make the correct Bragg angle with the incident beam and which at the same time lie in all possible rotational positions about the axis of the incident beam. Therefore the hkl reflection from a stationary mass of powder has the form of a conical sheet of diffracted radiation, and a separate cone is formed for each set of differently spaced lattice planes. The common powder diffraction method, i.e. Hull/Debye-Scherrer method is depicted in Figure A.18. The powder patterns (d-spacing pattern) contain the crystallographic information of certain chemical species present in the solid which is a “finger-print” for that solid.

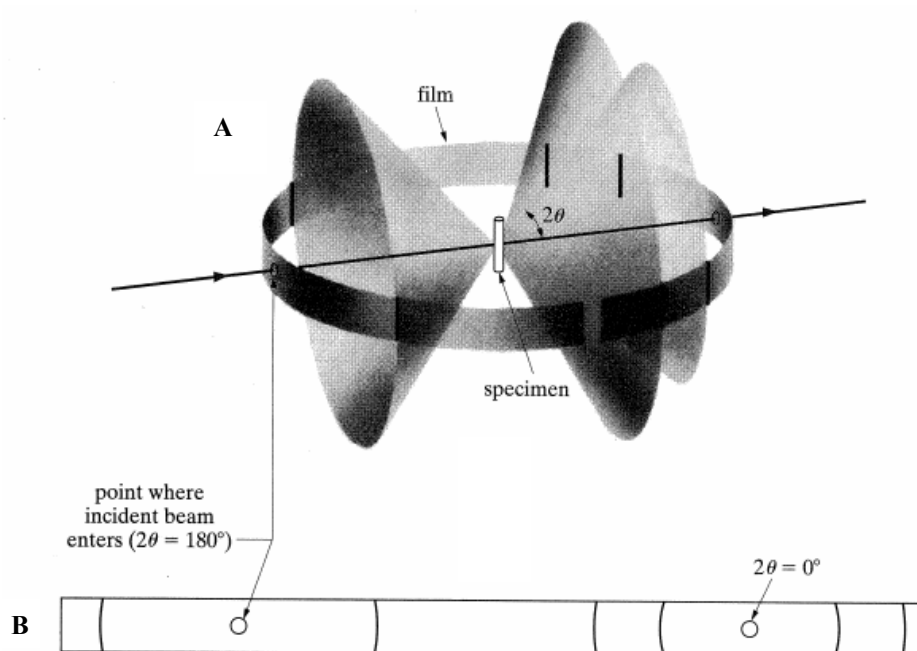


Figure A.18 Hull/Debye-Scherrer powder method: (A) relation of film to specimen and incident beam; (B) appearance of film when laid flat¹⁴³.

A.5.1.4 Crystallite Size

The crystallite size of the solid particle can be calculated using the Scherrer equation:

$$L = K \frac{2\pi}{w} \quad (\text{Equation A.24})$$

where w is the width of a certain diffraction peak in q -space, K is a constant depending on the shape and dimensionality of the crystallite and L is the crystallite size (Scherrer size). It is seen that the crystallite size is inversely proportional to the peak width. This highlights an important property of direct and reciprocal spaces. If a feature's dimension along a certain direct space direction is large, the feature's size along the corresponding direction in reciprocal space is small, and vice versa.

A.5.2 Small-angle X-ray Scattering (SAXS)

Small-angle scattering of X-rays allows the study of structures with sizes from ≈ 1 nm to ≈ 100 nm, and the applications range from biology to materials science ¹⁶³. This technique has been widely applied for the structural analysis of materials in two different ways. The first is crystallographic *small-angle diffraction*, which is used to study the periodic arrangement of atoms, molecules, or groups of molecules with large unit cells. The second is associated with diffuse small-angle scattering giving information on size, shape, and orientation of inhomogeneities (like precipitates, pores, macromolecules in solution, etc.) ¹⁶³. In small-angle scattering experiments, the two-phase model is frequently used as an approximation ^{114, 164}. The sample is considered to be made of two phases (a matrix and inclusions) with homogeneous, average scattering length densities (at the q scale investigated) and separated by sharp interfaces. In this case, the diffuse intensity at small angles can be written as:

$$I(\vec{q}) = I_0 \underbrace{(\rho_\alpha - \rho_\beta)^2}_{\substack{(\Delta\rho)^2 \\ \text{Scattering} \\ \text{contrast}}} \left| \underbrace{\int_V \Xi(\vec{r}) e^{i\vec{q}\cdot\vec{r}} d^3r}_{\substack{\text{Structure} \\ \text{function}}} \right|^2 \quad (\text{Equation A.25})$$

where I_0 is instrument constant, ρ is scattering length densities, $\Xi(\vec{r}) = 0$ for α phase and 1 for β phase or vice versa (Babinet's principle).

A.5.2.1 Porod's Law

Porod's law is generally valid for two-phase systems with sharp interfaces. The spherically averaged intensity is:

$$I_s(q) = \frac{I_0 2\pi \Delta\rho^2 \sigma}{q^4} = \frac{P}{q^4}, \quad qR \gg 1 \quad (\text{Equation A.26})$$

where σ is the total interface per unit volume, P is Porod's constant which is proportional to the total interfaces between the two phases. Thus Porod's analysis is quite useful for the analysis of micro- and mesoporous materials.

A.5.2.2 Integrated Intensity and Porod Length

For two-phase systems with sharp interfaces, the integrated intensity (“invariant”) can be written as:

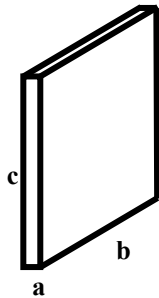
$$\tilde{I} = I_0 \int_0^{\infty} I_S(q) q^2 dq = I_0 2\pi^2 \Delta\rho^2 \phi(1-\phi) \quad (\text{Equation A.27})$$

where ϕ is volume fraction. By the combination with Porod’s law (Equation A.26), the Porod length (average chord-length) can be obtained as follows:

$$T = \frac{4 \tilde{I}}{\pi P} = 4 \frac{\phi(1-\phi)}{\sigma} \quad (\text{Equation A.28})$$

This T parameter has been introduced by Porod¹⁶⁵ and can be related to the mean chord lengths of the inclusions $l_I = 4\phi/\sigma$ and of the matrix $l_M = 4(1-\phi)/\sigma$ by $1/T = 1/l_I + 1/l_M$. Mean chord lengths have been used frequently to analyse small-angle scattering data¹⁶⁵. The advantage of T is that it is independent of the shape and arrangement of the particles¹⁶⁶.

For particle of known shape, e.g. plate-like particle, T can be written as:



$$T = 4 \frac{V_I (1-\phi)}{S_{IM}} = 4 \frac{abc}{2(ab+bc+ac)} (1-\phi)$$

or

$$T \cong 2a(1-\phi), \text{ if } a \ll b, c \quad (\text{Equation A.29})$$

A.6 Nitrogen Sorption

It has already been known for long time that a porous solid can take up relatively large volume of condensable gas. Gas adsorption is widely used for the characterisation of porous materials of which pore sizes lie within nanometer range to get information on the specific surface area, pore sizes and pore distribution of the solid¹⁶⁷. The pores are classified on the basis of their diameter (or width) as micropores (below 2 nm), mesopores (between 2 and 50 nm), and macropores (above 50 nm)¹⁶⁸. The gas

(adsorbate) used for the measurement should have certain characteristics. It should be chemically inert towards the solid sample (adsorbent), it should have saturation vapour pressure large enough to carry out the measurements accurately at working temperatures, and the shape of adsorbate molecule should be close to spherical symmetry. In this regards, nitrogen is by far most widely used as adsorbate gas. Other gases, such as argon, krypton, benzene, and carbon dioxide are sometimes used for the measurement.

The nitrogen sorption measurement is performed at constant temperature of 77.35 K, which is the boiling point of liquid nitrogen. Firstly, the sample is outgassed by exposure of the surface to high vacuum to remove all physisorbed material from the surface of the adsorbent. Afterwards, small amounts of gaseous adsorbate are fed gradually and adsorbed on to the sample. The volume of gas adsorbed V_A is taken as volume of the same amount of gas at standard temperature and pressure condition (STP). The partial pressure of gas P above the sample surface is measured relative to the saturation vapour pressure P_0 at a constant temperature. The plot of the volume adsorbed V_A versus relative pressure P/P_0 gives the so-called adsorption isotherm, which is defined as the relationship between the amounts of gas adsorbed and the pressure or relative pressure at constant temperature.

There are five different types of adsorption isotherms according to Brunauer classification¹⁶⁷ and the relatively rare *stepped isotherm*, designated as type VI as can be seen in Figure A.19.

Type I isotherms is usually considered to be indicative of adsorption in micropores by exhibiting prominent adsorption at low relative pressures and then level off. In case of macropores, there is multilayer formation in such a manner that the amount adsorbed increases gradually as the relative pressure increases, although the multilayer build-up close to the saturation vapour pressure may be quite abrupt¹⁶⁹. This unrestricted multilayer formation process gives rise to type II and type III isotherms. Depending on the surface properties of a given solid, there may be a pronounced stage of the monolayer formation (type II) or the adsorption isotherm may be convex in the whole pressure range (type III). The latter behaviour can be observed when lateral interactions between adsorbed molecules are strong in comparison to interactions between the adsorbent surface and adsorbate¹⁶⁹. There is no adsorption-desorption

hysteresis since the adsorption and desorption branches of the isotherm coincide. Type IV and V isotherms are characteristics of mesoporous solid indicated by the appearance of adsorption-desorption hysteresis loops. The adsorption process is initially similar to that on macroporous solids, but at higher pressures the amount adsorbed rises very abruptly due to the capillary condensation in mesopores. The adsorption isotherm levels off after these pores are filled. The distinction between types IV and V is analogous to that between types II and III. The *stepped isotherm*, appropriately designated type VI is relatively rare and is particularly of theoretical interest.

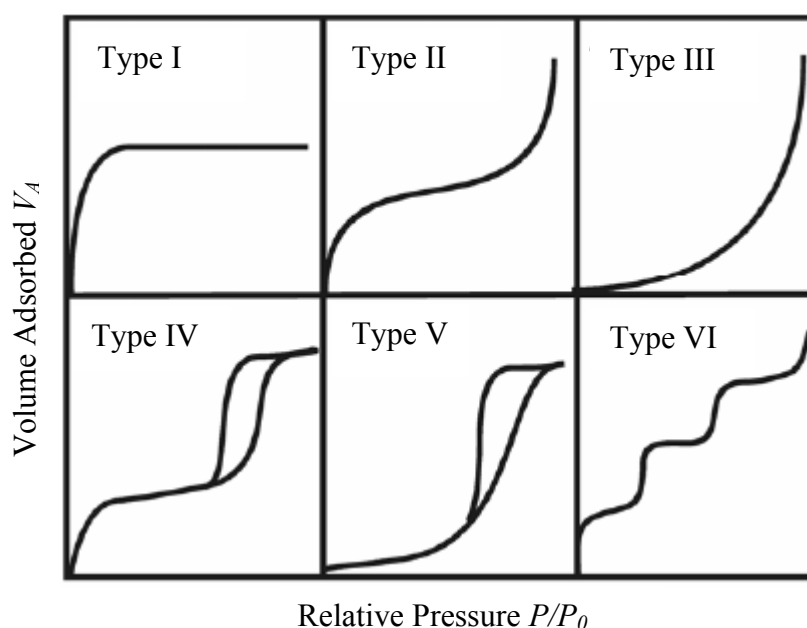


Figure A.19 The five types of adsorption isotherm, I to V according to Brunauer classification, together with type VI, the stepped isotherm¹⁶⁷.

There are 4 different types of hysteresis loops as shown in Fig. A.20 based on different hysteresis shapes which are related to the specific pore structures¹¹⁶. Type H1 is often associated with porous materials consisting of agglomerates (assemblages of rigidly joint particles) or compacts of approximately uniform spheres in fairly regular array, and hence having narrow distribution of pore size. Type H2 loop which is exhibited by many porous adsorbents (e.g. inorganic oxide gels and porous glasses) is indeed quite difficult to interpret. In the past, it is often referred to as ‘ink bottle’ pores which provides an over-simplified picture since the role of network effect must be taken into account. Type H3 loop is observed in materials comprising of aggregates (loose assemblages) of plate-like particles forming slit-like pores. Type H4 loop is often

associated with narrow slit-like pores and may also arise from the presence of large mesopores embedded in a matrix with pores of much smaller size¹⁶⁹. In many systems, especially those containing micropores, the extending hysteresis at low pressure (indicated by the dashed lines in Fig. A.20) may be associated with the swelling of non-rigid porous structure or chemisorption phenomenon¹¹⁶.

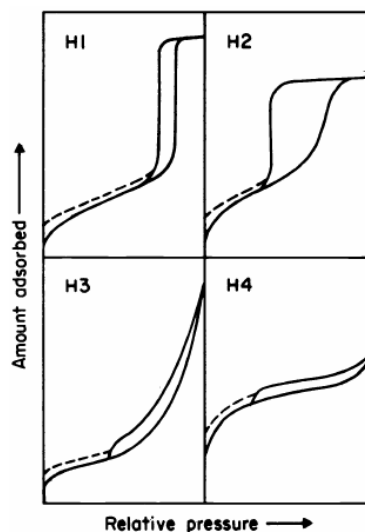


Figure A.20 Types of hysteresis loops¹¹⁶.

For the evaluation of specific surface area from gas adsorption data, the Brunauer-Emmett-Teller (BET) method has been widely used as the standard method^{167, 170}. The evaluation of the specific surface area using the BET method is based on the evaluation of the monolayer capacity, which is the number of adsorbed molecules in the monolayer on the surface of a material, by fitting experimental gas adsorption data to the BET equation (Equation A.30). The obtained monolayer capacity is then multiplied by the cross-sectional area of the nitrogen molecule in the monolayer formed on a given surface.

$$\frac{P/P_0}{V_A(1-P/P_0)} = \frac{1}{V_m C} + \frac{(C-1)P/P_0}{V_m C} \quad (\text{Equation A.30})$$

Where

P/P_0 = relative pressure

V_A = Volume of gas adsorbed on the adsorbent

V_m = Volume of gas needed to form a monolayer on the entire sample surface

C = Constant related to enthalpies of adsorption, H_A and condensation H_C given

$$\text{as } C \approx \exp[(H_A - H_C)/RT]$$

The adsorption data gives the values for the terms on the left hand side of Eq. A.30, from which the parameters C and V_m on the right hand side of the equation can be easily calculated. One can then calculate the specific surface area of the sample using Equation A.31.

$$SA_{BET} = \frac{V_m N_A \sigma}{V_0 m} \quad (\text{Equation A.31})$$

Where

SA_{BET} = Specific surface area evaluated using BET method

N_A = Avogadro's number

σ = Area per molecule of the adsorbate gas, i.e. 16.2 \AA^2 for nitrogen¹¹⁶

V_0 = Molar volume of the adsorbate

m = Mass of sample

Study of the capillary condensation marked by the hysteresis loop occurrence in generally Type IV isotherm will provide us the information on pore volume, leading to pore size and pore morphology analysis. Capillary condensation is intimately bound up with the curvature of a liquid meniscus. In case of mesopores, condensation occurs at lower relative pressures. The monolayer of nitrogen molecules form a curved interface which acts as nucleation site for condensation of gaseous nitrogen. From the Kelvin equation (Eq. A.32) it follows that the vapour pressure at which the adsorbate condenses must be less than the saturation vapour pressure P_0 . Consequently, "capillary condensation" of vapour to a liquid should occur within a pore at some pressure P^* determined by the value of r_m of the pore. The smaller the r_m , the lower will be the critical condensation pressure.

$$\ln\left(\frac{P^*}{P_0}\right) = -\frac{2\gamma V_0 \cos \theta}{RT r_m} \quad (\text{Equation A.32})$$

Where

P^* = Critical condensation pressure or vapour pressure

P_0 = Saturation vapour pressure

γ = Surface tension of the liquid adsorbate

V_0 = Molar volume of the liquid adsorbate

θ = Contact angle of the condensed adsorbate with the sample surface

R = Gas constant

T = Absolute test temperature

r_m = Mean radius of curvature

The mean radius of curvature r_m is related to pore size by considering the thickness of an adsorbed film deposited on the pore walls prior to the capillary condensation. Thus, capillary condensation occurs not directly in the pore itself but rather in the inner core as can be seen in Figure A.21.

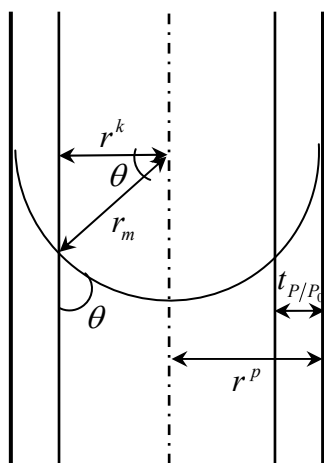


Figure A.21 Cross-section, parallel to the axis of a cylindrical pore of radius r^p , showing the “inner core” of radius r^k and the adsorbed film of thickness determined by the value of the relative pressure t_{P/P_0} together with the relationship between r_m of the Kelvin equation and the core radius r^k for a cylindrical pore with a hemispherical meniscus; θ is the angle of contact¹⁶⁷.

It is obvious that r_m is correlated to r^k by the contact angle according to the Eq. A.33.

$$r^k = r_m \cos \theta \quad (\text{Equation A.33})$$

For the simplicity, in case of nitrogen, the contact angle is taken as $\theta = 0^\circ$, which gives $\cos \theta = 1$, hence the mean radius of curvature r_m thus becomes equal to the radius of the pore less the thickness of the adsorbed film on the walls. The pore radius can be calculated by modification of Kelvin equation (Eq. A.34) giving:

$$r^p = -\frac{2\gamma V_0}{RT \ln\left(\frac{P^*}{P_0}\right)} + t_{P/P_0} \quad (\text{Equation A.34})$$

Appendix B

EXPERIMENTAL DETAILS

B.1 Samples and Preparations

B.1.1 Silica in *Equisetum hyemale*

B.1.1.1 Sample preparation

Shoots of scouring rush (*Equisetum hyemale*) were collected from the Botanical Garten Drachenberg at the University of Potsdam, Germany. *E.hyemale* starts to grow in spring time and can persist for three seasons or more (perennial plant). *E.hyemale* shoots were harvested in autumn 2004 for the first measurement and new shoots commenced in 2005 were harvested from May until March the following year for the silica contents and silica distribution investigations. Fresh samples were kept in a refrigerator with the temperature of -20°C to preserve the biological tissues for quite a long time without any decay.

The basal internodes (3-4 cm in height and 3-5 mm in diameter) were preferably used for all subsequent microstructural and analytical investigations because they were considered to be more mature than the upper internodes, thus supposed to be homogeneously silicified along the whole internodes. They were washed in desalinated water to remove accompanying dust and soil prior to the investigations. Different samples for different techniques were prepared as follows:

a) Native *E.hyemale*

Samples in their original forms without being subjected to any treatments were prepared for the investigations at all hierarchical levels using novel techniques in order to shed light on the silica characteristics and properties found in its native state.

- Internodes

Internodes were prepared for microtomography investigations. Internodes of three different parts (top, middle and base) of young (1-month-old) as well as mature (six-month-old) stalks were examined for their patterns of silica distribution by cutting each internode above the intercalary meristems of about 0.5-1 cm depending on the internodal lengths. The measurements were conducted in dry and wet condition. Samples in fully wet condition were prepared by placing fresh internodes (about 1 cm long) in water filled Eppendorf tubes to partly match the contrast between the soft tissues and the (water filled) hollow spaces and to avoid the shrinkages during the measurement, which could influence the absorption patterns due to changes in tissues thickness.

- Cross sections

Cross sections were prepared by axially cutting the fresh materials using razor blades with a thickness of approximately 200 μm for the semi-quantitative analysis of Si using SEM/EDX and Si mapping with EDX.

- Outer surface and tangential sections

Outer surface were also prepared for SEM/EDX investigations. The hollow stems were dissected into half parts and put onto the aluminium stubs. Furthermore, tangential sections (epidermal layers) were made by carefully scrapping the outer surface by razor blades to isolate the epidermal layers where silica was mostly accumulated. Epidermal layers were characterised by extensive methods, i.e. Raman microscopy, FTIR microscopy, and X-ray scattering. In addition, the samples were kept wet in a Petri dish during the measurement with Raman due to its insensitivity towards water, thus preserving the samples in their native state.

b) Embedded *E.hyemale*

For backscattered electron imaging, a completely flat sample surface was highly required to reduce the disturbing contrast coming from the morphological effects. Therefore, samples were needed to be embedded, ground, and polished. Samples were subjected to a successive water removal by soaking into different alcohol solution grades, i.e. 70%, 80% and 90% for about half a day for each treatment and finally immersed in 100% alcohol for three times within 2 days. The samples were

then transferred to MMA (methylmethacrylat) solutions and replaced for 2 times within a day to remove the remaining alcohols. Vacuum pumping was applied to remove the air bubbles trapped within the samples. Afterwards, the samples were put into a mould and filled with the polymer mixtures containing 10 grams MMA and 30 mg AIBN (azodiisobutyronitril) and placed into the oven. The polymerisation started gradually until the temperature reached 45°C for 1 day holding time. The temperature was then increased to about 55°C and samples were held for another 1 day for a complete curing process. Cross sections with thickness of about 0.5 cm were obtained by cutting the embedded samples by using a low speed saw (ISOMET, Buehler, Germany), which were then ground and polished using a polishing machine, type 1PM57 (Logitech, UK) for getting a flat surface. Different SiC papers grades (1200, 2400 and 4000) were consecutively used for several minutes, followed by polishing with 3 µm and 1 µm diamond papers for about 10 minutes for each treatment.

c) Chemically/thermally treated *E.hyemale*

Several chemical/thermal treatments of *E.hyemale* were exclusively carried out either to remove the accompanying organic matrix, such as cellulose or other inorganic substances, such as Ca, K, Na, etc, thus increasing the signal for silica detections and improving the accuracy of data analysis since the system was greatly simplified. Chemical treatments and thermal treatments were also combined to get “pure silica” from *E.hyemale*. Some treatments conducted within this research were described as following:

- Calcinated *E.hyemale*

One-year-old *E.hyemale* internodes were calcinated in air at 400° for 48 hours with a heating rate of 1 K/min in a furnace type L5/12/06 (Nabertherm, Germany) for the organics removal. The intact ash was investigated for its morphological structure by SEM, while powdered ash was prepared for SAXS/WAXS analysis. Calcinations were carried out at low temperature in order to not change the silica polymorph and to only insignificantly alter the structure of the original silica accumulated in the native tissue.

- H₂O₂-treated *E.hyemale*

One-month-old *E.hyemale* was soaked in 50 ml of 30% H₂O₂ for about 18 months without being penetrated by light to slow down the H₂O₂ oxidation process into water and oxygen. The oxygen would gradually oxidize the organic as well as inorganic compounds, leaving very thin epidermal layers which were considered to contain pure silica. H₂O₂-treated *E.hyemale* samples were characterised by SEM, FTIR, SAXS/WAXS, and nitrogen sorption.

- HCl-treated *E.hyemale* followed by calcination

E.hyemale stalks were dried at 105°C for 48 hours before being subjected to an acid treatment using 10%-HCl for 2 hours at boiling temperature to remove all inorganic substances except of silica and followed by the calcination process to completely remove the organic components. The calcination was carried out in air atmosphere with a heating rate of 1 K/min and 2 hour holding time at 400°C. The obtained biogenic silica was powdered and investigated by SAXS/WAXS and nitrogen sorption analysis. Additionally, biogenic silica powder obtained by calcinating HCl treated sample at 600°C for 2 hours with a heating rate of 2 K/min in a tube furnace type RE 1.1 (Heraeus Thermicon, Germany) was analysed by using FTIR microscopy and could be used as a reference.

d) Powdered *E.hyemale*

Powdered samples of both native and chemically/thermally treated *E.hyemale* were needed for particular investigations using SAXS/WAXS and nitrogen sorption techniques. For the element analysis using XRF method, dried *E.hyemale* stalks (105°C, 2 hours) were milled and 0.5 mm particles were collected after sieving. Lithium tetraborat (Li₂B₄O₇) was added to the sample powders and then they were heated up in the furnace until melting down. The liquid was poured into a form and tablets with a diameter of 32 mm and with plane surfaces were obtained after cooling. In addition, the powder of H₂O₂ treated *E.hyemale* sample was used for the investigation using FTIR spectroscopy in transmission mode.

B.1.1.2 Silica content determination by gravimetric method

Silica contents during aging were determined for the study of silica accumulations in *E.hyemale* stalks as the time increased and also for the macroscopic silica distribution of different segments within *E.hyemale* stalks. The stalks were dried at 105°C for 2 hours, and powdered. Five grams of powdered samples were required for the silica content analysis. At first, they were purified by 10% HCl to remove the other inorganic substances except of silica, followed by oxidation in air at 750°C for 2 hours for the organics removal and finally, the silica content was determined by gravimetric method. For the determination of silica distribution of different segments in *E.hyemale* stalks, the nodes and internodes were dissected into five different segments, i.e.: top, upper middle, middle, lower middle, and base. Each segment consisted of about 2-3 nodes/internodes depending on the stalk lengths, which comprised of normally 10-12 internodes. They were collected in different containers and silica contents were determined for each segment according to the procedure as mentioned above. The cones were excluded and its average silica content was determined separately.

B.1.1.3 Carbon content determination by gravimetric method

Carbon contents in different segments within *E.hyemale* stalks were also determined as a complement to its corresponding silica contents. Carbon as well as other light elements, for instance H, N and S were classically determined using a gravimetric method in a light element analyser (LECO, Switzerland).

B.1.2 Isolation of Silica from *Equisetum hyemale*

B.1.2.1 Sample preparation

For this experiment, dry and powdered *E.hyemale* shoots harvested in November 2002 and stored for about 4.5 years at room temperatures were used. In an attempt to isolate pure biogenic amorphous silica from *E.hyemale*, some thermal and chemical treatments

were performed to get rid of the organic matrix (cellulose, hemicellulose, pectin) as well as the inorganic substances. Two sets of samples were prepared:

i) Calcination of native, dry *E.hyemale* in air at seven different temperatures (300°C, 350°C, 400°C, 450°C, 500°C, 600°C, 750°C) in a furnace type L5/12/06 (Nabertherm, Germany). A low heating rate of 1 K/min and holding time of 48 hours were applied. Ash of *E.hyemale* of which silica content is about 60% was delivered after this process.

ii) To produce pure biogenic amorphous silica (calcined HCl-treated sample) from *E.hyemale*, a chemical treatment using 10% HCl (see section B.1.1) was performed to largely remove all inorganic compounds except silica, prior to the calcination in air at the same temperatures and conditions as applied to the ash production. The obtained ash and silica ash samples were then pressed into pellets with 0.2 mm thickness in order to have a well defined powder volume in the X-ray beam for SAXS measurement.

B.1.2.2 Density determination

Densities of both ash and silica ash samples calcined at 600°C were determined using a pycnometer, which is a flask with a definite volume. The weight of empty pycnometer and weight of pycnometer filled by water were measured using an analytical balance, thus density of water was obtained. The powder was added to the pycnometer filled by water, and then was subjected to ultrasonic impuls and vacuum for a short time to remove the gas bubbles trapped between the particles. The mass of the sample was determined based on the amount of water displaced by the powder and thence the specific gravity of the powder and its density.

B.1.3 Silicon Carbide (β -SiC) from *Equisetum hyemale*

B.1.3.1 Sample preparation and pyrolysis of *E.hyemale*

β -SiC can be simply produced from *E.hyemale* by heat treatment at high temperature (1500-1600°C) under inert atmosphere. Several attempts for β -SiC synthesis from the native *E.hyemale* stalks under different reductive atmospheres and different process parameters during the heat treatments (SiC/C 1, SiC/C 2, SiC/C 3) were performed. The multistep heat treatments were carried out for both SiC/C 1 and SiC/C 2 samples. The first step is the pyrolysis under vacuum up to 1000°C with a heating rate of 2 K/min and holding time of 2 hours in a tube furnace type RE 1.1 (Heraeus Thermicon, Germany). Afterwards, the samples were transferred into a vacuum inert gas graphite furnace (HTM Reetz, Germany) for the pyrolysis at high temperature in vacuum (SiC/C 1) and in Argon atmospheres (SiC/C 2). Prior to pyrolysis, the furnace chamber was flushed by nitrogen or argon for at least twice to ensure a non-oxidising atmosphere. The temperatures were increased from room temperatures to 1500°C by using a heating rate of about 13 K/min. The maximum temperatures were held for 0.5 h to allow silica to be in contact with carbon for the silicon carbide synthesis. The gauge pressure within furnace chamber was about 10 mBar during the pyrolysis process.

SiC/C 3 sample was produced after the pyrolysis process in a high temperature furnace, type FRH 50/300/1600 (Linn High Therm, Germany). Argon was flowed into the furnace chamber for 24 hours with a volumetric flow rate of 3.6 L/h to remove the air out of the system. Pyrolysis was then started by increasing the temperature from room temperature to 1500°C with an increment rate of 12 K/min. The maximum temperature was maintained for 2 hours. Argon gas flow was maintained at about 3.6 L/h and the pressure within furnace chamber was about 15 mBar during the pyrolysis process. The SiC/C 3 sample was further purified by subsequent oxidative thermal treatment and chemical treatment with hydrofluoric acid to obtain pure β -SiC compounds (SiC 1). The detail of the purification process was described in the following sub-section.

Finally, HCl-treated *E.hyemale* sample (see Section B.1.1) was used as the precursor for the synthesis of SiC with high grade and high purity. Pyrolysis was carried

out under vacuum in a high temperature furnace, type FRH 50/300/1600 (Linn High Therm, Germany). The temperature was increased from room temperature to 400°C with a heating rate of 1 K/min and maintained for 100 hours, and was then further heated up to 1500°C (2 K/min, 6 hours). The pyrolysed *E.hyemale* was then post-treated (see the following sub-section) to get pure β -SiC (SiC 2).

B.1.3.2 Purification of SiC/C into SiC

After the pyrolysis, SiC/C composite was produced accompanied by the remaining unreacted silica, degraded organics, and other minor metal compounds. Therefore, purification by means of thermal or chemical treatments had to be performed. At first the pyrolysed *E.hyemale* was calcinated at 750°C for 1 hour in a muffle furnace, type LM 312 (Linn High Therm, Germany) to remove the remaining organic degraded products. The furnace was heated up to 750° without any sample and held for 1 hour for the system stabilization at the maximum temperature prior to the calcinations. During the calcinations, some fractions of SiC were oxidized into SiO₂ silica. Therefore, the subsequent chemical treatments using 40% HF was conducted to remove the remaining silica derived from the unreacted native silica as well as silica from the oxidations of SiC. Finally, they were washed by dilute HCl (5%) to remove the trace metallic impurities and were rinsed by water and dried. Several characterisation techniques such as microtomography, SEM/EDX, SAXS/WAXS, and nitrogen sorption were used for the structural investigations of the resulting *E.hyemale* derived SiC/C as well as SiC compounds.

B.2 Analytical Methods

B.2.1 X-ray Microtomography

Microtomography was performed with a laboratory instrument (SkyScan-1072, Belgium), operated at 100 KV and 100 μ A. An air-cooled X-ray point source with a spot size of 10 μ m was used to illuminate the samples with a polychromatic X-ray cone

beam. X-ray projections were collected for sample rotation of 180° with a rotation step of 0.9° and an exposure time 1.7 s, at a geometrical magnification of 30 X. Data reconstruction was performed using a filtered backprojection algorithm for cone beam tomography including corrections for beam hardening (NRecon, Skyscan). The Amira™ program (Zuse Institute Berlin) was used for the final 3D rendering and visualisation.

B.2.2 Scanning Electron Microscopy (SEM)

An Environmental Scanning Electron Microscopy (ESEM), The Quanta FEG 600 (FEI, Netherland) was used for the sample topography imaging and backscattered electron analysis. SEM mode in low vacuum was chosen for the biological tissues imaging, thus sputtering was not necessary. Large field detector (LFD), which captured signals coming from the secondary electrons as well as backscattered electron for the image formation, was usually used in low vacuum mode. A voltage of 10 kV and pressure of about 100 Pa was generally used. For backscattered analysis, high vacuum was absolutely needed, thus sputtering of sample with carbon was necessary. The voltage of about 20 kV was applied. Solid-state detector (SSD) detector was used to record the backscattered electron signal from the sample, while Everhard-Thornley detector (ETD) was used for the corresponding SEM image.

For the energy dispersive X-ray analysis (EDXA), a DSM 940A SEM (Zeiss, Germany), equipped with an EDXA link ISIS-System (Oxford Instruments) and operated at 20 KV and 1.3×10^{-4} Pa was used. SEM was employed for the morphological observation of the cross sectional or the longitudinal (surface) anatomy and EDXA was utilized for semi-quantitatively elemental analysis of the samples. The energy resolution of EDXA was 133 eV, which corresponds to a penetration depth of the electron beam of roughly 3 μm for the Si analysis. Si was quantified in weight percent with respect to all elements detected within the local illuminated areas. The error of the semi quantitative analysis due to the limitation of the instrument used was approximately 1-2%.

B.2.3 Raman Microscopy

A Confocal Raman Microscope (CRM200, WITEC, Germany) equipped with a water immersion objective (Nikon, 60x, numerical aperture (NA) = 1) and a piezo scanner (P-500, Physik Instrumente) were used for spectroscopic imaging. A linear polarised laser (diode pumped green laser, $\lambda = 532$ nm, CrystaLaser) was focused with a diffraction limited spot size ($0.61\lambda/NA$) and the Raman light was detected by an air-cooled, back illuminated spectroscopic CCD (ANDOR) behind a grating (600 g mm^{-1}) spectrograph (ACTON) with a resolution of 6 cm^{-1} . For the mapping through a silica knob, an integration time of 2.5 s in $0.5 \text{ }\mu\text{m}$ steps was chosen and every pixel corresponded to one scan. The ScanCtrlSpectroscopyPlus software (WITEC, Germany) was used for measurement setup and image processing. Chemical images were achieved by using a sum filter, integrating over defined wavenumber areas in the spectrum. The filter calculated the intensities within the chosen borders and the background was subtracted by taking the baseline from the first to the second border. Images of amorphous silica, silanol groups, and cellulose were achieved by integrating over $245\text{-}570 \text{ cm}^{-1}$, $937\text{-}993 \text{ cm}^{-1}$, and $1054\text{-}1191 \text{ cm}^{-1}$, respectively. On the chemical images, selected areas differing in composition were marked to calculate average spectra from those areas.

B.2.4 FTIR

FTIR microscopy was carried out as a complementary technique to Raman microscopy. A FTIR spectrometer (Vertex 70, Bruker, Germany) equipped with a microscope (Hyperion 2000, Germany) and a 20x attenuated total reflection (ATR) objective was used for the measurement on the outer sample surfaces. The epidermal layer of *E.hyemale* was mounted on a glass slide, whereas silica powder was spread on a KBr window using a spatula. The visible light mode enabled to view the sample and to locate the ATR objective exactly at the regions of interest. The sample stage was then lifted up to be in contact with the ATR crystal, whose tip diameter was about $100 \text{ }\mu\text{m}$. The IR beam was going through the ATR crystal; the evanescent IR wave was reflected from the sample surface and transferred back to the system to a liquid nitrogen-cooled MCT detector. The spectra were collected with a spectral resolution of 4 cm^{-1} within the

4000-600 cm^{-1} region by averaging 128 scans for the *E.hyemale* samples and 64 scans for the silica powder. The resulted interferograms were converted back to the frequency domains (FTIR spectra) by means of Blackman-Harris 3-Term function, power spectrum as the phase correction mode and a zero filling factor of 2. The OPUS software (Bruker, Germany) was used for the measurement operation as well as for spectral treatment and analysis. Baseline correction was performed using concave rubberband correction method with iterations number of 10 and 300 baseline points.

Furthermore, the H_2O_2 -treated sample was characterised in transmission mode by using a FTIR spectroscopy (Perkin Elmer, 16 PC, Germany). Five scans were taken with a spectral resolution of 2 cm^{-1} within the region range of 400 to 4000 cm^{-1} . The Spectrum v.2 Software (Perkin Elmer, Germany) was used for the spectral treatment and analysis.

B.2.5 X-ray Fluorescence

X-ray Fluorescence was carried out for the elemental analysis. An energy dispersive spectrometer X-LAB₂₀₀₀ (Spectro, Germany) equipped by BRAGG and BARKLA polarisators was employed. X-ray photons were collected with a Si(Li) detector. The instrument was operated by using special software integrated in a PC. The spectra analysis and evaluation was fully automatically executed.

B.2.6 X-ray Scattering

The SAXS/WAXS measurements were carried out on a Nanostar instrument (Bruker AXS, Germany) with a sealed tube X-ray generator operated at 40 KV and 35 mA. A parallel, monochromatic X-ray beam, with wavelength $\lambda = 0.154 \text{ nm}$ (Cu $K\alpha$) was provided by a parabolically bent, graded multilayer (Göbel mirror). Data were collected with a single photon counting area detector (HiStar, Bruker AXS). The sample-detector distance was set to 80 mm and 1050 mm for WAXS and SAXS, respectively. This allowed covering overlapping ranges of scattering vectors q from $0.1 \text{ nm}^{-1} < q < 2 \text{ nm}^{-1}$ for SAXS and $1.5 \text{ nm}^{-1} < q < 23 \text{ nm}^{-1}$ for WAXS, where $q = 4\pi\sin(\theta)/\lambda$ with 2θ being the scattering angle. The two-dimensional SAXS and WAXS patterns were azimuthally

averaged to obtain one-dimensional scattering profiles of the intensity versus the length of the scattering vector q , and the instrument related background was subtracted.

B.2.7 Powder Diffraction

A powder diffractometer (D8, Bruker AXS, Germany) with a sealed tube X-ray generator in θ - θ geometry operated at 40 KV and 40 mA was used to get the XRD patterns of the measured samples. A parabolically bent, graded multilayer (Göbel mirror) was used for beam parallelisation and for monochromatisation (Cu-K α radiation with a wavelength of 0.154 nm). Data were collected with a solid state detector (Sol-X, Bruker AXS) in steps of $\Delta(2\theta) = 0.05^\circ$ and a step time of 6 s. The scattering angle 2θ was then converted into the modulus of scattering vector q ($q = 4\pi\sin(\theta)/\lambda$).

B.2.8 Nitrogen Sorption

Nitrogen sorption studies were carried out using an AUTOSORB-1 MP (Quantachrome, USA) instrument. For the analysis the samples were transferred into sample cells and evacuated at different temperature from 100°C for at least 6 hours depending on the characteristics of samples. The measurements were performed at -196°C, which was the boiling point of liquid nitrogen. AUTOSORB Software, AS1Win was used for the data analysis. The specific surface area was calculated using BET methods, whereas pore size and pore size distribution was determined using the methods proposed by Barrett, Joyner and Halenda (BJH) and by Dollimore and Heal (DH).

Appendix C

SAXS/WAXS DATA EVALUATION

The measured SAXS/WAXS raw data have to be corrected by the transmission factor according to the equation below, whereas the additional intensity correction due to dark current (electronic noise) can be neglected since the effect is not significant for the instrument used.

$$I = I_S^M - \tau_S \cdot I_{EB}^M, \text{ for free standing sample (no sample cell)}$$

or

$$I = I_S^M - \left(\frac{\tau_{S+EC}}{\tau_{EC}} \cdot I_{EC}^M \right), \text{ for sample with cell}$$

(Equation C.1)

Where

I = corrected intensity

I_S^M = measured intensity of sample

τ_S = transmission of sample

τ_{S+EC} = transmission of sample and empty cell

I_{EB}^M = measured intensity of empty beam

I_{EC}^M = measured intensity of empty cell

The one-dimensional scattering profile of the intensity (corrected) versus the length of the scattering vector, q obtained after the azimuthal integration is then further evaluated.

C.1 Analysis of Powder Diffraction/WAXS Data

C.1.1 Phase identification

Powder diffraction/ WAXS pattern of an unknown material can be used to identify chemical compounds contained within the materials by matching the WAXS pattern

with the WAXS pattern / fingerprint of known compound from the reference pattern database. For this purpose, the MATCH software (CrystallImpact, Germany) embedded with PDF-2 as database was used. Figure C.1 is an example showing the phase identification of SiC derived from HCl-treated *E.hyemale* (SiC 2) using MATCH software which fits well with β -SiC compound from the reference.

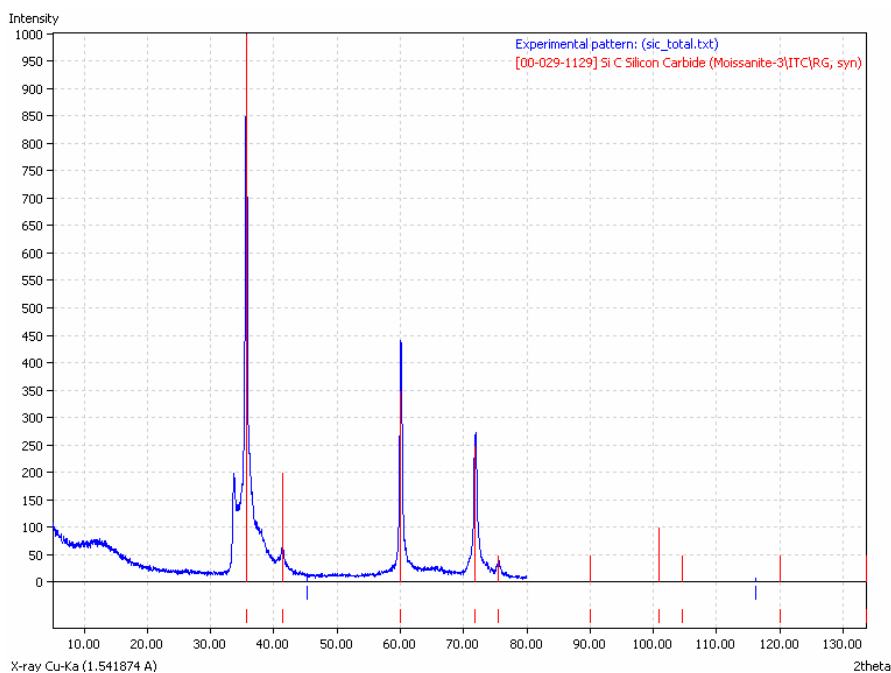


Figure C.1 Phase identification of SiC derived from HCl-treated *E.hyemale* (SiC 2) using MATCH Software.

C.1.2 Determination of the fraction of crystalline silica

Silica isolated from *E.hyemale* after HCl treatment followed by calcination shows several crystalline peaks attributed to α -quartz besides a prominent broad peak of amorphous silica based on the powder diffraction pattern. The fraction of crystalline silica was determined by calculating the ratio of the integral intensity in the profiles of the crystalline peaks to the total scattering intensity. Amorphous silica peak and all of quartz peaks were separated from the total integral intensity profile (Fig. C.2 (A)), and then fitted using a Gaussian function (Fig. C.2 (B), (D)), corrected by background subtraction and finally the areas below the integrated intensity profile were determined (see Eq. A.27).

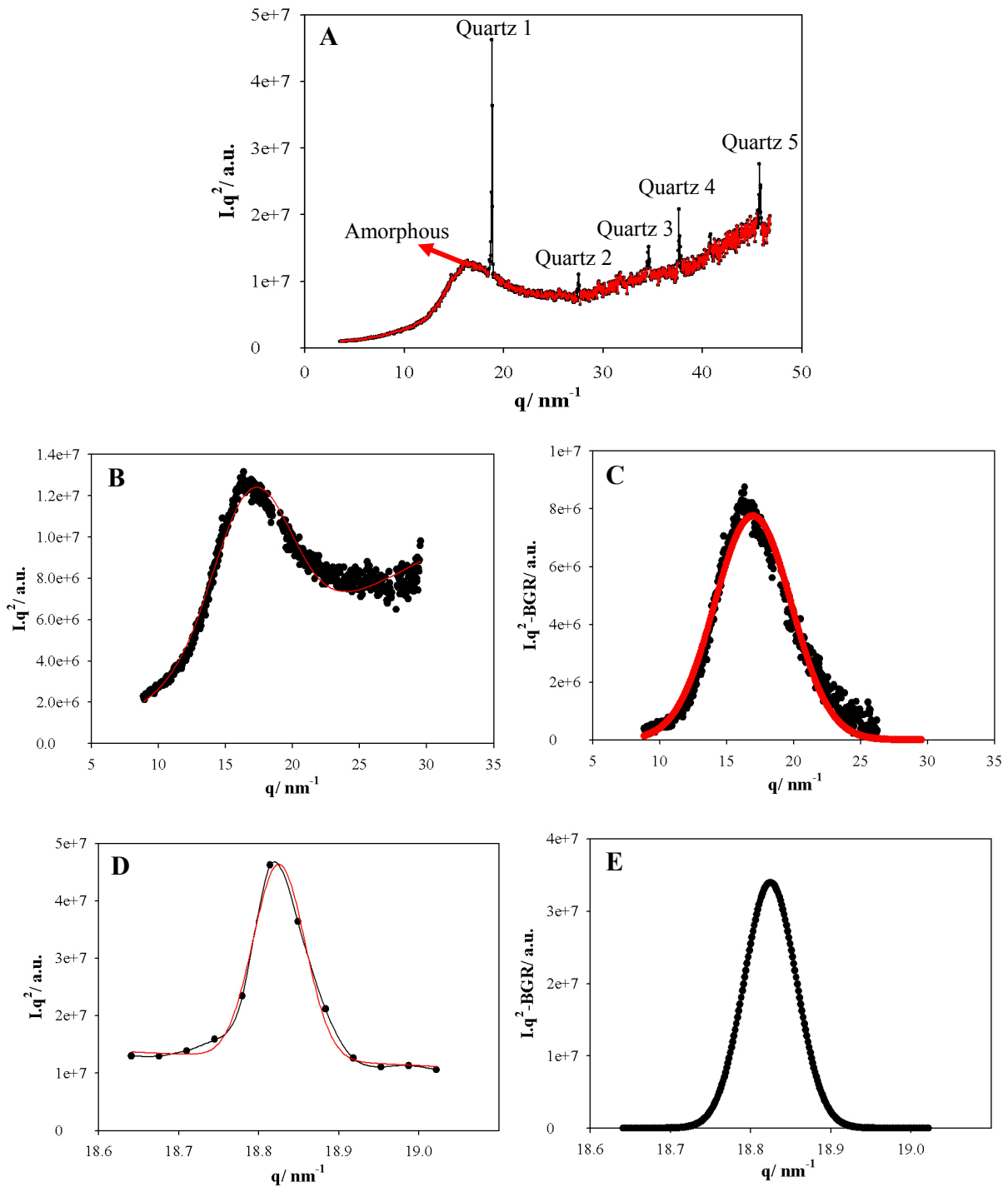


Figure C.2 Plot of Integral intensity versus scattering vector: (A) Silica obtained from calcination of HCl-treated *E.hyemale* at 450°C ; (B) Amorphous silica; (C) Amorphous silica with background subtraction; (D) Quartz 1; (E) Quartz 1 with background subtraction.

Area of amorphous silica = 55,657,699.5771

$$\begin{aligned} \text{Area of crystalline silica} &= \sum_{i=1}^5 \text{Area of quartz}_i \\ &= 2,763,191.4602 + 103,551.3825 + 130,664.0473 \\ &\quad + 316,672.202 + 419,330.6891 \\ &= 3,733,409.7811 \end{aligned}$$

Total Area = 55,657,699.5771 + 3,733,409.7811 = 59,391,109.3582

$$\begin{aligned} \text{Fraction of crystalline silica } (\alpha\text{-quartz}) &= (3,733,409.7811/59,391,109.3582) \times 100\% \\ &= \underline{6.3\%} \end{aligned}$$

C.2 Analysis of SAXS Data

C.2.1 Porod's law and integrated SAXS intensity

Since the scattering intensities at large q obtained from biogenic silica and ash samples are proportional to q^{-4} (Fig. C.3 (A), (D)), Porod's law prevails (Glatter and Kratky, 1982). This means that there are sharp interfaces between spatially separated phases of different electron density. Porod's plot can be drawn by plotting $I \cdot q^4$ vs. q^4 and then linear regression was applied over a certain linear range, which was determined arbitrarily (Fig. C.3 (B), (E)). The slope is the background which was subtracted from the scattering intensity, whereas the intercept is the Porod constant which is proportional to the specific interfacial area between the two phases (see Eq. A.26). The Kratky plot, which is the scattering intensity after background subtraction multiplied by the square of q as the function of the scattering vector q can be seen in Fig. C.3 (C), (F). The area below the curve is proportional to the integrated SAXS intensity (see Eq. A.27) related to the volume fraction. The T-parameter, which is a measure for the smallest dimension of particles or interconnected domains (Fratzl, 1997) can be then determined from the combination of Porod's law and integrated SAXS intensity (see Eq. A.28). Since the integrated scattering intensity of ash sample at very low q tends to increase with an unknown manner, in contrast to that of biogenic silica showing a

maxima (Fig. C.3 (C) vs. (F)), the T-parameter calculated for the ash sample gives a lower boundary.

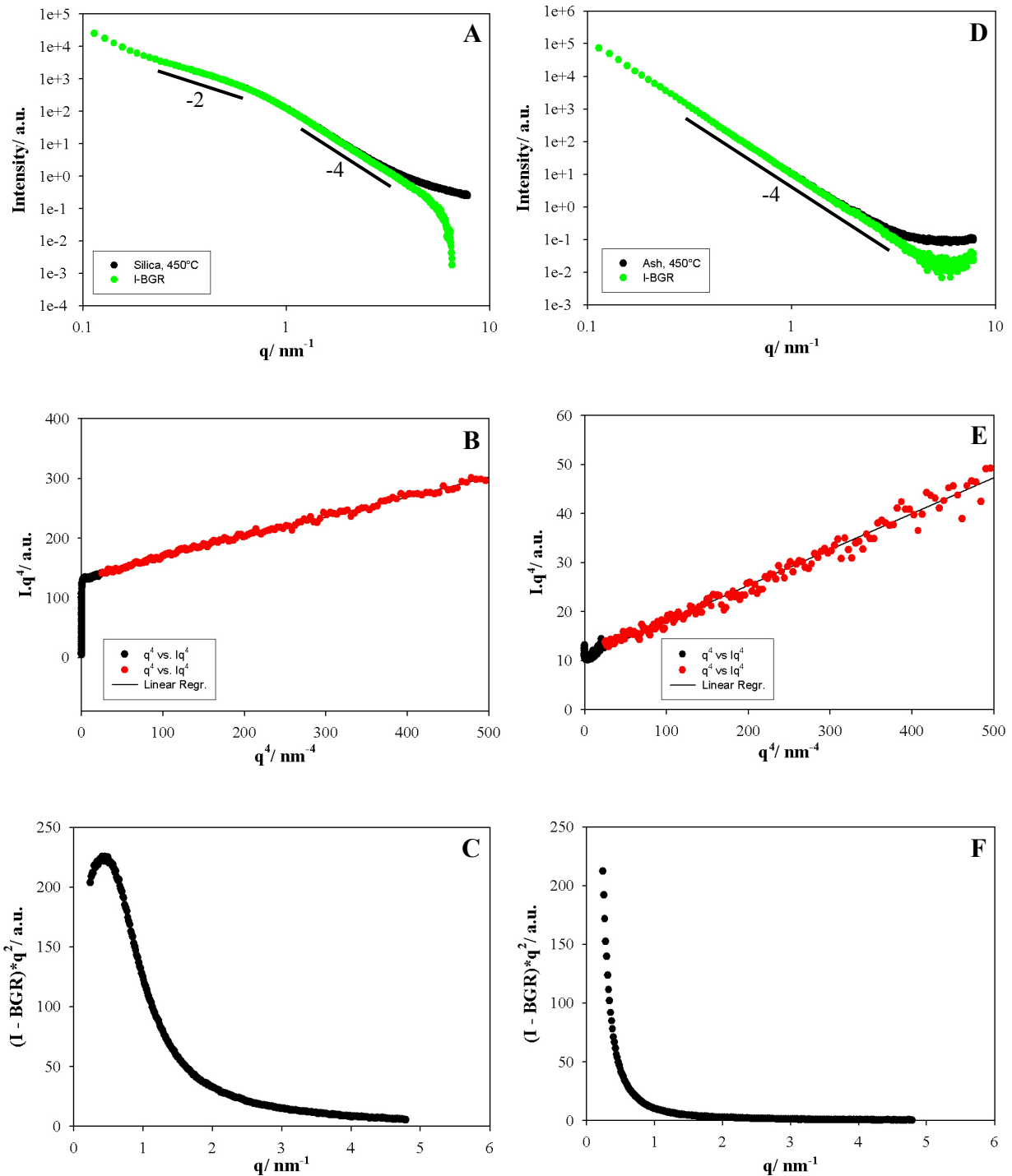


Figure C.3 Scattering profile, Porod plot, and Kratky plot. (A-C) HCl-treated *E.hyemale* calcined at 450°C. (D-E) Ash obtained after calcination of native *E.hyemale* at 450°C.

C.1.2 Normalisation of Porod constant and integrated SAXS intensity

Porod constants and integrated SAXS intensities of different silica ash and ash samples have to be normalised before being compared with other corresponding values obtained from other samples. Intensity normalisation was taken with respect to a factor K as defined below which contains some parameters that are not always constant during different measurement courses due to the X-ray beam intensity variation, noises, and different sample characteristics.

$$K = I_0 \cdot d \cdot \tau \cdot t \quad (\text{Equation C.2})$$

Where

I_0 = primary intensity

d = sample thickness

τ = transmission

t = time

Thus $I_{corrected} = \frac{I_{measured}}{K}$. Since Porod constant (P) and integrated intensity (\tilde{I}) are proportional to intensity, they must be also corrected in a similar way.

Time (t) is the same for all measurements, I_0 is relatively stable during the measurements, and the powder volume illuminated by X-ray beam is constant for all samples. Since $\tau = \exp(-\mu d) \Leftrightarrow d = -\ln \tau / \mu$ (see Eq. A.3) with μ is linear absorption coefficient which is specific for each elements. If μ 's are considered to be constant, thus a correction factor of τ ($-\ln \tau$) has to be taken into account since the each sample has different transmission value. Thus, both Porod constant (P) and Integrated intensity (\tilde{I}) can be corrected as follows:

$$P_{corrected} = \frac{P}{\tau(-\ln \tau)} \quad (\text{Equation C.3})$$

$$\tilde{I}_{corrected} = \frac{\tilde{I}}{\tau(-\ln \tau)} \quad (\text{Equation C.4})$$

It is considered that there are no significant differences in linear absorption coefficients (μ) within different biogenic silica and ash samples treated at different calcination temperatures (300°-750°C). Furthermore, the difference between μ of

biogenic silica and ash sample is less than 5%, according to a rough estimate described below. Thus, μ is assumed to be constant for all samples.

Ash sample was assumed to be composed of 60% Si, 15% Ca, 15% K, 5% Na, and 5% Mg, whereas biogenic silica sample was assumed to be composed of 100% Si. For the used X-ray energy 8.05 keV, μ of those elements are defined as depicted in Table C.1.

Table C.1 Specific absorption coefficient ¹⁷¹ for several elements at X-ray energy 8.05 keV

c	Element	μ (1/cm)
0.6	Si	151.72
0.15	Ca	264.98
0.15	K	127.60
0.05	Na	29.27
0.05	Mg	70.86

$$\mu_{ash} = \sum \mu_i \cdot c_i = 151.72(0.6) + 264.98(0.15) + 127.6(0.15) + 29.27(0.05) + (0.05)70.86$$

$$\mu_{ash} = 154.93$$

$$\frac{\mu_{ash} - \mu_{biogenic\ silica}}{\mu_{ash}} = \frac{154.93 - 151.72}{154.93} \times 100\% = 2\%$$

References

1. E. Fluck. Gmelin Handbook of Inorganic Chemistry. System number 15 Part A1. 8th Ed. Springer. Berlin-Heidelberg. (1984).
2. S.T. Pantelides and W.A. Harrison. Physical Review B 13 (1976): 2667-2691.
3. A. Feltz. Amorphous Inorganic Materials and Glasses. VCH. Weinheim. (1993).
4. S. Weiner and L. Addadi. Journal of Materials Chemistry 7 (1997): 689-702.
5. S. Weiner and H.D. Wagner. Annual Review of Materials Science 28 (1998): 271-298.
6. H.A. Lowenstam. Science 211 (1981): 1126-1131.
7. R.K. Iler. The Chemistry of Silica: Solubility, Polymerization, Colloid and Surface Properties, and Biochemistry. John Wiley & Sons. USA. (1979).
8. E. Epstein. Proc. Natl. Acad. Sci. USA 91 (1994): 11-17.
9. E. Epstein. Annual Review of Plant Physiology and Plant Molecular Biology 50 (1999): 641-664.
10. C.C. Perry, T. Keeling-Tucker. J. Biol. Inorg. Chem. 5 (2000): 537-550.
11. J.A. Raven, A.M. Waite. New Phytologist 162 (2004): 45-61.
12. J. Aizenberg, J.C. Weaver, M.S. Thanawala, V.C. Sundar, D.E. Morse, and P. Fratzl Science 309 (2005): 275-278.
13. C.N. Page. Bot. J. Linn. Soc. 65 (1972): 359-397.
14. R.M. Bateman, P.R. Crane, W.A. DiMichele, P.R. Kenrick, N.P. Rowe, T. Speck, W.E. Stein. Annual Review of Ecology and Systematics 29 (1998): 263-292.
15. W.N. Stewart and G.W. Rothwell. Paleobotany and the evolution of plants. Second edition. Cambridge University Press. USA. (1993).
16. R. Hauke. A taxonomic monograph of the genus *Equisetum* subgenus *Hippochaete*. Nova Hedwigia. Heft 8. J.Cramer Verlag. Weinheim. (1963).
17. R.L. Hauke. American Fern Journal 68 (1978): 37-40.
18. T. Speck, O. Speck, A. Emanns, H.C. Spatz. Botanica Acta 111 (1998): 366-376.
19. T.E. Timell. Svensk Papperstidning 67 (1964): 356-363.
20. F. Smithson. Nature 178 (1956): 107.

21. A.L. Carnelli, J.P. Theurillat, M. Madella. Review of Paleobotany and Palynology 129 (2004): 39-65.
22. C.H. Chen, J. Lewin. Canadian Journal of Botany 47 (1969): 125-131.
23. F.M. Hoffman, C.J. Hillson. Botanical Gazette 140 (1979): 127-132.
24. P.B. Kaufman, J.D. LaCroix, P. Dayanandan, L.F. Allard, J.J. Rosen, W.C. Bigelow. Developmental Biology 31 (1973): 124-135.
25. C.C. Perry, M.A. Fraser. Philosophical Transactions: Biological Sciences 334 (1991): 149-157.
26. G. Holzhueter, K. Narayanan, T. Gerber. Analytical and Bioanalytical Chemistry 376 (2003): 512-517.
27. P.B. Kaufman, W.C. Bigelow, R. Schmid, N.S. Ghosheh. American Journal of Botany 58 (1971): 309-316.
28. David. R. Lide. CRC Handbook of Chemistry and Physics. 73rd Ed. CRC Press, Inc. USA. (1992-1993).
29. B. Elvers, S. Hawkins, W. Russey, G. Schulz. Refractory Ceramics to Silicon Carbide. Ullmann's Encyclopedia of Industrial Chemistry. Vol. A. 23. 5th completely revised edition. VCH. Weinheim. (1993).
30. C.N. Fenner. Amer. J. Sci. 36 (1913): 331-384.
31. S.J. Stevens, R.J. Hand, J.H. Sharp. J. Mat. Sci. 32 (1997): 2929-2935.
32. P.P. Budnikow. Technologie der Keramischen Erzeugnisse "Einschliesslich der Feuerfesten Baustoffe". VEB Verlag Technik Berlin. (1953).
33. S. Sadasivan, D.H. Rasmussen, F.P. Chen, R.K. Kannabiran. Colloids and Surfaces A: Physicochemical and Engineering Aspects 132 (1998): 45-52.
34. N. Nishiyama, S. Tanaka, Y. Egashira, Y. Oku, K. Ueyama. Chem. Mater. 15 (2003): 1006-1011.
35. A.G. Howard, N.H. Khdary. Materials Letters 61 (2007): 1951-1954.
36. F. Jun, W. XiuFeng, W. LieSong, C. Bing, W.Y. Ting, Z. WanLin. Chinese Science Bulletin 52 (2007): 461-466.
37. T. Uchino, A. Aboshi, S. Kohara, Y. Ohishi, M. Sakashita, K. Aoki. Physical Review B 69 (2004) 155409.
38. S. Chandrasekhar, K.G. Satyanarayana, P.N. Pramada, P. Raghavan. Journal of Materials Science 38 (2003): 3159-3168.

39. N. Horn, M. Marquet, J. Meek, G. Budahazi. US Patent 5,576,196. (1996).
40. F. Serafini-Cessi, G. Bellabarba, N. Malagolini, F. Dall'Olio. *J. Immunol. Methods* 120 (1989): 185-189.
41. W.T. Tsai, K.J. Hsien, J.M. Yang. *J. Colloid and Interface Sci.* 275 (2004): 428-433.
42. Z. Korunic, P.G. Fields, M.I.P. Kovacs, J.S. Noll, O.M. Lukow, C.J. Demianyk, K.J. Shibley. *Postharvest Biology and Technology* 9 (1996): 373-387.
43. L.A. Zemnukhova, A.G. Egorov, G.A. Fedorishcheva, N.N. Barinov, T.A. Sokol'nitskaya, and A.I. Botsul. *Inorganic Materials* 42 (2006): 24-29.
44. D.M. Ibrahim, M. Helmy. *Thermochimica Acta* 45 (1981): 79-85.
45. M. Patel, A. Karera, P. Prasanna. *J. Mat. Sci.* 22 (1987): 2457-2464.
46. A. Chakraverty, P. Mishra, H.D. Banerjee. *Journal of Materials Science* 23 (1988): 21-24.
47. C. Real, M.D. Alcalá, J. M. Criado. *Journal of the American Ceramic Society* 79 (1996): 2012-2016.
48. N. Yalçın and V. Sevinç. *Ceramics International* 27 (2001): 219-224
49. S. Chandrasekhar, P.N. Pramada, P. Raghavan, K.G. Satyanarayana. *Journal of Materials Science Letters* 21 (2002): 1245-1247.
50. M.F. de Souza, W.L.E. Magalhães, M.C. Persegil. *Materials Research* 5 (2002): 467-474.
51. T.-H. Liou. *Mat. Sci. Eng. A* 364 (2004): 313-323.
52. L.Y. Sun and K.C. Gong. *Industrial & Engineering Chemistry Research* 40 (2001): 5861-5877.
53. L.P. Hunt, J.P. Dismukes, J.A. Amick. *J. Electrochem. Soc.: Solid-state Science and Technology* 131 (1984): 1683-1686.
54. J. G. Lee and I. B. Cutler. *Amer. Ceram. Soc. Bull.* 54 (1975): 195-198.
55. R.V. Krishnarao, M.M. Godkhindl, P.G.I. Mukunda, and M. Chakraborty. *J. Am. Ceram. Soc.* 74 (1991): 2869-2875.
56. R.V. Krishnarao. *Journal of Materials Science Letters* 12 (1993): 1268-1271.
57. R.V. Krishnarao, M.M. Godkhindl, M. Chakraborty, P.G. Mukunda. *Journal of Materials Science* 29 (1994): 2741-2744.

58. R.V. Krishnarao, Y.R. Mahajan. *Journal of the European Ceramic Society* 15 (1995): 1229-1234.
59. T.-H. Liou, F.-W. Chang, J.-J. Lo. *Ind. Eng. Chem. Res.* 36 (1997): 568-573.
60. R.V. Krishnarao, Y.R. Mahajan, T.J. Kumar. *Journal of the European Ceramic Society* 18 (1998): 147-152.
61. K. Janghorban, H.R. Tazesh. *Ceramics International* 25 (1999): 7-12.
62. S.K. Singh, B.C. Mohanty, and S. Basu. *Bull. Mater. Sci.* 25 (2002): 561-563.
63. J.C.C. Freitas, J.S. Moreira, F.G. Emmerich, T.J. Bonagamba. *Journal of Non-Crystalline Solids* 341 (2004): 77-85.
64. I.A. Rahman and F. L. Riley. *J. Eur. Ceram. Soc.* 5 (1989): 11-22.
65. T.-H. Liou, F.-W. Chang. *Ind. Eng. Chem. Res.* 35 (1996): 3375-3383.
66. H. Hamdan, M.N.M. Muhid, S. Endud, E. Listiorini, Z. Ramli. *Journal of Non-Crystalline Solids* 211 (1997): 126-131.
67. P. Strauch, S. Lehmann, R. Nöske. *Progress in Coordination and Bioinorganic Chemistry*, ed. M. Melnik and A. Sirota. Slovak Technical University Press. Bratislava. (2003): 329-342.
68. R. Nöske, I. Horn. German Patent „Verfahren zur Herstellung von Siliciumcarbid aus nachwachsenden Rohstoffen“. DD 100 20 626. (2001).
69. V. Valtchev, M. Smahi, A.C. Faust, L. Vidal. *Angewandte Chemie-International Edition* 42 (2003): 2782-2785.
70. V.P. Valtchev, M. Smahi, A.C. Faust, L. Vidal. *Chem. Mater.* 16 (2004): 1350-1355.
71. C.C. Perry and T. Keeling-Tucker. *Chem. Commun.* (1998): 2587-2588.
72. F. Fauteux, W. Rémus-Borel, J.G. Menzies, R.R. Bélanger. *FEMS Microbiology Letters* 249 (2005): 1-6.
73. R.V. Krishnarao, J. Subrahmanyam, T.J. Kumar. *Journal of the European Ceramic Society* 21 (2001): 99-104.
74. C. Real, M. D. Alcalá, A. Muñoz-Páez, and J. M. Criado. *Nuclear Instruments and Methods in Physics Research Section B* 133 (1997): 68-72.
75. D.R. Bassett, E.A. Boucher, A.C. Zettlemoyer. *Journal of Materials Science* 7 (1972): 1379-1382.

76. E. Fluck. Gmelin Handbook of Inorganic Chemistry. System number 15 Part B3. 8th Ed. Springer. Berlin-Heidelberg. (1984).
77. E.H.P. Wecht. Feuerfest-Siliciumcarbid. Springer. Wien. (1977).
78. Y. Zhang, N.L. Wang, R. He, X. Chen, J. Zhu. Solid State Communications 118 (2001): 595-598.
79. C. Vix-Guterl and P. Ehrburger. Carbon 35 (1997): 1587-1592.
80. P. Greil, T. Lifka, A. Kaindl. Journal of the European Ceramic Society 18 (1998): 1961-1973.
81. L. Esposito, D. Sciti, A. Piancastelli, and A. Bellosi. Journal of the European Ceramic Society 24 (2004): 533-540.
82. Y.-J. Lin and C.-P. Tsang. Ceramics International 29 (2003): 69-75.
83. R. Nöske, E. Ludwig, H. Fichtner, F. Piper. Chem. Technik. 44.Jg. Heft 7/8. (1992).
84. H. Sieber, C. Hoffman, A. Kaindl, P. Greil. Advanced Engineering Materials 2 (2000): 105-109.
85. P. Greil. Journal of the European Ceramic Society 21 (2001): 105-118.
86. Z. Di, S. Binghe, F. Tongxiang. Science in China Ser. E Engineering and Materials Science 47 (2004): 470-478.
87. E. Vogli, H. Sieber, P. Greil. Journal of the European Ceramic Society 22 (2002): 2663-2668.
88. M. Singh, B.-M. Yee. Journal of the European Ceramic Society 24 (2004): 209-217.
89. H. Sieber. Materials Science and Engineering A 412 (2005): 43-47.
90. Q. Guanjun, M. Rong, C. Ning, Z. Chunguang, J. Zhihao. Journal of Materials Processing Technology 120 (2002): 107-110.
91. T. Nagase, I. Nagamoto, T. Shiono, T. Nishida. J. Soc. Mat. Sci. Japan 54 (2005): 580-584.
92. R.V. Krishnarao and Y.R. Mahajan. Ceramics International 22 (1996): 353-358.
93. C. Vix-Guterl and P. Ehrburger. Carbon 35 (1997): 1587-1592.
94. K.J. Niklas. Plant Biomechanics: An Engineering Approach to Plant Form and Function. The University of Chicago Press. USA. (1992).

95. E. Gailliez-Degremont, M. Bacquet, J. Laureyys, M. Morcellet. *Journal of Applied Polymer Science* 65 (1997): 871-882.
96. H.G.M. Edwards, D.W. Farwell, D. Webster. *Spectrochimica Acta, Part A: Molecular and Biomolecular Spectroscopy* 53A (1997): 2383-2392.
97. U.P. Agarwal and S.A. Ralph. *Applied Spectroscopy* 51 (1997): 1648-1655.
98. J.L. Bishop and E. Murad. *Journal of Raman Spectroscopy* 35 (2004): 480-486.
99. L.C. Prinsloo, W. du Plooy, C. van der Merwe. *Journal of Raman Spectroscopy* 35 (2004): 561-567.
100. C.F.B. Séné, M.C. McCann, R.H. Wilson, and R. Crinter. *Plant Physiol.* 106 (1994): 623-1631.
101. A.J. Macnish, D.E. Irving, D.C. Joyce, V. Vithanage, A.H. Wearing, R.I. Webb, and R.L. Frost. *Australian Journal of Botany* 51 (2003): 565-572.
102. C. Paluszkiwicz, M. Gałka, W. Kwiatek, A. Parczewski, S. Walas. *Biospectroscopy* 3 (1997): 403-407.
103. R. Jetter, S. Schaffer, M. Riederer. *Plant, Cell and Environment* 23 (2000): 619-628.
104. S.K. Sharma, P.G. Lucey, M. Ghosh, H.W. Hubble, K.A. Horton. *Spectrochimica Acta Part A* 59 (2003): 2391-2407.
105. H. Moenke. *Mineralspektren. Die Ultrarotabsorption der häufigsten und wirtschaftlich wichtigsten Halogenid-, Oxyd-, Hydroxyd-, Carbonat-, Nitrat-, Borat-, Sulfat-, Chromat-, Wolfram-, Molybdat-, Phosphat-, Arsenat-, Vanadat- und Silikatmineralien im Spektralbereich 400-4000 cm⁻¹. Akademie Verlag Berlin.* (1962).
106. G. Socrates. *Infrared and Raman Characteristic Group Frequencies, Tables and Charts.* 3rd Edition. John Wiley and Sons Ltd. England. (2001): 241-247.
107. H.H.W. Moenke. Chapter 16. Silica, the three-dimensional silicates, borosilicates and beryllium silicates. V.C. Farmer (Editor). *Monograph 4. The Infrared Spectra of Minerals.* Mineralogical Society. London. (1974): 365-382.
108. M. Hino and T. Sato. *Bulletin of the Chemical Society of Japan* 44 (1971): 33-37.
109. K.K. Pandey. *Journal of Applied Polymer Science* 71 (1999): 1969-1975.
110. C.-F. Liu, J.-L. Ren, F. Xu, J.-J. Liu, J.-X. Sun, R.-C. Sun. *J. Agric. Food. Chem.* 54 (2006): 5742-5748.

111. C.J. Garvey, I.H. Parker, G.P. Simon. *Macromol. Chem. Phys.* 206 (2005): 1568-1575.
112. F.C. Lanning, B.W. Ponnaiya, C.F. Crumpton. *Plant physiology* 33 (1958): 339-343.
113. O. Paris, C. Zollfrank, G.A. Zickler. *Carbon* 43 (2005): 53-66.
114. O. Glatter, O. Kratky. *Small-Angle X-ray Scattering*. Academic Press. London. (1982).
115. P. Fratzl, H.F. Jakob, S. Rinnerthaler, P. Roschger, K. Klaushofer. *Journal of Applied Crystallography* 30 (1997): 765-769.
116. K.S.W. Sing, D.H. Everett, R.A.W. Haul, L. Moscou, R.A. Pierotti, J. Rouquérol, T. Siemieniewska. *Pure & Appl. Chem.* 57 (1985): 603-619.
117. E.P. Barrett, L.G. Joyner, and P.P. Halenda. *Journal of the American Chemical Society* 73 (1951): 373-380.
118. Spectral Database for Organic Compounds, SDBS. National Institute of Advanced Industrial Science and Technology (AIST). http://riodb01.ibase.aist.go.jp/sdbs/cgi-bin/cre_index.cgi?lang=eng
119. V.R. Franceschi and P.A. Nakata. *Annu. Rev. Plant Biol.* 56 (2005): 41-71.
120. F. Hong, N.O. Nilvebrant, L.J. Jönsson. *Biosensors and Bioelectronics* 18 (2003): 1173-1181.
121. K.A. Handreck and L.H.P. Jones. *Plant and Soil* XXIX (1968): 449-459.
122. C.C. Perry, S. Mann, R.J.P. Williams. *Proc. R. Soc. Lond. B* 222 (1984): 427-438.
123. C.K. Morikawa and M. Saigusa, *Plant and Soil* 258 (2004): 1-8.
124. C.T.G. Knight and S.D. Kinrade. Chapter 4. A primer on the aqueous chemistry of silicon. L.E. Datnoff, G.H. Snyder, and G.H. Korndörfer (Editors). *Silicon in Agriculture*. Elsevier Science B.V. Netherlands. (2001): 57-69.
125. J.D. Birchall. *Chemical Society Reviews* 24 (1995): 351-357.
126. C.C. Perry. Chapter 8. Chemical Studies of Biogenic Silica. S. Mann, J. Webb, R.J.P. Williams (Editors). *Biom mineralization: Chemical and Biochemical Perspectives*. VCH. Weinheim. (1989): 223-256.
127. R.D. Hartley, L.H.P. Jones. *Journal of Experimental Botany* 23 (1972): 637-640.
128. K. Schwarz. *Proceedings of the National Academy of Sciences of the United States of America* 70 (1973): 1608-1612.

129. N. Gierlinger, L. Sapei, O. Paris. *Planta* (2007). *Accepted (with minor correction)*.
130. J.C.C. Freitas, F.G. Emmerich, and T.J. Bonagamba. *Chem. Mater.* 12 (2000): 711-718.
131. P.J. Holloway. Plant cuticles: physicochemical characteristics and biosynthesis. K.E. Percy, J.N. Cape, R. Jagels, C.J. Simpson (Editors). *Air pollutants and the leaf cuticle. Ecological Sciences, NATO ASI Series, Vol. G 36.* Springer. Berlin-Heidelberg. (1994): 1–13.
132. R.L. Hauke. *Rev. Biol. Trop.* 15 (1969): 269-281.
133. A. Woesz, J.C. Weaver, M. Kazanci, Y. Dauphin, J. Aizenberg, D.E. Morse, P. Fratzl. *Journal of Materials Research* 21 (2006): 268-278.
134. D. Klemm, B. Philipp, T. Heinze, U. Heinze, W. Wagenknecht. *Comprehensive Cellulose Chemistry. Vol. 1. Fundamentals and Analytical Methods.* Wiley-VCH. Weinheim. (1998).
135. N.S. Trofimova, N.M. Zabivalova, A.M. Bochek, and N.P. Novoselov. *Russian Journal of Applied Chemistry* 74 (2001): 1924-1927.
136. L.G. Smirnova, Y.B. Grunin, S.V. Krasil'nikova, M.A. Zaverkina, D.R. Bakieva, and E.V. Smirnov. *Colloid Journal* 65 (2003): 778-781.
137. Y.-H.P. Zhang, M.E. Himmel, J.R. Mielenz. *Biotechnology Advances* 24 (2006): 452-481.
138. D. Fengel and G. Wegener. *Wood: Chemistry, Ultrastructure, Reactions.* Remagen: Kessel Verlag. (2003).
139. R. Blachnik. *D'Ans Lax Taschenbuch für Chemiker und Physiker. Band III. Elemente, anorganische Verbindungen und Materialien, Minerale. Vierte, neubearbeitete und revidierte Auflage.* Springer. Berlin-Heidelberg. (1998).
140. Y.-J. Hao, G.-Q. Jin, X.-D. Han, X.-Y. Guo. *Materials Letters* 60 (2006): 1334-1337.
141. O. Paris, I. Zizak, H. Lichtenegger, P. Roschger, K. Klaushofer, P. Fratzl. *Cellular and Molecular Biology (Paris)* 46 (2000): 993-1004.
142. Peter Fratzl. *Fibre Diffraction Review* 10 (2002): 31-39.
143. B.D. Cullity and S.R. Stock. *Elements of X-ray Diffraction. Third Edition.* Prentice Hall. New Jersey, USA. (2001).

-
144. A.C. Kak and M. Slaney. Principles of Computerized Tomographic Imaging. IEEE Press. New York. (1988).
 145. E. Badel, J-M. Létang, G. Peix, D. Babot. Meas. Sci. Technol. 14 (2003): 410-420.
 146. R.E. Alvarez, A. Macovski. Phys. Med. Biol. 21 (1976): 733-744.
 147. Skyscan n.v., Vluchtenburgstraat 3 – 2630 Aartselaar, Belgium. Skyscan 1172 – Desktop X-ray Microtomograph. Instruction Manual. (2005).
 148. E. Van de Castele, D. Van Dyck, J. Sijbers, and E. Raman. Effect of beam hardening on resolution in X-ray Microtomography. In SPIE Medical Imaging. (2004).
 149. R.W. Cahn, P. Haasen, E.J. Kramer. Materials Science and Technology “Characterisation of Materials Part I”. Vol. 2A. VCH. Weinheim. (1992).
 150. L. Reimer, G. Pfefferkorn. Raster-Elektronenmikroskopie. 2nd Edition. Springer. Berlin-Heidelberg. (1977).
 151. L. Reimer. Scanning Electron Microscopy “Physics of Image Formation and Microanalysis”. Springer Series in Optical Sciences. Vol. 45. Springer. Berlin-Heidelberg. (1985).
 152. Environmental Scanning Electron Microscopy. An introduction to ESEM[®]. Philips Electron Optics. Eindhoven, The Netherlands. 2nd Printing. Robert Johnson Associates. (1996).
 153. Bernhard Schrader. Infrared and Raman Spectroscopy “Methods and Applications”. VCH. Weinheim. (1995).
 154. N. Gierlinger and M. Schwanninger. Spectroscopy (Amsterdam, Netherlands) 21 (2007): 69-89.
 155. Olaf Hollrichter. Combine & Conquer “Confocal Raman microscopy teams high-resolution capabilities with powerful material analysis”. Spie’s *oe* magazine. November (2003): 16-20.
 156. Ewen Smith and Geoffrey Dent. Modern Raman Spectroscopy – A Practical Approach. John Wiley & Sons Ltd. England. (2005).
 157. A. Carden and M.D. Morris. Journal of Biomedical Optics 5 (2000): 259-268.
 158. Confocal Raman Microscopy. CRM 200 Manual. WiTec Wissenschaftliche Instrumente und Technologie GmbH. (1998-2001).

-
159. H.P. Klug and L.E. Alexander. X-ray Diffraction Procedures for Polycrystalline and Amorphous Materials. 2nd Edition. John Wiley & Sons. USA. (1974).
 160. J. Als-Nielsen and Des McMorrow. Elements of Modern X-ray Physics. John Wiley & Sons. England. (2001).
 161. R. Zallen. The Physics of Amorphous Solid. John Wiley & Sons. USA. (1983).
 162. H. Ibach and H. Lüth. Solid-state Physics. An Introduction to Principles of Materials Science. 2nd Edition. Springer. Berlin-Heidelberg. (1995).
 163. P. Fratzl. Acta. Phys. Polon. 82 (1992): 121-136.
 164. A. Guinier and G. Fournet. John Wiley & Sons. USA. (1955).
 165. G. Porod. Kolloid-Zeitschrift 124 (1951): 83-114.
 166. P. Fratzl, H.S. Gupta, O. Paris, A. Valenta, P. Roschger, K. Klaushofer. Progr. Colloid Polym. Sci. 130 (2005): 33-39.
 167. S.J. Gregg and K.S.W. Sing. Adsorption, Surface Area and Porosity. Second Edition. Academic Press. London. (1982).
 168. D.H. Everett. IUPAC Manual of Symbols and Terminology for Physicochemical Quantities and Units, Appendix 2, Part 1. Pure. Appl. Chem. 31 (1972): 578-638.
 169. M. Kruk and M. Jaroniec. Chem. Mater. 13 (2001): 3169-3183.
 170. S. Brunauer, P.H. Emmett, E. Teller. J. Am. Chem. Soc. 60 (1938): 309-319.
 171. Periodic Table, XAFS Database. <http://www.csrri.iit.edu/periodic-table.html>

ACKNOWLEDGEMENTS

This thesis was conducted at the Max Planck Institute of Colloids and Interfaces, Department of Biomaterials in the Biotemplating group of Dr.habil. Oskar Paris in Potsdam, Germany from April 2004 to September 2007. The financial support from Max Planck Society is gratefully acknowledged.

I wish to express my sincere gratitude to my supervisor, Dr.habil. Oskar Paris for giving excellent guidance, support, and his valuable and precise comments on my work. I would like to thank my second supervisor Prof. Dr. Peter Strauch at Potsdam University for his guidance, many valuable discussions, and encouragement. I am indebted to Dr. Notburga Gierlinger for the help with the Raman and FTIR experiments and their interpretation and for many fruitful discussions. I would also like to thank Dr. Robert Nöske for the collaboration on the whole project by providing the *E.hyemale* samples, doing numerous chemical/thermal treatments and for many useful discussions. I wish to thank Prof. Dr. Peter Fratzl for the opportunity he has given to me to do a PhD work in this internationally acclaimed leading research institute.

Additionally, I would like to express my gratitude to Ingrid Zenke for the help during SAXS/WAXS measurements and for the measurements using XRD at the last phase of my experiments. I thank also Dr. Jürgen Hartmann for his endurance doing numerous EDX measurements. Many thanks are conveyed to Christine Pilz who helped me a lot during the microtomography investigations. I wish to thank Annemarie Martins for the help during sample preparations and also Regina Rothe for the nitrogen sorption measurements. Special thanks to Prof. Bach from *Institut für Neuwertwirtschaft* (IfN) Zeitz for the XRF measurement.

I would like to thank Dr. Stefan Siegel and Dr. Chenghao Li for many useful discussions on hard physics and for their gentle and friendly personalities and for creating supportive work environment. I am indebted to Dr. Gerald Zickler, Dr. Wolfgang Wagermeier, Dr. Aurelien Gourrier, Dr. Barbara Aichmayer, Karin Jungnikl, Dr. Murat Kazanci, Dr. Atul Deshpande, Robin Seidel for many helpful discussions. I wish to thank Dr. Ingo Burgert, Dr. Willie Abasolo, Dr. Rivka Elbaum, Dr. Kazuchika Yamauchi and the rest of the plant group for many valuable discussions and inputs

related to silica in plant. I wish to thank Dr. Willie Abasolo also for his willingness to check and correct some grammatical errors in this thesis. Special thanks for Dr. Rivka Elbaum and family for their hospitality and never ending supports and for the delicious Jewish gastronomic specialties.

I thank Luna Goswami as my “permanent” neighbour since we came at the same time and stayed in the same office and thanks for sharing a lot of things concerning life, research and future. I also want to thank “der Junge” Maxim Erko for doing several SAXS/WAXS measurements for my ‘suddenly’ new project and for creating a live atmosphere in our office though just within a couple of months, “spaciba”. I would like to thank all other colleagues in this institute for the supports and creating such a nice atmosphere in this department.

I wish to express my gratitude to Löhmannsröben family for their hospitality, kindness, and their sincere helps and supports. Special thank to the ‘thai guy’ Laem for the valuable discussion on chemistry stuffs and for the nice dinner in Berlin with super hot “level ten” chilli. I thank my friends (Gregoria, Netty, ‘beloved’ ‘little’ Kim, Sally, Novita, William, Linda, Lusi, ...) and others who I cannot mention one by one for cheering me up and for their encouragements. I would like to express my gratitude to my family (father, sisters and brothers) for their unflinching love and for lifting my spirits up during the bad times. Finally, I thank the mighty God for His faithfulness, abundant love and grace empowering me through every hard time and for enabling me to complete this thesis work.

Curriculum vitae

Personal Information

Name : Lanny Sapei
Date of birth/ Place : 25th January 1978 in Bandung, Indonesia

Education

Since 04/2004 PhD student at Max Planck Institute of Colloids and Interfaces,
Biomaterials Department and Potsdam University, Germany
10/2001 - 2003 MSc. in “Biobased Materials”
Fachhochschule Reutlingen, Germany
1996 – 2000 BSc. in Chemical Engineering, subprogram Bioprocess
Institut Teknologi Bandung (ITB), Bandung
1993 – 1996 Senior High School at SMAK 1 BPK Bandung
1990 – 1993 Junior High School at SMPK 5 BPK, Bandung

Research

2004 - 2007 “Characterisation of silica in *Equisetum hyemale* and its transformation into biomorphous ceramics”.
PhD thesis at MPI (Max Planck Institute) of Colloids and Interfaces, Potsdam, Germany.
2003 “Effect of Scaffold Structure on Chondrocyte Phenotype”.
MSc. thesis at NMI (Natural and Medical Science Institute), Reutlingen, Germany.
1999 – 2000 “Ultrafiltration for reducing water from Crude Palm Oil (CPO) using hollow-fiber membranes”.
BSc. Thesis at ITB (Institut Teknologi Bandung), Bandung
Plant Design: “Glutamic acid production from fermentation of molasses using *Brevibacterium flavum*”